Residual Stresses and Oxidation of Silicon Carbide Fiber Reinforced Silicon Carbide Composites

by

Bradley L. Wing

A dissertation submitted in partial fulfillment
of the requirements for the degree of
Doctor of Philosophy
Material Science and Engineering
in the University of Michigan
2016

Doctoral Committee:

Professor John Halloran, Chair
Assistant Professor Samantha Daly
Dr. Kathleen Sevener
Professor Emeritus Anthony Waas

Table of Contents

List of Tables

List of Figures

Abstract

The focus of this study was to determine the effects of environmental exposure on mechanical properties of a continuous fiber, MI-RBSiC/SiC ceramic matrix composite (CMC). We have determined that crystallization expansion of silicon causes large residual stresses to accumulate at multiple length scales within the composite. Large residual microstresses, stresses exhibited between individual grains in the matrix, were measured in the silicon and SiC grains of the composite matrix using Raman spectroscopy. The microstresses were predicted using a modified thermo-elastic model in which the thermo-elastic strain was substituted for the crystallization expansion strain. The ply-level residual stresses, stresses formed between the laminate layers of the composite, were measured using Vickers indentations. A separate thermo-elastic model for determining residual stress as a result of coefficient of thermal expansion mismatch was modified to determine the residual stress accompanying the crystallization expansion of silicon in the matrix. To determine how the stress state changes as a result of processing and use, the residual microstress states were measured after annealing. A concurrent study of the oxidation of the debond layer concluded that thick fiber coatings allowed for oxygen to penetrate deeply into a fully dense composite without the presence of cracking or mechanical loading of any kind.

Chapter 1 Introduction

1.1 Objective

The goal of this research is to determine how the environment interacts with the composite manufactured by GE, called HiPerComp™. In order to achieve this goal, we first had to identify key factors of interest, determine the as-manufactured properties of these factors, and measure the changes that occurred during environmental testing.

The majority of this dissertation will focus on the residual stress state in the composite material, which is known to affect the first matrix cracking stress, which is a vital mechanical property in ceramic matrix composites. Much time was spent determining the source and magnitude of the residual stress in the as-manufactured material, after which, we were able to measure the affects of environment on the residual stress.

Another important aspect of the composite is the coating on the fiber. This coating provides a means of crack deflection, which preserves the strength of the fiber during matrix cracking. We examined the oxidation behavior of the fiber coatings under various temperatures and times.

1.2 Background

Ceramic matrix composites (CMCs) show incredible potential for lowering overall weight and increasing strength in cases of high temperatures applications[1–6]. In the instance of aerospace applications, CMCs offer weight reduction[4,7], increased

operating temperatures[8–12], and increased efficiency over super-alloy counterparts[13–15]. Specifically, SiC/SiC CMCs have received considerable efforts in recent years due to its preferable mechanical and chemical properties[16,17]. CMCs are preferential to the monolithic counterparts due to the fiber reinforcements[18,19]. Crack propagation through the matrix of a CMC allows for a reduction in the stress on the composite[20,21], while the fibers maintain the load on the composite. The traction between the fiber and the debond layer offers a toughening mechanism for the composite[22–24], and allows for seemingly ductile response from the ceramic composite[25–27].

SiC/SiC composites can be manufactured in a variety of methods using various fiber configurations[28]. The research presented here focuses on a continuous fiber laminate layup, meaning that the fibers in a single laminate all have the same orientation and have no intentional crossing within the tow. This is a relatively simple architecture compared to something like a 2-D woven laminate where the fibers are intentionally crossed in a systematic method to increase the strength in a complex stress condition.

The fibers are first coated with boron nitride (BN) while in bundles called tows. The tows are laid together, all in the same direction, and sent through a polymer-based slurry that acts to hold the tows together. At this stage, the strcuture is called a prepreg tape, and this is the basis of a single laminate in the final composite. The prepreg tape is pyrolized to create a carbon rich, porous structure in preparations for melt-infiltration.

The matrix portion of the composite if formed via the melt-infiltration process. The pyrolized laminates are laid up in the proper architecture, and liquid silicon is allowed to infiltrate the laminates, where it reacts with the carbon and forms silicon carbide[29,30]. The laminate composite produced has a [0/90]2s architecture, with a layer of

matrix only material between each fiber containing layer (Figure 1.1). In this process, not all of the silicon reacts. Typically, 10-50 vol% of the resulting reaction bonded silicon carbide (RBSiC) consists of unreacted free silicon [2].

Although the residual silicon lowers the temperature capabilities of the composite, it allows for a fully dense, near net shape composite within a single processing step[31–34]. This is advantageous when compared to chemical vapor deposition, which results in a very porous composite[32,35], or PIP, which takes numerous steps to create a fully dense composite[36,37].

1.3 Dissertation Overview

1.3.1 Crystallization Expansion of Silicon

The focus of the this effort was a class of CMCs consisting of a melt-infiltrated (MI) SiC/SiC CMC, commonly known as HiPerComp™, designed by GE Aviation[38]. The unreacted free silicon that provides the focus of this study. When the free liquid silicon is allowed to cool, it solidifies and expands. Nominally, we expect an 11 vol% expansion of the silicon phase when transforming from liquid to solid; however, the silicon phase is surrounded by the much stiffer SiC phase of the matrix. The result is that the silicon in the matrix experiences a compressive stress, while the SiC of the matrix will have a tensile stress. This phenomenon has yet to be studied.

In a study by Wilhelm et al.[17], it was mentioned that residual stress plays a role in the mechanical properties of RBSiC, however the magnitude of the residual stress is not determined. Hillig notes that the expansion of the silicon can cause a residual stress state in RBSiC, but does not measure or compute the stress that would result[39]. We examine

the magnitude of the stress from the crystallization expansion of silicon in two monolithic materials in Chapter 2, and in the matrix of the CMC material in Chapter 3.

This event is further complicated in the composite, since the matrix is only part of the composite. Although the silicon is constrained by the surrounding SiC, there is still some expansion of the two-phase mixture. This will have an effect on the other components of the composite and ultimately will contribute to the mechanical properties of the composite. In the thesis of Dan Dunn[40], he noticed that cracks formed in the matrix of the composite during bend testing, closed up when the load was removed. Dunn attributed the crack closing within the matrix to a compressive stress in the matrix portion of the composite. Similarly, Morscher et al. witnessed a composite compressive stress during tensile testing of the composite[41]. In the Morscher study, hysteresis loops were performed above the proportional limit of the composite. Upon unloading, the loops showed a reduction in the amount of strain induced post-proportional limit. This implies a compressive stress in the composite that causes a reduction in openness of the cracks produced during tensile testing.

In Chapters 2 and 3, we showed that the unreacted free silicon expands. In Chapter 5, we determine the total amount of expansion of the two-phase, siliconized-SiC based on the crystallization expansion of the silicon. As can be seen in Figure 1.1, between each of the fiber containing layers is a layer of matrix only material. The expansion of the silicon phase during processing will cause all of the siliconized-SiC material to expand evenly. However, in the layers of the composite that have fibers, the fibers will act to dilute the expansion of that layer. The result is some type of stress state in the matrix layers and in the fiber layers. We have measured the ply-level stress that

develops in the matrix only layers of the composite using an indentation method. We then modified a thermo-elastic residual stress model to predict the ply-level stress from the crystallization expansion of silicon.

1.3.2 Relaxation of Residual Stress

It is not only important to understand the mechanical properties as-manufactured at room temperature, but also how those properties will be affected during the life of the material. For this reason, Chapter 4 and Chapter 6 focus on how the composite material responds when exposed to a harsh environment.

In Chapter 4, we have examined how the stress in the unreacted free silicon phase and the SiC phase relax as a function of time and temperature for the monolithic and composite materials. This was done for one of the monolithic materials as well as the CMC for direct comparison. The monolithic material was chosen for its use in an earlier creep study by Weiderhorn[42]. The differences and similarities between the monolithic material and the composite material are reported.

1.3.3 Oxidation of Boron Nitride Coatings

Finally, in Chapter 6, the environmental work continues by examining the oxidation behavior of the boron nitride (BN) coatings. Oxidation is considered one of the key limiting factors of CMCs[43]. In this chapter, it is observed that the BN coatings act as a pipeline for oxygen ingress into the fully dense composite material. As was expected, the depth of oxygen penetration is dependent on the time and temperature of exposure. However, it was also observed that the thickness of the BN coating was a large contributor to the depth to which oxygen is able to penetrate.

References

1. Luthra K, Singh R, Brun MK. Toughened Silcomp Composites - Process and Preliminary Properties. *Am Ceram Soc Bull*. 1993;72:79.

2. Zhou H, Singh RN. Processing and Microstructural Characterization of Melt-Infilitrated Si/SiC Composites. *J Mater Synth Process*. 1997;5:125-134.

3. Zhou H, Singh RN. Kinetics Model for the Growth of Silicon Carbide by the Reaction of Liquid Silicon with Carbon. *J Am Ceram Soc*. 1995;9(78):2456-2462.

4. Jacobson NS, Fox DS, Opila EJ. High Temperature Oxidation of Ceramic Matrix Composites. *Pure Appl Chem*. 1998;70:493-500.

5. Singh M, Behrendt DR. Microstructure and Mechanical Properties of Reaction-Formed Silicon Carbide (RFSC) Ceramics. *Mater Sci Eng*. 1994:183-187.

6. Gouadec G, Colomban P, Bansal NP. Raman Study of Hi-Nicalon-Fiber-Reinforced Celsian Composites: I, Distribution and Nanostructure of Different Phases. *J Am Ceram Soc*. 2001;84:1129-1135.

7. Lin HT, Waters S, Breder K. High-temperature creep response of a commercial grade siliconized silicon carbide. doi:10.1023/A:1004616617093.

8. Naslain R, Guette A, Rebillat F, et al. Oxidation mechanisms and kinetics of SiC-matrix composites and their constituents. doi:10.1023/B:JMSC.0000048745.18938.d5.

9. WIEDERHORN S, FIELDS B, HOCKEY B. FRACTURE OF SILICON-NITRIDE AND SILICON-CARBIDE AT ELEVATED-TEMPERATURES. doi:10.1016/0921-5093(94)90958-X.

10. Amer MS, Durgam L, El-Ashry MM. Raman mapping of local phases and local stress fields in silicon–silicon carbide composites. *Mater Chem Phys*. 2006;98(2–3):410-

414. http://www.sciencedirect.com/science/article/pii/S0254058405006838. Accessed August 1, 2006.

11. LUTHRA K. THERMOCHEMICAL ANALYSIS OF THE STABILITY OF CONTINUOUS SIC FIBERS.

12. Morscher GN, Cawley JD. Intermediate Temperature Strength Degradation in SiC/SiC Composites. *J Eur Ceram Soc*. 2002;22:2777-2787.

13. Smith CE, Morscher GN, Xia Z. Electrical Resistance as a Nondestructive Evaluation Technique for SiC/SiC Ceramic Matrix Composites Under Creep-Rupture Loading. *Int J Appl Ceram Technol*. 2011;8:298-307.

14. Grondahl CM, Tsuchiya T. Performance Benefit Assessment of Veramic Components in an MS9001FA Gas Turbine. *J Eng Gas Turbines Power-transactions Asme*. 2001;123:513-519.

15. Larochelle KJ, Morscher GN. Tensile Stress Rupture Behavior of a Woven Ceramic Matrix Composite in Humid Environments at Intermediate Temperature - Part 1. *Appl Compos Mater*. 2006;13:147-172.

16. Wilhelm M, Kubel F, Wruss W. XRD Investigation of Si-SiC Composites with Fine SiC Microstructure. *Powder Diffr*. 2001;16:42-45.

17. Wilhelm M, Kornfeld M, Wruss W. Development of SiC-Si Composites with Fine-grained SiC Microstructure. *J Eur Ceram Soc*. 1999;19:2155-2163.

18. DICARLO J. CREEP OF CHEMICALLY VAPOR-DEPOSITED SIC FIBERS. doi:10.1007/BF01144723.

19. DiGregorio JF, Furtak TE. Analysis of Residual Stress in 6H-SiC Paricles within Al2O3/SiC Composites through Raman Spectroscopy. *J Am Ceram Soc*. 1992;75:1854-

1857.

20. Morscher GN, Pujar VV. Design Guidelines for In-Plain Mechaincal Properties of SiC Fiber-Reinforced Melt-Infiltrated SiC Composites. *Int J Appl Ceram Technol*. 2009;6:151-163.

21. Morscher GN. Stress-dependent matrix cracking in 2D woven SiC-fiber reinforced melt-infiltrated SiC matrix composites. doi:10.1016/j.compscitech.2003.10.022.

22. Nimmer R, Corman G, Gilmor R. *Laminate Orientation and Bias Effects on Preprep HiPerComp CMC Mechanical Properties*. Niskyuna, NY: GE Global Research; 2009:1-20.

23. THOULESS M, EVANS A. EFFECTS OF PULL-OUT ON THE MECHANICAL-PROPERTIES OF CERAMIC-MATRIX COMPOSITES. doi:10.1016/0001-6160(88)90083-1.

24. THOULESS M, SBAIZERO O, SIGL L, EVANS A. EFFECT OF INTERFACE MECHANICAL-PROPERTIES ON PULLOUT IN A SIC-FIBER-REINFORCED LITHIUM ALUMINUM SILICATE GLASS-CERAMIC. doi:10.1111/j.1151-2916.1989.tb06171.x.

25. Trice RW, Halloran JW. Influence of Microstructure and Temperature on the INterfacial Fracture Energy of Silicon Nitride/Boron Nitride Fibrous Monolithis Ceramics. *J Am Ceram Soc*. 1999;82:2502-2508.

26. Baskaran S, Halloran JW. Fibrous Monolithic Ceramics: III, Mechanical Properties and Oxidation Behavior of the Silicon Carbide/Boron Nitride System. *J Am Ceram Soc*. 1994;5(77):1249-1255.

27. Dever JA, Nathal MV, DiCarlo JA. Research on High-Temperature Aerospace Materials at NASA Glenn Research Center. doi:10.1061/(ASCE)AS.1943-5525.0000321.

28. Naslain RR. Processing of Ceramic Matrix Composites. *Key Eng Mater*. 1999;164-165:3-10.

29. Hayun S, Frage N, Dariel MP. The morphology of ceramic phases in BxC-SiC-Si infiltrated composites. doi:10.1016/j.jssc.2006.01.031.

30. Martinez Fernandez J, Munoz A, de Arellano Lopez AR, Valera Feria FM, Dominguez-Rodriguez A, Singh M. Microstructure-Mechanical Properties Correlation in Siliconized Silicon Carbide Ceramics. *Acta Mater*. 2003;51:3259-3275.

31. Luo ZH, Jiang DL, Zhang JX, Lin QL, Chen ZM, Huang ZR. Influence of Phenolic Resin Impregnation on the Properties of Reaction-Bonded Silicon Carbide. doi:10.1111/j.1744-7402.2012.02758.x.

32. Bhatt RT, Gyekenyesi JZ, Hurst JB. Silicon Effects on Properties of Melt Infiltrated SiC/SiC Composites. *NASA/TM*. 2000;210034:1-9.

33. Singh M, Behrendt DR. Studies on the Reactive Melt Infilitration of Silicon and Silicon-Molybdenum Alloys in Porous Carbon. *Annu Meet Am Ceram Soc*. 1992;(94).

34. Weber S, Sommer F, Kern F, Gadow R, Voggenreiter H, Koch D. Thermoplastic Forming as an Alternative Shaping Process for Near-Net-Shape Production of C-SiSiC Ceramics via Liquid Silicon Infiltration (LSI) Process. doi:10.4416/JCST2014-00011.

35. Probst KJ, Besman TM, Stinton DP, Lowden RA, Anderson TJ, Starr TL. Recent Adances in Forced-Flow, Thermal-Gradient CVI for Refractory Composites. *Surf Coatings Technol*. 1999;(120-121):250-258.

36. Yajima S, Hayashi J, Omori M, Okamura K. Development of a Silicon Carbide

Fibre with High Tensile Strength. *Nature*. 1976;261:683-685.

37. Ishikawa T, Kojtoku Y, Kumagawa K, Yamamura T, Nagasawa T. High-strength Alkali-resistant Sintered SiC Fibre Stable to 2,200 C. *Lett to Nat*. 1998;391:773-775.

38. Corman GS, Luthra KL. Silicon Melt Infiltrated Ceramic Composites (HiPerComp). In: *Handbook of Ceramic Composties*. New York: Springer; 2005.

39. Hillig WB. Melt Infiltration Process for Making Ceramic Matrix Composites. In: Mazdiyasni KS, ed. *Fiber Reinforced Ceramic Composites*. Park Ridge, NJ: Noyes Publications; 1990:261-277.

40. Dunn D. The Effect of Fiber Volume Fraction in HiPerComp SiC-SiC. 2010.

41. Morscher GN, Ojard G, Miller R, et al. Tensile creep and fatigue of Sylramic-iBN melt-infiltrated SiC matrix composites: Retained properties, damage development, and failure mechanisms. *Compos Sci Technol*. 2008;68(15-16):3305-3313. doi:10.1016/j.compscitech.2008.08.028.

42. Wiederhorn SM, Hockey BJ, French JD. Mechanisms of Deformation of Silicon Nitride and Silicon Carbide at High Temperatures. *J Eur Ceram Soc*. 1999;19:2273-2284.

43. Sheldon BW, Sun EY, Nutt SR, Brennan JJ. Oxidation of BN-Coated SiC Fibers in Ceramic Matrix Composites. *J Am Ceram Soc*. 1996;79:539-543.

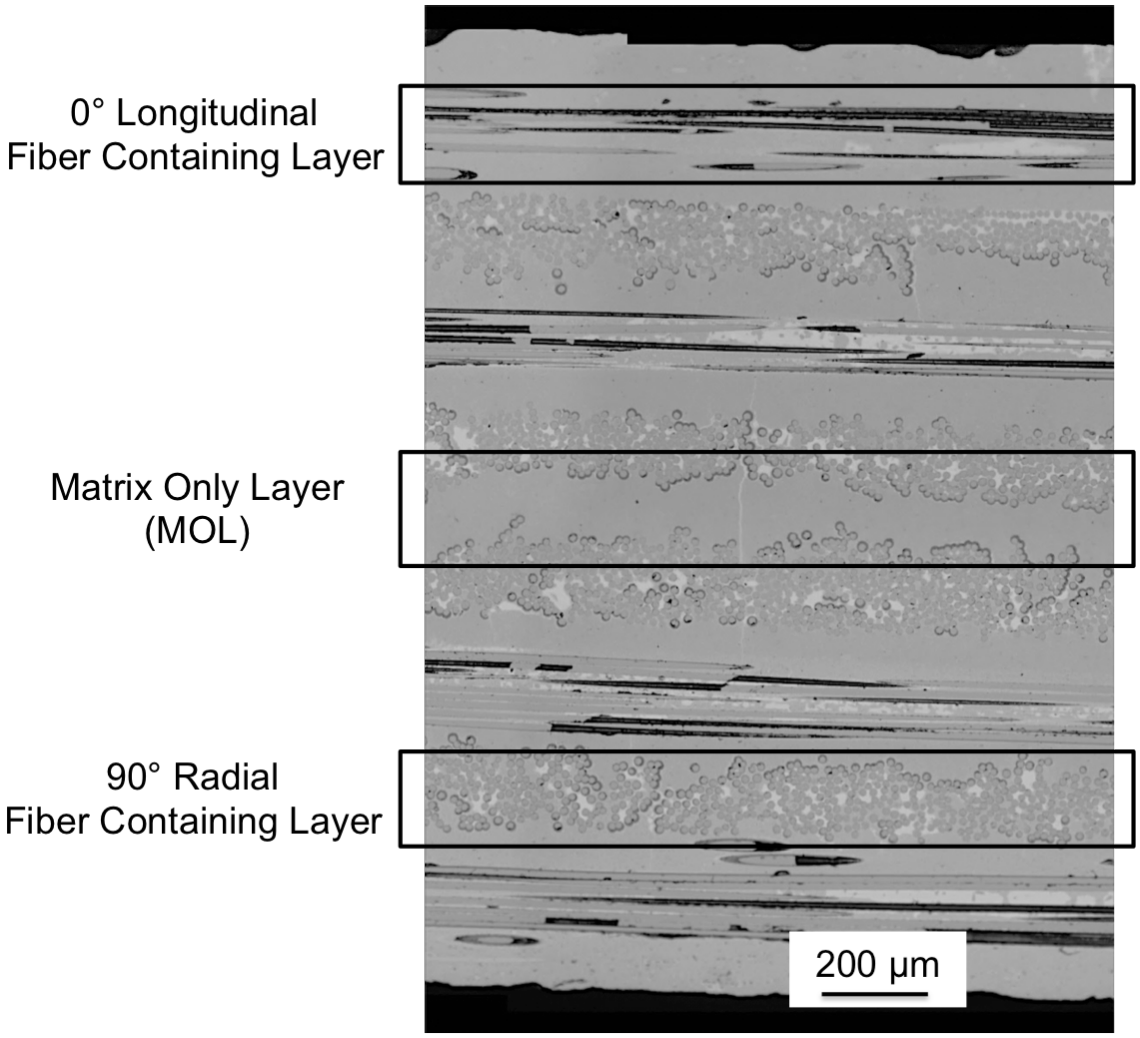

Figure 1.1. Representative of the [0/90]2s architecture of HiPerComp™.

Chapter 2 Microstress from Crystallization Expansion of Silicon in Reaction Bonded Silicon Carbide[1]

2.1 Introduction

Silicon carbide is a very useful material for a number of applications due to its high temperature capabilities, high thermal conductivity, and low density[1–3]. There are many ways of manufacturing SiC including powder sintering, chemical vapor deposition (CVD), pyrolysis of silicon containing polymer preforms, as well as other techniques[4]. Reaction bonding is a prominent technique, where a preform is converted to SiC by the reaction of liquid silicon with a source of carbon, and is often conducted by melt-infiltration (MI) of liquid silicon into a carbon preform[5,6]. By melt-infiltration, fully dense RBSiC can be made to net shape at relatively low temperatures, with relatively fast manufacturing[7].

In the MI process, silicon carbide is formed by the reaction of liquid silicon alloy with a carbon source to form a rigid SiC network. A disadvantage of MI is that a fraction of the silicon is not reacted. Typically, a significant fraction of the silicon is left unreacted, so that the RBSiC is a two-phase mixture of SiC and free silicon [5]. While RBSiC is a well-known material and process, the existence of large residual microstress on the scale of the grain size is a little-recognized attribute. In this chapter, we present

[1] This chapter has been submitted for review to the Journal of the American Ceramic Society on October 6, 2015.

measurements of the compressive microstress in the free silicon phase and tensile microstresses in the SiC phase. We propose that these microstresses arise from the crystallization of the free silicon liquid during cooling.

Liquid silicon is a random dense packed liquid, but crystalline silicon is a tetrahedral solid with a significantly lower density. The density difference between the liquid and crystal causes the silicon volume fraction to expand by about 11% upon solidification, which creates a crystallization expansion strain (CES). The phenomenon of crystallization expansion of the free silicon has been noted by Hillig[8], but he makes no reference to its role in the resulting microstresses. The SiC network is rigid, and so silicon crystallization must either expel some of the liquid silicon, or SiC network must constrain the silicon phase. Preventing the silicon expansion causes a residual microstress state. The constrained silicon phase must experience a compressive residual microstress while the constraining SiC phase must experience a tensile residual microstress. This chapter addresses the measurement of these microstresses and determines the cause of the microstresses.

2.2 Materials and Experimental Methods

2.2.1 Materials and Microstructural Characterization

We examine two commercial grades of reaction-bonded silicon carbide (RBSiC) with two markedly different volumes fractions of free silicon. The lower-silicon RBSiC material is SC-2 is received from Coors Tek in 2014, and the higher-silicon RBSiC is KXO1 and was manufactured by Carborundum around 1986 and was provided by Sheldon Wiederhorn from samples of a material used in a previous study of creep[9]. The volume fraction of the free silicon phase was determined by examining more than 80

fields of view of polished surfaces, imaged optically at 200x using a Nikon Eclipse ME600L microscope. The silicon phase was isolated with a threshold function and its area fraction determined using Matlab.

The free silicon fraction was independently determined with quantitative X-ray diffraction (XRD) using the internal standards method. An internal standard was created using known volumes of silicon powder and the RBSiC material, which has an unknown amount of free silicon. The integrated intensity ratios depend on the total amount of silicon. This is the known amount of silicon powder as well as the unknown amount of native silicon in the RBSiC material. Standards consisted of 0, 10, 20, 30, and 40 vol% silicon with the remaining volume made up of RBSiC. The integrated intensity of the (111), (220), and (311) peaks of silicon compared with the (101), (102), (103), (104), and (110) α-SiC peaks. The diffraction patterns were collected with a Rigaku Miniflex over the range from 10-65° using a scan rate of 1°/min with a step size of 0.02°.

2.2.2 Raman Spectroscopy Method

We measured the residual microstress state in the silicon phase and SiC phase using Raman microspectroscopy, which is a common technique used to determine the residual microstress state in a material[10–12]. Raman spectroscopy is a measurement of inelastic light scattering arising from the polarizability of molecular vibrational modes. Molecular species have Raman emission bands with characteristic frequencies. As microstress is applied, then the characteristic shift position associated with the vibrational modes will shift. Shifts in Raman band positions indicate alterations to the vibrational mode structure, and can be used to measure the hydrostatic stress on the molecular species at very high spatial resolution.

The difference between the peak position of the unstressed state and the microstress state is measured as a wavenumber shift, $\Delta\omega$[13]. This shift can be used to calculate the current microstress state based on the equation

$$\Delta\omega = R\sigma \quad [1]$$

where R is the coefficient relating the Raman shift to the hydrostatic stress, and σ is the hydrostatic stress experienced by the corresponding phase.

Silicon has a well-defined, single Raman peak at 520 cm^{-1} and a Raman coefficient of 1.88 ± 0.05 cm^{-1}/GPa has been measured by Anastakakis et al[14]. SiC is a more complicated, having a triplet transverse optic (TO) peak and a broad longitudinal optic (LO) peak. DiGregorio and Furtak have analyzed the TO peak of polycrystalline SiC[15], and fit the full triplet of the TO as a single peak, with an unstressed state of 797 cm^{-1}. They determined a Raman coefficient for the TO peak in polycrystalline SiC to be 3.53 ± 0.21 cm^{-1}/GPa. This will serve as the Raman coefficient for both α and β-SiC[15,16]

A custom Raman microspectroscopy system was used in this work[17,18]. A fiber optic coupled 532 nm green laser (Innovative Photonics) was collimated and reflected off a dichroic filter (SEMROCK). The dichroic filter brought the laser onto the same axis as the Raman scattering collection path. The laser was directed into a Nikon Eclipse ME600L microscope using a custom-built turning mirror turret. The laser passed through the microscope optics in an epi-illumination geometry, and focused into a spot size of 20 microns at the sample surface providing energy for Raman scattering.

The Raman scattered photons from the sample are collected back through the microscope optics, passing through the dichroic as the Raman emission wavelength is

longer than the source laser light. The dichroic acts to first bring the laser light onto the same path as the collection beam, and also to filter out 532 nm laser light. A notch filter (SEMROCK) was placed behind the dichroic to provide additional laser rejection prior to a second collimating objective which fiber-coupled the collection beam. By removing residual laser excitation power, the notch filter eliminates interfering Raman scattering from SiO_2 in the fiber optics. The collection fiber optic then delivered the collected Raman signal into a HoloSpec VPT spectrograph (Kaiser Optical Systems, Inc.). In the spectrograph the Raman scattered light is dispersed by the grating such that different wavelengths of light are measured at different physical locations across the imaging detector (charged coupling device, CCD). A Newton EM CCD (ANDOR) was used to measure the Raman scattered light and transmit the recorded signal to a computer for analysis in Matlab (MathWorks).

2.3 Results: Microstress from Raman Measurements

2.3.1 Microstructure and Free Silicon

Figure 2.1 illustrates the microstructure as optical images of polished sections for each grade. The images show two interpenetrating networks consisting of silicon (light grey) and SiC (dark grey). In these images, we can see the extent of the unreacted free silicon. The characteristic size of the SIC phase, inferred from linear intercept measurements, varies from 1.9-4.8 microns in the low-Si material, with the free silicon phase having a characteristic size of 0.6-4.6 microns. The SiC phase is somewhat smaller in the high-Si material, 1.3-2.8 microns, with the free silicon region in the range 0.8-1.8 microns.

Image analysis determined the volume fraction of free silicon to be 20 ± 4 vol% for the low-Si material and 40 ± 6 vol% for high-Si material. These values represent the mean volume fraction average of 80 fields of view with the variation representing the range of repeated analyses.

For the XRD analysis, the method of internal standards was used. In Figure 2.2 we show the ratio of the integrated intensities for the three silicon peaks over the total integrated intensity (silicon and SiC), plotted against the added amount of silicon powder. The overall volume of silicon was determined using the form:

$$\frac{I_{Si}}{I_{Si}+I_{SiC}} = m\left[x + (1-x)V_{Si}^{RBSiC}\right] \qquad [2]$$

where I is the integrated intensity of the respective phase, x is the volume of pure silicon added to the powder, V_{Si}^{RBSiC} is the volume fraction of silicon phase in the RBSiC material, and m is a constant determined experimentally. The amount of silicon in the RBSiC material is constant. Using the relationship in Eq [2], we were able to determine the unknown amount of silicon in the RBSiC material. XRD determined that the silicon content in the high-Si RBSiC is 42 ± 1% and the constant m is 1.048. For the low-Si material, the free silicon volume fraction was determined to be 24 ± 1%. This is in very good agreement with values obtained by image analysis.

2.3.2 Microstress from Raman Measurements

Raman spectra were recorded at 20 different positions on each sample. Using a spot size of 20 microns, we were able to include more than 10 SiC grains and the surrounding free silicon. Four different samples of the high and low silicon materials were examined. Figure 2.3 shows typical spectra for 4 locations in a sample with high-Si content. The positions of the spots are illustrated in the microstructure at the top of Figure

2.3 The complete spectrum, including the Si peak near 520 cm^{-1} and the SiC peak near 797 cm^{-1}, are in the center of Figure 2.3. The lower left Figure 2.3 shows in detail the region of the silicon peak. Notice that the spectra from the four locations overlap. The unstressed silicon peak location is shown as a line at 520 cm^{-1}. The observed peaks are centered around 523 cm^{-1}, indicating a red-shift which we interpret as arising from a compressive microstress in the free silicon phase. The lower right portion of Figure 2.3 shows the 4 observed spectra for the TO SiC peak with the unstressed peak location shown at 797 cm^{-1}. These have different intensities, but all are centered around 787-789 cm^{-1}. The blue shift from the unstressed peak indicates the presence of tensile stresses in the SiC phase.

Figure 2.4 has similar information from 4 typical locations for the low-Si material, showing the locations of the probed region (top of Figure 2.4), the four spectra (center of Figure 2.4) and details of the Raman peaks from the silicon phase (bottom left of Figure 2.4) and Raman peaks from the SiC phase (bottom right of Figure 2.4).

Table 2.I lists the measured peak locations for the 4 example positions for both samples, and the residual microstress calculated using a piezoraman coefficient of 1.88 ± 0.05 cm^{-1}/GPa for the 520 Si peak and 3.53 ± 0.21 cm^{-1}/GPa for the TO peak in polycrystalline SiC. For these examples, the silicon phase is shown to have a compressive residual microstress of around 1.74-1.88 GPa, while the SiC phase has a tensile residual microstress of 2.13-2.37 GPa in high-Si material and 1.77-2.08 GPa of compression in silicon and 2.10-2.43 GPa of tension in SiC in the low-Si material. These values correspond to the spectra in Figure 2.3 and Figure 2.4.

Table 2.II presents all the data for both grades of RBSiC, for 20 locations in each of 4 specimens of each material. Each value is the result of 20 spectra taken at different points on the polished sample. The results of Eq. [1] from each spectrum are averaged together for the reported residual microstress measurement. The measured stresses are consistent from sample to sample. The location-to-location variation is taken into account within the error calculation. The error reported also includes the peak fitting error and the reported Raman coefficient error.

2.4 Discussion

The measured hydrostatic stress state found in both of the RBSiC materials is very large. These large microstresses exist in commercially available RBSiC as well as RBSiC produced in a lab more than 25 years prior to this study. For the compressive microstress measured in the silicon, the low-Si material (mean value of 1.92 ± .11 GPa) showed a slightly higher magnitude than that of the measured compressive microstress in the silicon phase of the high-Si material (mean value of 1.76 ± .15 GPa). Conversely, the low-Si material, has a lower residual tensile microstress in the SiC phase (mean value of 2.12 ± .22 GPa) than that of the SiC phase in the high-Si material (mean value of 2.28 ± .10 GPa).

These stresses are very large, and have not been reported in previous studies. Two potential sources for these large stresses were investigated: (1) as a result of a coefficient of thermal expansion mismatch (thermoelastic stresses) and (2) as a result of the crystallization expansion of silicon during processing. We will evaluate the magnitude of these two sources of stress and determine which contributes most to the measured microstresses or if there is equal contribution.

2.4.1 Thermoelastic Stresses

Microstresses in two-phase materials are conventionally understood in terms of the thermoelastic effects that arise upon cooling due to the difference in thermal expansion between the two phases. As the thermoelastic coefficient (TEC) of silicon is smaller than the TEC of SiC, one would anticipate that, upon cooling the silicon would endure a compressive residual microstress and the SiC would have a corresponding tensile residual microstress. Thermoelastic stresses are in the correct sense (compressive in silicon, tensile in SiC), but is the magnitude of the values measured by Raman consistent with thermoelastic stresses? We examined the microstress induced from a coefficient of thermal expansion (CTE) mismatch. A CTE mismatch calculation was done for silicon and SiC using the classical model developed for thermoelastic microstress in two-phase composites by Kingery[20], which is based on the work of Turner[19,20].

Both silicon and SiC have CTEs that vary with temperature. CTE curves from the literature were used[21,22]:

$$\alpha_{SiC} = 3.19 * 10^{-6} + 3.60 * 10^{-9}T - 1.68 * 10^{-12}T^2 \quad [°C^{-1}] \qquad [3]$$

$$\alpha_{Si} = \begin{pmatrix} 3.725\{1 - \exp[-5.88 * 10^{-3}(T - 124)]\} \\ +5.548 * 10^{-3}T \end{pmatrix} * 10^{-3}\ [K^{-1}] \qquad [4]$$

where α is the coefficient of thermal expansion and *T* is the temperature. The thermoelastic Kingery-Turner solution follows the form:

$$\sigma_i = (\alpha_r - \alpha_i)\Delta T K_i = \Delta\alpha\Delta T K_i \qquad [5]$$

where σ is the stress, K is the bulk modulus for that phase, α is the coefficient of thermal expansion, and ΔT is the difference between the initial and final temperature. The

subscript *i* denotes the phase in which the stress is being calculated. The subscript *r* denotes the CTE of the mixture of the two phases and can be expressed as:

$$\alpha_r = \frac{\frac{\alpha_1 P_1 K_1}{d_1} + \frac{\alpha_2 P_2 K_2}{d_2}}{\frac{P_1 K_1}{d_1} + \frac{P_2 K_2}{d_2}} \quad [6]$$

For this expression, P is the weight fraction and d is the density. 1 and 2 denote the properties for silicon and SiC, respectively. We can simplify P/d to volume fraction, V_i:

$$\alpha_r = \frac{\alpha_1 K_1 V_1 + \alpha_2 K_2 V_2}{K_1 V_1 + K_2 V_2} \quad [7]$$

We can then solve α_r using the CTEs in Eq. 3 and Eq. 4 as well as the relevant values found in Table 2.III. We will keep the α_r term for simplicity purposes. We then integrated Eq. 5 from the melting temperature of silicon (1410°C) to room temperature (25°C):

$$\sigma_i = K_i \int_{1410}^{25} (\alpha_r - \alpha_i) dT \quad [8]$$

Results of Eq. 7 can be seen in Table 2.IV for both phases in each material. The thermoelastic microstresses calculated from the CTE mismatch are about 0.045 GPa compression for the silicon phase and 0.014-0.030 GPa tension in the SiC phase. These thermoelastic values more than an order of magnitude lower than the measured residual microstress. Therefore, we know that the microstress measured using Raman spectroscopy is not entirely due to CTE mismatch.

2.4.2 Stress from Crystallization Expansion of Silicon

With the thermoelastic mismatch so low, we will turn our attention to the crystallization expansion of silicon. During the MI process, there is residual silicon which

expands when it solidifies. The expansion of the silicon places the solid silicon in a state of compression, as the silicon expansion is constrained by the surrounding rigid network of silicon carbide. The silicon carbide network is then in a state of tension to balance the stress in the silicon. This phase transformation produces the correct sense of the residual stresses observed by Raman spectroscopy.

We will now concern ourselves with the magnitude of the stress developed by the crystallization expansion of the silicon. The density of solid silicon at 1410°C is 2.32 g/cm^3 and the density of liquid silicon at 1410°C is 2.57 g/cm^3. Therefore, when the silicon transforms from liquid to solid, there is a volumetric expansion in the silicon phase of about 11%. This results in a linear crystallization expansion strain, $\varepsilon_{CES} = 0.362$.

To evaluate the stress developed by this strain, we will modify the classical Kingery-Turner thermoelastic model so that it can be used with crystallization expansion strain rather than thermal expansion mismatch strain. Since the $\alpha\Delta T$ portion of the relationship represents a strain, we can substitute the CTE mismatch strain for the crystallization expansion strain (CES) of the silicon during the phase transformation.

Since α_r represents the CTE for the two-phase mixture, we will start by relating that to the strain of the two-phase mixture ($\varepsilon_{Si\text{-}SiC}$) in this way:

$$\varepsilon_{Si-SiC} = \alpha_r \Delta T = \frac{\alpha_{Si} K_{Si} V_{Si} + \alpha_{SiC} K_{SiC} V_{SiC}}{K_{Si} V_{Si} + K_{SiC} V_{SiC}} \Delta T \qquad [9]$$

We can then substitute the CTE strain ($\alpha\Delta T$) for the strain associated with the phase transformation. SiC does not undergo a phase transformation, so $\alpha_{SiC}\Delta T = 0$. Silicon does transform, and $\alpha_{Si}\Delta T = \varepsilon_{CES}$:

$$\varepsilon_{Si-SiC} = \frac{\varepsilon_{CES} K_{Si} V_{Si}}{K_{Si} V_{Si} + K_{SiC} V_{SiC}} \qquad [10]$$

We can then use this in Eq. 5, which results in:

$$\sigma_i = \varepsilon_{Si-SiC} K_i - \alpha_i \Delta T K_i \quad [11]$$

where $\alpha_i \Delta T$ is the expansion of the *i* phase. Again, for SiC this value is 0, and for silicon, this is the crystallization expansion strain, ε_{CES}. Thus, we can conclude an expression for the stress in SiC:

$$\sigma_{SiC} = \varepsilon_{Si-SiC} K_{SiC} \quad [12]$$

and for silicon:

$$\sigma_{Si} = K_{Si}(\varepsilon_{Si-SiC} - \varepsilon_{CES}) \quad [13]$$

The results of the Kingery-Turner adaptation for CES can be seen in Figure 2.5.

In examining the curves from Eq. 12 in Figure 2.5a, we see that stress in the SiC phase increases nearly linearly with increasing amounts of unreacted free silicon. As for the stress in the silicon phase shown in Figure 2.5b, we see a nearly linear relationship again. However, the magnitude range of stress in silicon is much less than that of the range expressed in the SiC phase. The Kingery-Turner model modified for CES shows that the majority constituent has a larger variation in stress than the minority constituent. In the region of interest, the SiC phase has a range of nearly 2 GPa, while the silicon only ranges by about 0.5 GPa.

Based on these equations derived from the modified Kingery-Turner model, we can calculate the expected magnitude of residual microstress in the silicon and SiC phases. The results can be seen in Table 2.IV. The table shows 2.28 GPa of compression in the free silicon and 0.72 GPa tension in the SiC phase for SC-2. For KX01, we calculate 2.05 GPa of compression in the free silicon and 1.48 GPa tension in the SiC phase.

From Figure 2.5 and Table 2.IV, we see that the modified Kingery-Turner model under-estimates the stress in SiC by a large amount. Based on the model, one would expect to see a large variation in the SiC microstresses of the two materials. However that is not what is measured.

The modified model seems to capture the measured values for free silicon in these two materials very well. For both materials, the microstress in the SiC phase is much less than what is observed. Why is one phase modeled well with the Kingery-Turner modification, and the other phase does not fit reasonably at all? One reason may be a result of the probing depth of Raman spectroscopy.

2.4.3 Raman Spectroscopy Probe Depth

Raman spectroscopy is considered a surface technique, however, the depth of the probe is dependent on the laser wavelength and the absorption coefficient of the material being examined. As was mentioned previously, we are using a 532 nm green laser for excitation. For SiC, this has an absorption coefficient of 35.2cm^{-1} for a 532 nm laser[23]. This corresponds to an average optical penetration depth of approximately 285 microns into crystalline SiC. Therefore, SiC is relatively transparent to the laser source, and the Raman measurements can be thought of as a bulk measurement for crystalline SiC.

For crystalline silicon, the absorption coefficient for 532 nm green light is 115,000cm^{-1}. This is a significantly higher absorption rate than SiC, and results in an absorption length of 87 nm. Silicon is therefore, relatively opaque to green light. Therefore, in a pure silicon sample, the measured microstress would come purely from the surface and for a pure SiC sample, the measured microstress for SiC would be a combination of a surface measurement and a bulk measurement. In the case of RBSiS,

the SiC is somewhat transparent to green light, as a result, the opaque silicon can be measured under semi-transparent SiC grains (Figure 2.6).

In Figure 2.6, we have the microstructure of a polished surface of low-Si material. Since we assume the material to be homogeneous in all directions, we can imagine this image as a cross-section where the excitation probe is incident on the top of the image, illustrated as arrows. The SiC grains are transparent to the 532 nm excitation beam, but once the laser wavelength comes in contact with a silicon grain, it is absorbed over a very small length. However, we still receive signal from the surface as well as approximately one SiC grain size deep in the bulk.

The result is that we obtain a surface measurement as well as a measurement of the stress at every distance up to one grain size deep. This makes the stress analysis more complicated. Gouadec et al. discusses the difference between assuming a bulk measurement in a transparent material versus a surface measurement in an opaque material[24]. For a bulk measurement, the assumption is that the stress measured with Raman spectroscopy is the hydrostatic stress state of the material. However, at the surface, the stress measured would be purely planar.

The stress measured is based off of the average for the entire area being examined. It is unknown at this time what fraction of the stress measured comes from the planar stress near the surface or from the hydrostatic stress in the bulk of the material. Similarly, it is unknown at what length scale the measurement shifts from being a surface, planar measurement, to a bulk, hydrostatic measurement.

2.5 Conclusion

There are intense microstress in the constituent phases of reaction boned silicon carbide SiC and free silicon that have previously not been discussed in the literature. The free silicon phase carries compressive stress on the order of 1.7-2 GPa, while the silicon carbide phase carries a tensile stress in the range of 2.1-2.4 GPa. The measured microstresses in the silicon phase and the SiC phase are much larger than what a CTE mismatch can account. We have shown that the large residual microstress state in MI-RBSiC can be attributed to the volumetric changes during crystallization of the unreacted silicon. We have modified the Kingery-Turner thermoelastic stress model to determine the stress in the silicon and SiC phases anticipated from crystallization expansion strain. The modified model is in good agreement with the stress measured in the silicon phase for both the material examined. The modified model under predicts the stress in the SiC phase. We have analyzed the probe depth of the Raman spectroscopy and found that the measured values are a result of surface measurements as well as approximately 1 SiC grain size deep.

2.6 Acknowledgement

The authors thank Professor Michael Morris for guidance and use of the Raman microscopy equipment in his laboratory. We have appreciated working with him immensely.

References

1. Luthra K, Singh R, Brun MK. Toughened Silcomp Composites - Process and Preliminary Properties. *Am Ceram Soc Bull*. 1993;72:79.

2. Popper P, ed. *Special Ceramics*. London: British Ceramic Research Association; 1960.

3. Chiang Y-M, Messner RP, Terwilliger CD, Behrendt DR. Reaction-Formed Silicon Carbide. *Mater Sci Eng*. 1991;63(144):1-2.

4. Snead LL, Nozawa T, Katoh Y, Byun T-S, Kondo S, Petti DA. Handbook of SiC Properties for Fuel Performance Modeling. *J Nucl Mater*. 2007;371:329-377.

5. Zhou H, Singh RN. Processing and Microstructural Characterization of Melt-Infilitrated Si/SiC Composites. *J Mater Synth Process*. 1997;5:125-134.

6. Singh M, Behrendt DR. Studies on the Reactive Melt Infilitration of Silicon and Silicon-Molybdenum Alloys in Porous Carbon. *Annu Meet Am Ceram Soc*. 1992;(94).

7. Sawyer GR, Page TF. Microstructural Characterization of "REFEL" (Reaction-Bonded) Silicon Carbides. *J Mater Sci*. 1978;13:885-904.

8. Hillig WB. Melt Infiltration Process for Making Ceramic Matrix Composites. In: Mazdiyasni KS, ed. *Fiber Reinforced Ceramic Composites*. Park Ridge, NJ: Noyes Publications; 1990:261-277.

9. Wiederhorn SM, Hockey BJ, French JD. Mechanisms of Deformation of Silicon Nitride and Silicon Carbide at High Temperatures. *J Eur Ceram Soc*. 1999;19:2273-2284. http://www.ewp.rpi.edu/hartford/users/papers/engr/ernesto/barthc2/EP/Other/References/[23].pdf. Accessed 1999.

10. Colomban P, Gouadec G, Mathez J, Tschiember J, Peres P. Raman Stress Measurement in Opaque Industrail C/Epoxy Composites Submitted to Tensile Strain. *Intern Stress Polym Compos*. 2006;37(4):646-651.

11. Watts J, Hilmas G, Fahrenholtz WG, Brown D, Clausen B. Stress Measurements in ZrB2-SiC using Raman Spectroscopy and Neutron Diffraction. *J Eur Ceram Soc*. 2010;30:2165-2171.

12. Ferralis N. Probing Mechanical Properties of Graphene with Raman Spectroscopy. *cond-mat.mtrl-sci*. 2010:1-16.

13. Sciti D, Guicciardi S, Celotti G, Deluca M, Pezzotti G. Residual Stress Investigation in SiC/MoSi2 Composites. *Adv Eng Mater*. 2007;9:393-399.

14. Anastassakis E, Cantarero A, Cardona M. Piezo-Raman measurements and anharmonic parameters in silicon and diamond. *Phys Rev B*. 1990;41:7529-7535.

15. DiGregorio JF, Furtak TE. Analysis of Residual Stress in 6H-SiC Paricles within Al2O3/SiC Composites through Raman Spectroscopy. *J Am Ceram Soc*. 1992;75:1854-1857.

16. DiGregorio JF, Furtak TE, Petrovic JJ. A Technique for Measuring Residual Stress in SiC Whiskers within an Alumina Matrix through Raman Spectroscopy. *J Appl Phys*. 1992;71:3524-3531.

17. Esmonde-White KA, Esmonde-White FWL, Morris MD, Roessler BJ. Fiber-optic Raman Spectroscopy of Joint Tissues. *Analyst*. 2011;136:1675-1685.

18. Esmonde-White FWL, Morris MD. Raman Imaging and Raman Mapping. In: *Emerging Raman Applications and Techniques in Biomedical And Pharmaceutical Fields*. Springer-Verlag; 2010:97-110.

19. Kingery WD. Note on Thermal Expansion and Microstresses in Two-Phase Compositions. *J Am Ceram Soc*. 1957;40(10):351-352.

20. Turner PS. Thermal-Expansion Stress in Reinforced Plastics. *J Am Ceram Soc*. 1946;37(4):239-250.

21. Li Z, Bradt RC. Thermal Expansion and Thermal Expansion Anisotropy of SiC Polytypes. *J Am Ceram Soc*. 1987;70:445-448.

22. Hull R. *Properties of Crystalline Silicon*. London: INSPEC; 1999.

23. Derst G, Wibertz C, Kalbitzer S, Kratschmer W, Bhatia KL. Optical Properties of SiC for Crystalline/Amorphous Pattern Fabrication. *Appl Phys Lett*. 1989;54(18):1722-1724.

24. Gouadec G, Makaoui K, Perriere L, Colomban P, Mazerolles L. Ruby Micro-Piexospectroscopy in GdAlO3/Al2O3(/ZrO2), Er3Al2O12/Al2O3(/ZrO2) and Y3Al5O12/Al2O3(/ZrO2) Binary and Ternary Directionally Solidified Eutectics. *J Eur Ceram Soc*. 2012;(32):2145-2151.

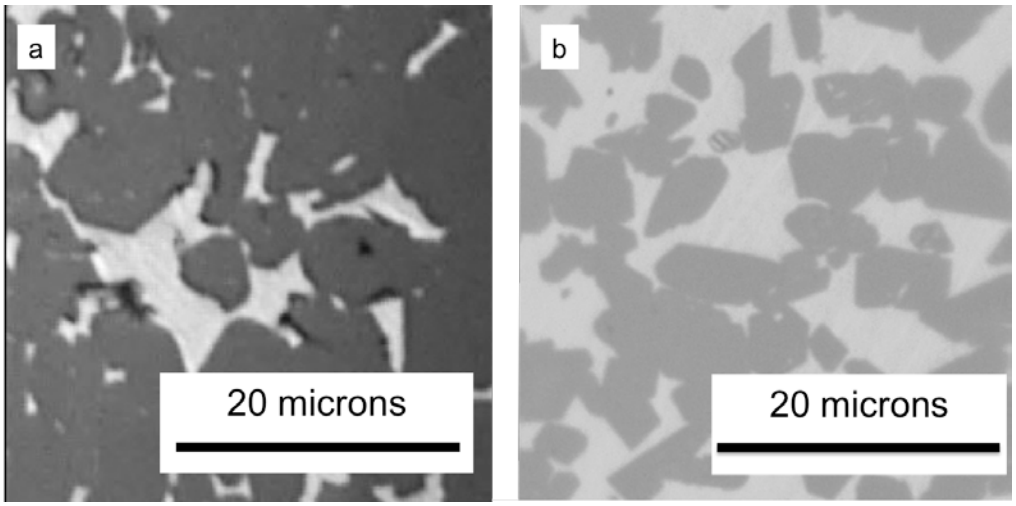

Figure 2.1. Light grey is unreacted free silicon and dark grey is SiC. a is an image of SC-2 RBSiC received from Coors Tek with 24 vol% unreacted free silicon. b is an image of KX01 with 42 vol% unreacted free silicon.

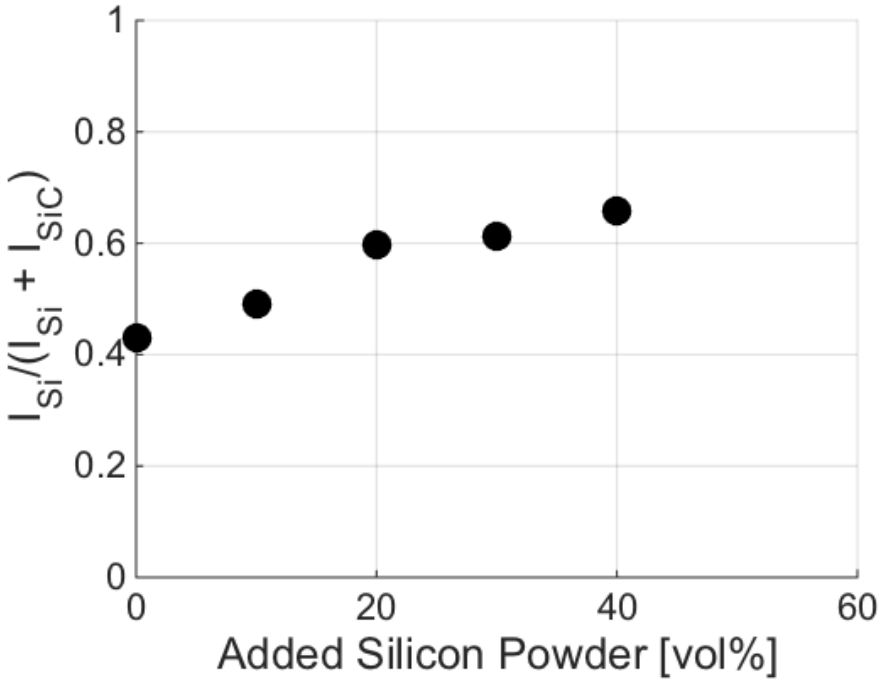

Figure 2.2. Sum of the integrated intensities of the silicon (111), (220),and (311) powder diffraction peaks divided by the sum of the integrated intensities of the silicon and SiC (101), (102),(103),(104) and (110) diffraction peaks versus the weight percent of powder Si added to the KX01 RBSiC materials.

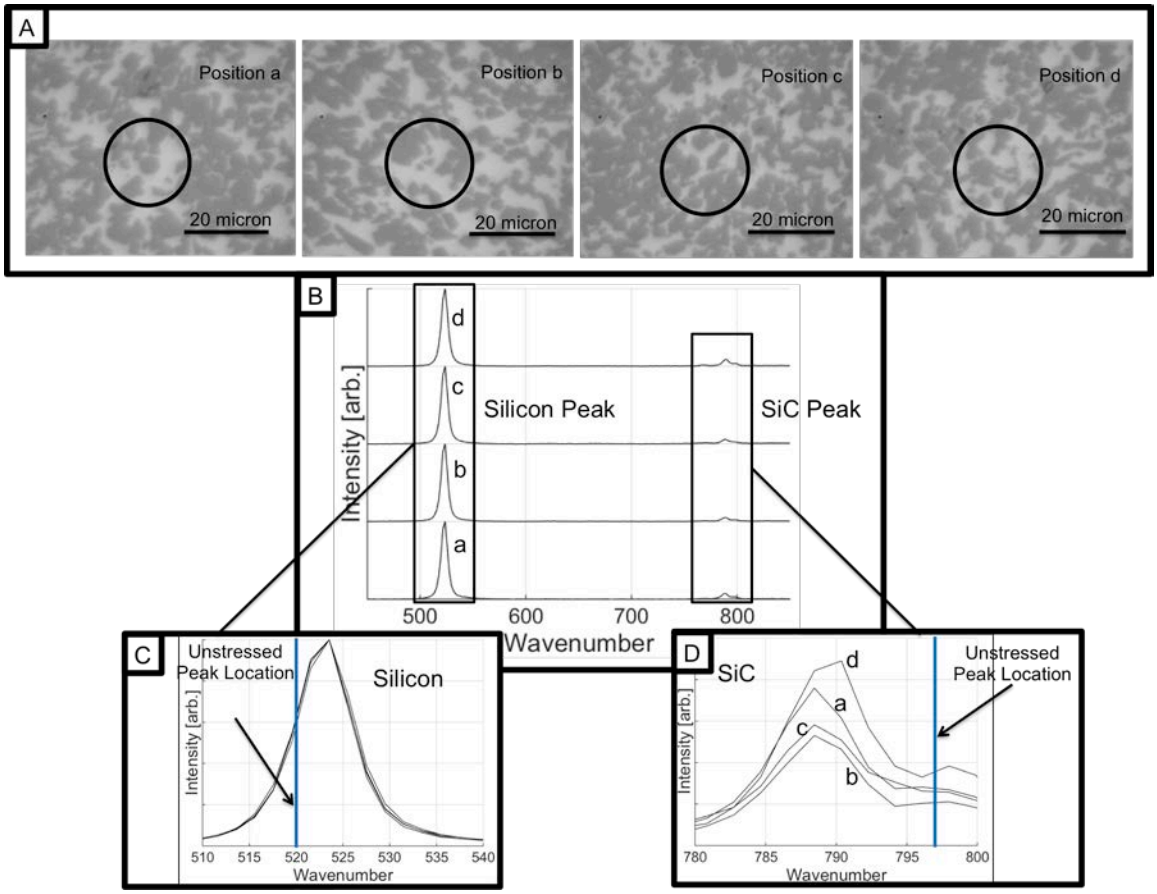

Figure 2.3. The images in part A at the top indicate the positions in the sample where each individual spectrum came from. The black circles indicate the location of the 20 micron diameter Raman probe for four locations in a high-Si sample. Part B is the Raman spectrum for the four locations shown in part A for the high-Si RBSiC. Part C provides detailed Raman spectra of the 520 cm^{-1} peak from silicon with the spectra from the four locations. The solid vertical line indicates the location of the unstressed peak position for silicon (520 cm^{-1}). In part D, we show the detailed Raman spectra of the 797 cm^{-1} peak from SiC with spectra from the four locations. The solid vertical line indicates the location of the unstressed peak position for SiC (797 cm^{-1}).

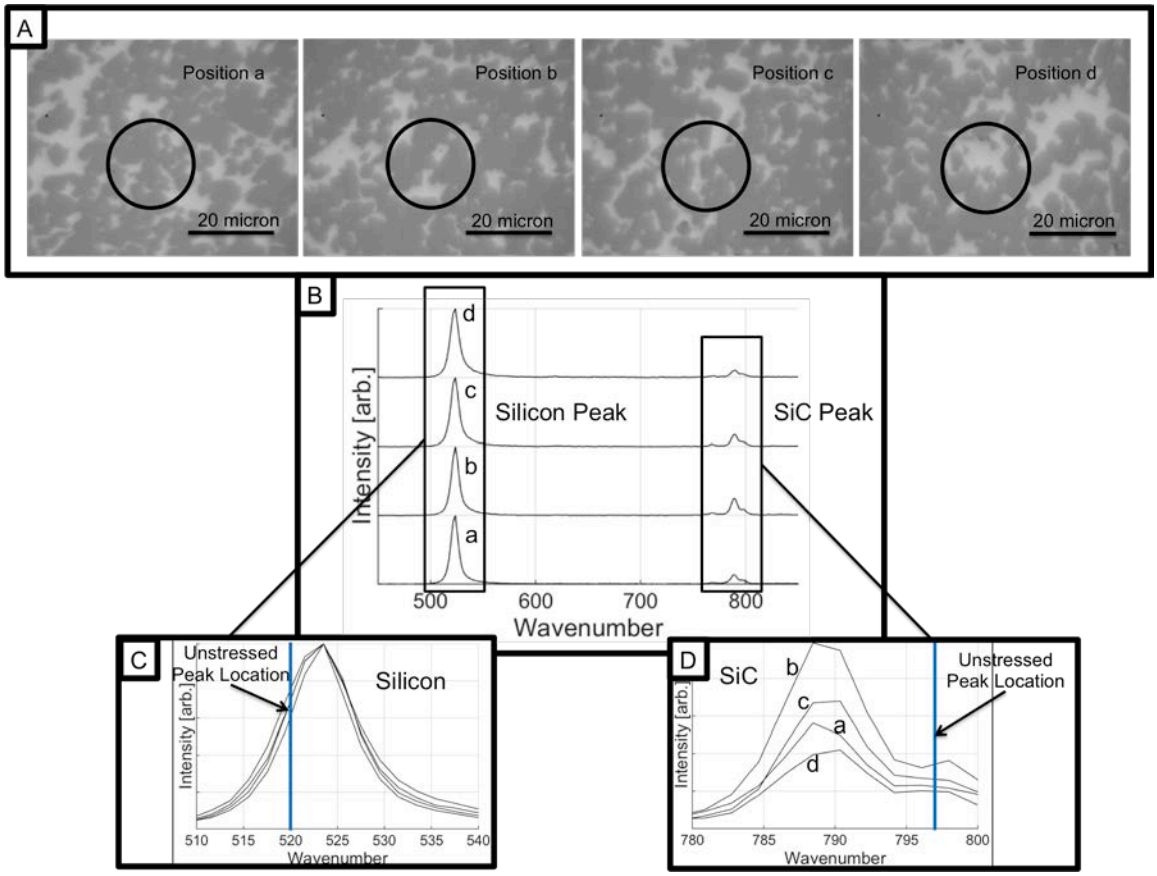

Figure 2.4. The images in part A at the top indicate the positions in the sample where each individual spectrum came from. The black circles indicate the location of the 20 micron diameter Raman probe for four locations in a low-Si sample. Part B is the Raman spectrum for the four locations shown in part A for the low-Si grade RBSiC received from Coors Tek. Part C provides detailed Raman spectra of the 520 cm^{-1} peak from silicon with the spectra from the four locations. The solid vertical line indicates the location of the unstressed peak position for silicon (520 cm^{-1}). In part D, we show the detailed Raman spectra of the 797 cm^{-1} peak from SiC with spectra from the four locations. The solid vertical line indicates the location of the unstressed peak position for SiC (797 cm^{-1}).

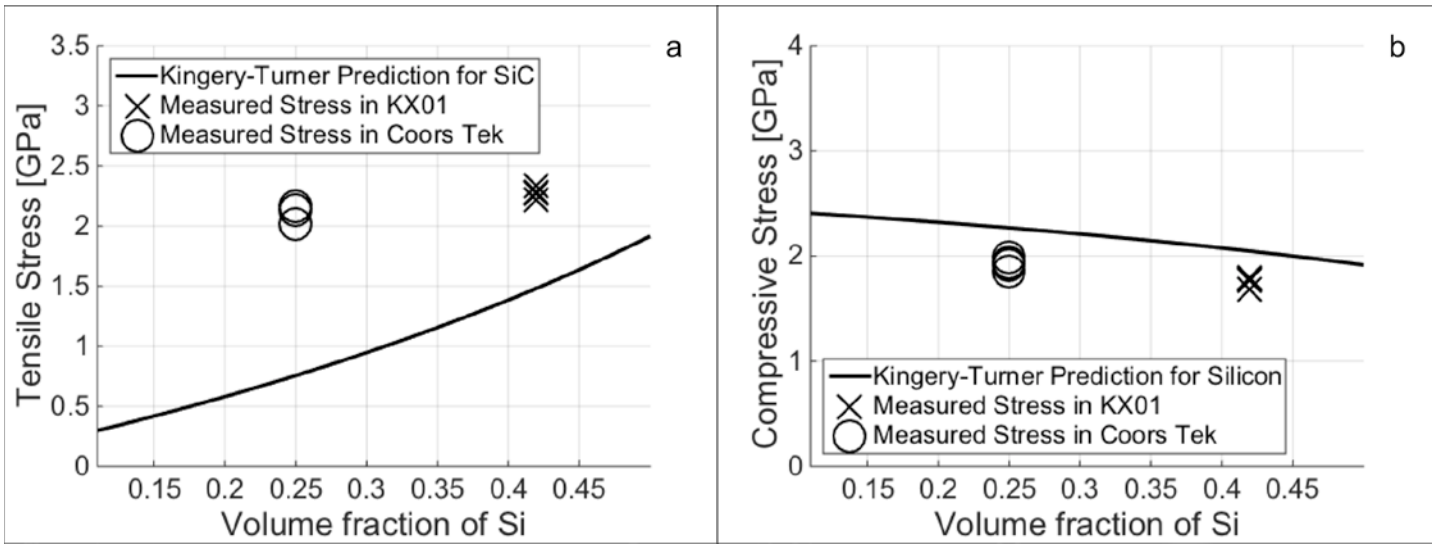

Figure 2.5. Results of the Kingery-Turner Crystallization Expansion modification along with the measured microstress values, displayed as a function of the volume fraction of free silicon determined through XRD. Figure 5a shows the results for the tensile stress in the SiC phase and Figure 5b shows the results for the compressive stress in the free silicon phase.

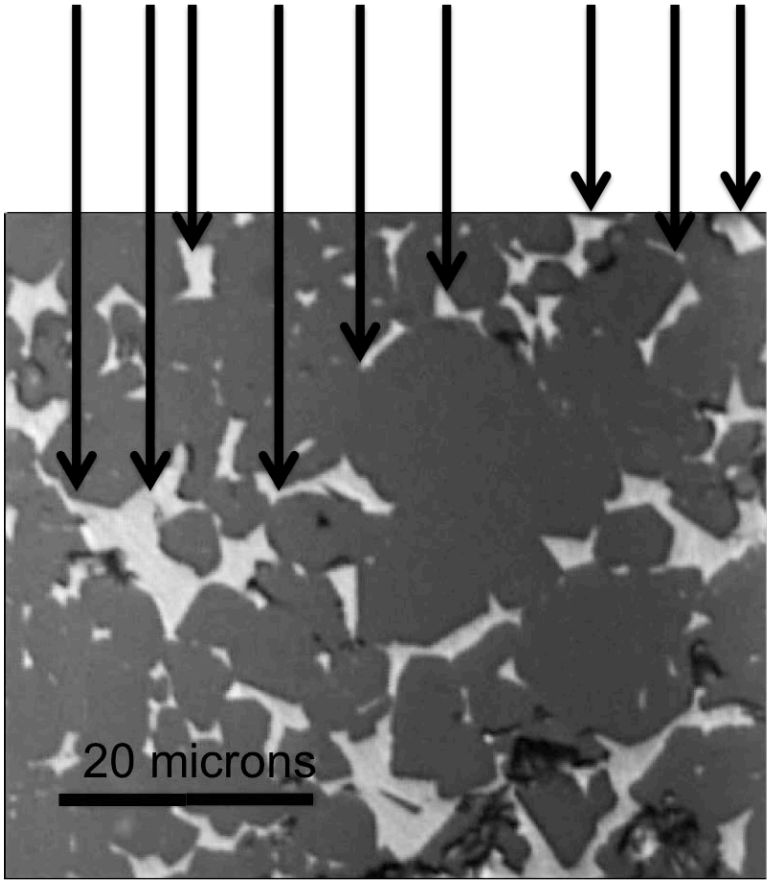

Figure 2.6. Image of SC-2 as if it were viewed from the top. The illuminating laser light (indicated with black arrows) collects Raman information from the opaque silicon grains at the surface as well as subsurface silicon grains viewed through the transparent SiC grains.

Table 2.I. Results of peak fitting the Raman spectrum of the positions specified in Figure 2.3 and Figure 2.4

Material	Position	Silicon Peak Position [cm^{-1}]	Compressive Microstress in Silicon [GPa]	SiC Peak Position [cm^{-1}]	Tensile Microstress in SiC [GPa]
High-Silicon	a	522.92 ± .04	1.74 + .03	788.62 ± .13	2.37 ± .04
	b	522.88 ± .05	1.77 ± .03	788.81 ± .09	2.32 ± .02
	c	522.97 ± .05	1.77 ± .03	789.26 ± .33	2.19 ± .09
	d	523.16 ± .04	1.88 ± .03	789.47 ± .12	2.13 ± .03
Low-Silicon	a	522.97 ± .07	1.77 ± .04	789.47 ± .38	2.13 ± .11
	b	523.50 ± .06	2.08 ± .04	789.42 ± .27	2.15 ± .08
	c	523.20 ± .09	1.90 ± .05	789.60 ± .32	2.10 ± .09
	d	523.09 ± .11	1.84 ± .06	789.79 ± .39	2.43 ± .11

Table 2.II. Results for Silicon Microstress state from Raman Spectroscopy in RBSiC

Material	Sample Name	Compressive Residual Microstress in Silicon [GPa]	Tensile Residual Microstress in SiC [GPa]
Low-Silicon	CT-HT-01	1.85 ± .16	2.16 ± .11
	CT-HT-02	1.99 ± .08	2.15 ± .11
	CT-HT-03	1.90 ± .07	2.13 ± .08
	CT-HT-04	1.94 ± .10	2.16 ± .14
High-Silicon	KX01-6D-01	1.68 ± .13	2.33 ± .10
	KX01-6D-02	1.77 ± .22	2.27 ± .06
	KX01-6D-03	1.78 ± .12	2.28 ± .11
	KX01-6D-04	1.79 ± .11	2.22 ± .12

Table 2.III. Relevant values used in Kingery-Turner equations

Material	Phase	K [GPa]	V [%]
Low-Silicon	Silicon	69	24
	SiC	227	76
High-Silicon	Silicon	69	42
	SiC	227	58

Table 2.IV. Predicted values and measured values for stresses in SiC and silicon

Material	Average Measured Compressive Microstress in Silicon [GPa]	Compressive Microstress in Silicon from Thermoelastic Kingery-Turner model [GPa]	Compressive Microstress in Silicon from Crystallization Strain - Modified Kingery-Turner model [GPa]	Average Measured Tensile Microstress in SiC [GPa]	Tensile Microstress in SiC from Thermoelastic Kingery-Turner model [GPa]	Tensile Microstress in SiC from Crystallization Strain - Modified Kingery-Turner model [GPa]
Low-Silicon	1.92 ± .11	0.046	2.28	2.12 ± .22	0.015	0.72
High-Silicon	1.76 ± .15	0.042	2.05	2.28 ± .10	0.030	1.48

Chapter 3 Microstresses in the Matrix of a Melt-Infiltrated Reaction Bonded Silicon Carbide Ceramic Matrix Composite[2]

3.1 Introduction

Fiber-reinforced ceramic matrix composites (CMCs) are important for many applications to reduce weight[1,2] and increase temperature capabilities[3]. Composites with silicon carbide fibers with a silicon carbide matrix (SiC/SiC) are an important class of CMCs. The matrix SiC can be produced by infiltration and pyrolysis of a SiC-precermic polymer[4,5], by chemical vapor infiltration[6,7], or by melt infiltration[8,9]. This chapter concerns the HiPerComp™ material, a SiC fiber reinforced composite with a reaction bonded matrix produced by infiltration of molten silicon into a carbonaceous preform (MI SiC/SiC CMC)[10]. These melt infiltrated composites have a matrix which is almost free of porosity, but often has unreacted free silicon, so the matrix has two important phases, SiC and free silicon.

We have reported that the free silicon phase in monolithic reaction bonded silicon carbide (RBSiC) has intense compressive microstress, while the SiC phase has tensile microstress in Chapter 2. These microstress originate from the expansion of the free silicon phase as the liquid silicon freezes to the less-dense crystalline silicon during cooling from the melt infiltration temperature. Here we show similar behavior for the free silicon and matrix SiC in an MI-SiC/SiC CMC.

---

[2] This chapter has been submitted for review to the Journal of Composites B on October 8, 2015

3.2 Methods

3.2.1 Material

We will be examining a commercial MI-RBSiC/SiC CMC manufactured by GE Aviation. The composite, HiPerComp™, is a continuous fiber reinforce composite produced by melt-infiltration using silicon carbide fibers with a boron nitride (BN) interphase coating[9]. The architecture of this composite is a laminate of eight plies of uniaxial fibers with [0/90]2s layup, resulting in a through-thickness of ~2 mm. The samples represented in this paper are all cut from a single panel using a slow-speed diamond saw. Each sample is approximately 10 x 25 x 2 mm.

The melt infiltration (MI) process results in an RBSiC matrix with ~20 ± 5 vol% unreacted free silicon determined by quantitative XRD. To determine the free silicon amounts, the method of standards was used. The details are presented in Chapter 2, but briefly, pulverized samples of the composite were combined with known amounts of powdered silicon. We then compared the integrated intensities of the three silicon peaks ((111), (220), and (311) peaks) and the four SiC peaks (silicon peaks and (101), (102), (103), (104), and (110) α-SiC peaks). The β-SiC (111) and (220) peaks are close to the α-SiC peaks (102) and (110) peaks, so this procedure captures both alpha-and beta-silicon carbide. The total peak intensity of silicon peaks and SiC peaks were determined for mixtures of pulverized composite with added silicon, with the total amount of silicon in the powder. This included the amount added as well as the amount of silicon in the CMC. We are then able to determine the linear relationship between the intensity ratio and the exact amount of free silicon to within ±5 vol% for the panel examined.

We are examining the residual microstress state in the two phases in RBSiC. We seek to measure the microstresses in the free silicon and the SiC phases in the RBSiC. We will be investigating the stress in the silicon and SiC grains of the matrix.

3.2.2 Microstress Measurement

We used Raman spectroscopy to measure the residual microstress in the matrix RBSiC of this CMC. Raman spectroscopy has been shown effective in measuring the residual microstress in both silicon[11,12] and SiC[13–15]. For a Raman active material, there is a characteristic wavenumber associated with the bonding to particular Raman modes. A stress in the material causes the characteristic wavenumber of the Raman mode to shift, with blue shift for tension and red shift for compression The difference between the characteristic wavenumber and the shifted wavenumber ($\Delta\omega$) can be directly related to the stress (σ) applied to the material through the Raman coefficient, R:

$$\Delta\omega = R\sigma \qquad [1]$$

We will use Raman coefficients from the literature. For silicon, we use the $q \approx 0$ optical phonon Raman peak at 520 cm^{-1}, for which R_{Si} = 1.88 ± 05 cm^{-1}/GPa as determined by Anastakakis[16]. For polycrystalline SiC, we use the full triplet transverse optic (TO) phonon mode Raman peak at 797cm^{-1}, for which used 3.53 ± 0.21 cm^{-1}/GPa as determined by DiGregorio[17]. This has been shown to be consistent for α and β-SiC[18].

The stress values reported are the results of subtracting the known, unstressed peak location from the measured stressed peak location. As these peaks are broad some uncertainty is introduced. The uncertainty is larger in the SiC because the transverse optic phone around 797cm^{-1} has to be fit as a triplet and is only about 20% as intense as the simple silicon peak at 520cm^{-1}.

The peak locations were measured using a custom system set up with the assistance of Dr. Francis Esmonde-White[19,20]. The details are in Chapter 2, but briefly, we used a 532nm green laser for excitation. The laser was fed into a collimator via a fiber optic cable. The collimated

beam is refracted toward the Nikon Eclipse ME600L microscope using a dichroic filter. The laser travels through the optics of the microscope and is incident on the sample with a spot size of 20 microns. This ensures that multiple silicon and SiC grains are being sampled at every position. Some of the excited photons pass back through the microscope optics toward the dichroic filter. The excited photons go through two filters to remove the reflected 532nm wavelength as well as any excitation incurred from the fiber optic cable before being collimated again. The filtered, collimated photons are separated based on energy levels with the HoloSpec VPT spectrograph and are read to the computer with the Newton EM CCD. We used a two-system calibration method. First, we calibrated the CCD using an argon light emission spectrum. We then calibrated the laser separately using acetaminophen.

Fourteen samples were analyzed. Each sample was examined as-manufactured. All samples were polished to a 1 micron finish with a non-aqueous solution. Twenty measurements were taken for each sample. Care was taken to ensure that the spectra were collected from a region of matrix at least 20 microns from a fiber, since fluorescence from the BN coating on the fiber interfered with the Raman spectra. Spectra were collected from 280 locations, providing pairs of microstress measurements for the silicon and SiC phases. Peak fitting was done manually using Origin 9.1 software. The measured microstress in the 20 locations was averaged together to determine the microstress value reported for each individual sample.

3.3 Results

3.3.1 Microstructure and Free Silicon

A polished cross section appears in Figure 3.1. Here we see alternating lamina containing longitudinal SiC fibers (visible by their polished cross section or by the long voids from fiber pulled out during polishing) and lamina with transverse fibers (visible from the round fiber cross-

sections). Notice that each fiber-containing ply is about 200 microns thick, and the plies are separated by a layer of RBSiC matrix which is about 100 microns thick (Figure 3.1). The area of concern is the thick center layer that contains only the matrix. All measurements were taken from this region to avoid the florescence of the BN coatings, as well as for consistency.

It is difficult to obtain clear contrast in the SEM between the matrix SiC and the free silicon, so a polished sample was etched with KOH to dissolve the silicon. A secondary electron image of the microstructure in this region can be seen in part B of Figure 3.1. The voided regions represent where the silicon was during the measurements. Etching away the silicon was done only for imaging purposes. No Raman measurements were taken on samples with silicon etched out.

The free silicon is known to be an interconnected phase[21]. The size of the interpenetrating silicon veins is on the order of a few hundred nm. The individual matrix SiC grains are not resolved in Figure 3.1B, but from the outline of the etched silicon, it is possible to infer that the SiC grain size is on the order of 1 micron.

Raman spectra were collected in the central matrix region, as illustrated by the box in Figure 3.1A. Reflected light images of four representative locations are shown in Figure 3.2. The spots where the spectra were collected are shown as black rings (~20microns in diameter), and the mottled contrast indicates the darker SiC and brighter free silicon. Since the SiC grains are approximately 1 micron, and the silicon grains are much smaller, the 20 micron spot size shown inFigure 3.2 is sampling multiple grains of both phases. Spectra are collected from ~300 SiC grains per scan, which we can presume have random crystallographic orientation. The free silicon phase, present as an interconnected phase a few hundred nanometers thick between the

SiC, crystallizes as single crystal domains several microns in size[22]. The 20 micron spot size samples many of these so we treat the free silicon as random polycrystals.

In Figure 3.3A, we provide the full Raman spectra for each of the regions pictured in Figure 3.2. Each individual spectrum contains the q≈0 phonon peak for silicon (near 520 cm^{-1}) as well as the TO peak for SiC (near 797 cm^{-1}). The silicon peaks for the four locations are shown in detail in part B of Figure 3.3. The vertical black line shows the position of the unstressed q≈0 phonon peak at 520 cm^{-1}. The measured silicon peaks are sharp and well defined. The red dotted line indicates the curve fit used to determine the peak position. At all four locations, the Raman peak shifts to higher wavenumber, indicating a compressive stress in the silicon.

Similarly, we show the TO SiC peaks for each position in part C of Figure 3.3. Due to the triplet splitting, the SiC TO peak is much broader. The SiC peaks are less distinct, but peak fitting shows that they are have been shifted to lower wavenumber, consistent with tensile stresses in the silicon carbide.

The peak positions and calculated hydrostatic stresses inferred from the wavenumber shift $\Delta\omega$ for the spectra collected from these four representative locations can be seen in Table 3.I. The variability in the calculated microstress, amounting to 0.1-0.2 GPa, comes from the uncertainty in the peak positions from the peak fitting. To establish the repeatability of the Raman spectra themselves, at several locations the spectra were collected 3 times. The peak positions obtained by fitting the spectra were within the uncertainty of the peak fit, i.e, within 0.2 cm^{-1} for the silicon and within 0.7 cm^{-1} for the SiC.

Notice the variability in the microstress. For the silicon, with a simple peak, the peak position varies by about 6% between the four locations. The average inferred compressive stress for these four positions is about 2.8 GPa, varying from 2.4 to 3.1 GPa, or about a 15% variation

in the compressive stress in the free silicon. The magnitude of the tensile stress inferred for the SiC shows about the same magnitude of variability. The average tensile stress for these four locations is 0.54 GPa, and it varies from 0.24 to 0.75 GPa.

3.3.2 Position to Position Variation

Figure 3.4 shows the stress data for the 20 positions of a single sample. We have plotted the data as pairs of points (σ_{Si} and σ_{SiC}) calculated from the $\Delta\omega_{Si}$ and $\Delta\omega_{SiC}$ from fitting the spectra at each position. It is convenient to present these data as plots with tensile stress in SiC in the vertical axis and compressive stress in the free silicon in the horizontal axis, so that a point can represent each pair.

For this single sample, we see variation in the measured tensile stress from nearly 0 GPa up to about 1.4 GPa. For the compressive stress in the silicon phase, we see a variation from about 2.5 GPa to 3.5 GPa. The silicon shows slightly lower variation than what is examined in the SiC phase for this sample. The error bars plotted in Figure 3.4 represent the error in the peak fitting. The error in the compressive stress in the silicon phase averages out to be about ±0.1 GPa. The average error in the SiC phase is about double that of the silicon phase, ±0.2 GPa. This error is consistent for all the samples in this study.

For each sample, 20 different positions were imaged. A plot of all the points can be seen in Figure 3.5. In this figure, we see that there is significant variation within the system being studied. Remember, all samples were cut from a single panel.

There is a significant amount of variation within a single panel of the CMC material. We have examined the distribution of this data set and found that this is a normal distribution for both the silicon and SiC phases (Figure 3.6). The mean value for the compressive microstress in

silicon is 2.72 GPa and the mean value for the tensile microstress in SiC is 0.50 GPa. The standard deviation in both data sets is about the same, 0.36 GPa in silicon and 0.33 GPa in SiC.

We have a large confidence in the stress measured in the silicon phase since the peaks are large and narrow. Therefore we know that the stress is different from location to location. In the SiC phase, we are less confident because the low intensity and broad peaks are more difficult to fit. Both the silicon and SiC phases show a normal distribution with very similar standard distributions providing more confidence in the tensile microstress measured in the SiC phase.

3.3.3 Sample to Sample Variation

Figure 3.7 shows the average microstress measured in the 14 samples of the CMC with points. The gray X shows the overall mean microstress value from all of the positions examined. The open circle in the graph is based off of the Kingery-Turner model from Chapter 2. This is a predicted value of the microstress in each phase based on the crystallization expansion of the silicon phase during fabrication of the matrix.

We see that averaging all of the microstress measurements within each sample greatly reduces the apparent variation in the system. The overall mean value for the calculated microstress agrees vary well for the SiC phase and is slightly higher value for the silicon phase.

3.4 Discussion

3.4.1 Prediction of Microstress

In the previous chapter, a thermal expansion stress model was adapted to consider the stress developed during the crystallization of the silicon phase. The initial model determines the stress developed in a two phase mixture from a thermal expansion mismatch strain. The

adaptation substitutes the thermal expansion mismatch strain for the crystallization expansion strain (ε_{CES}).

Briefly, the model uses the same form described in Kingery[23] and Turner[24]:

$$\sigma_i = (\alpha_r - \alpha_i)\Delta T K_i = \Delta\alpha \Delta T K_i \quad [2]$$

where σ_i is the stress in the particular phase, α_i is the coefficient of thermal expansion for the phase of interest, K_i is the bulk modulus for the phase, ΔT is the temperature gradient, and α_r is described by:

$$\alpha_r = \frac{\alpha_1 K_1 V_1 + \alpha_2 K_2 V_2}{K_1 V_1 + K_2 V_2} \quad [3]$$

In Eq. [3] α is the coefficient of thermal expansion, V is the weight fraction of the phase, and K is again the bulk modulus. The 1 and 2 designations are for the two phases being examined. We can expand Eq. [2] to:

$$\sigma_i = \alpha_r \Delta T K_i - \alpha_i \Delta T K_i \quad [4]$$

We know that αΔT is equivalent to a strain. $\alpha_r \Delta T$ therefore describes the strain of the two-phase mixture, and $\alpha_i \Delta T$ is the total strain in each phase. For the crystallization expansion of the silicon phase, we equate

$$\alpha_{Si} \Delta T = \varepsilon_{CES} \quad [5]$$

$$\alpha_{SiC} \Delta T = 0 \quad [6]$$

With this in place, we are able to simplify the strain in the two phase mixture to:

$$\alpha_r \Delta T = \varepsilon_{Si-SiC} = \frac{\varepsilon_{CES} K_{Si} V_{Si}}{K_{Si} V_{Si} + K_{SiC} V_{SiC}} \quad [7]$$

We can make our final substitutions back into Eq. [4] to determine the microstress in silicon carbide and silicon from the crystallization expansion strain:

$$\sigma_{SiC} = \varepsilon_{Si-SiC} K_{SiC} = \frac{\varepsilon_{CES} K_{Si} V_{Si}}{K_{Si} V_{Si} + K_{SiC}(1 - V_{Si})} K_{SiC} \quad [8]$$

$$\sigma_{Si} = K_{Si}(\varepsilon_{Si-SiC} - \varepsilon_{CES}) = K_{Si}\left(\frac{\varepsilon_{CES}K_{Si}V_{Si}}{K_{Si}V_{Si}+K_{SiC}(1-V_{Si})} - \varepsilon_{CES}\right) \quad [9]$$

The averaged measured values of the microstresses are in good agreement with the predicted value from the Kingery-Turner model. We can see that the modified model provides a good reference for the magnitude of stress measured in the matrix of the composite material. Nearly all of the compressive stresses in the silicon phase show a higher magnitude than what the model would suggest. We believe that processing conditions are the cause for this discrepancy.

3.4.2 Position to Position Variation

This level of variation is far greater than what was examined in the previous study of the monolithic RBSiC materials. In the case of the monolithic materials, the only interaction we need concern ourselves with is the expansion of the silicon against the SiC. Therefore, the two-phase mixture has no other boundary conditions outside the two phases.

In the case of the composite, the microstress measured is again due to the crystallization expansion of the silicon against the stiff SiC phase. However, the composite has other components that can affect the local microstress. Besides the SiC phase in the RBSiC matrix, which constrains the expanding silicon, the composite also has a very strong SiC fiber and a very weak boron nitride (BN) debond coating which varies significantly in thickness throughout the composite. These two elements will therefore impact how the microstress develops in the immediate vicinity of the fiber. These effects will diminish as a function of distance from the fiber, but it is unknown at this time what length scale is necessary to mitigate the effects of the stiff fibers and weak BN coatings on the microstress measured in the silicon and SiC phases.

3.4.3 Microstress and Matrix Residual Stress

The microstresses measured in this study do not directly impact the first matrix cracking stress. The tensile stress measured in the SiC phase compensates compression in the free silicon. This balances out on the length scale of a few multiples of the grain size, about 10 microns or so. The crystallization of the silicon does cause an overall net expansion of the Si:SiC two-phase matrix. As will be shown in Chapter 5, it is this matrix expansion that creates the ply level residual stress that affects the macroscopic properties of the CMC.

3.5 Conclusion

In this study, we discovered large residual compressive microstresses in the silicon phase and large residual tensile microstresses in the SiC phase. In the free silicon phase, we measured an average of 2.7 GPa of compression and in the SiC phase, we measured an average of 0.5 GPa of tension. The magnitude and sign of the microstresses measured are consistent with the crystallization expansion of silicon being the cause of the microstress. This was determined using a modification of the Kingery-Turner model. The model estimates the microstress in the SiC phase very well and slightly underestimates the microstress measured in the silicon phase.

We observed significant variation in the measured microstress from position to position among all of the samples testing. The variation follows a normal distribution in both phases examined. We attribute the variation to the complexity of the microstructure in the composite that the monolithic materials do not have.

3.6 Acknowledgement

We would like to thank Elizabeth Getto for her assistance in providing SEM images used in this manuscript.

References

1. Krenkel W, Renz R, Krenkel W, eds. CMCs for Friction Applications. In: *Ceramic Matrix Composites*. Wiley-VCH; 2008:396.

2. Kaya H. The Application of Ceramic-Matrix Composites to the Automotive Ceramic Gas Turbine. *Compos Sci Technol*. 1999;59:861-872.

3. Bansal NP, Lamon J, eds. *Ceramic Matrix Composites: Materials, Modeling, and Technology*. Hoboken, NJ: Wiley; 2015.

4. Yajima S, Hayashi J, Omori M, Okamura K. Development of a Silicon Carbide Fibre with High Tensile Strength. *Nature*. 1976;261:683-685.

5. Ishikawa T, Kojtoku Y, Kumagawa K, Yamamura T, Nagasawa T. High-strength Alkali-resistant Sintered SiC Fibre Stable to 2,200 C. *Lett to Nat*. 1998;391:773-775.

6. Probst KJ, Besman TM, Stinton DP, Lowden RA, Anderson TJ, Starr TL. Recent Adances in Forced-Flow, Thermal-Gradient CVI for Refractory Composites. *Surf Coatings Technol*. 1999;(120-121):250-258.

7. Naslain R, Langlais F, Fedou R. The CVI-Processing of Ceramic Matrix Composites. *Le J de Phys Colloq*. 1989;(50):C191-C207.

8. Zhou H, Singh R. Processing and Microstructural Characterization of Melt-Infiltrated Si/SiC Composites. *J Mater Synth Process*. 1997;5:125-134.

9. Corman GS, Luthra KL. Silicon Melt Infiltrated Ceramic Composites (HiPerComp). In: *Handbook of Ceramic Composties*. New York: Springer; 2005.

10. Hillig WB. Melt Infiltration Process for Making Ceramic Matrix Composites. In: Mazdiyasni KS, ed. *Fiber Reinforced Ceramic Composites*. Park Ridge, NJ: Noyes Publications; 1990:261-277.

11. Huang X, Wu K, Chen M, et al. Temperature Dependence of Raman Scattering in Si Crystalls with Heavy B and/or Ge Doping. *Mater Sci Semicond Process*. 2006;9:257-260.

12. Hart TR, Aggarwal RL, Lax B. Temperature dependence of Raman scattering in silicon. *Phys Rev B*. 1970;1(2):638-642. doi:10.1103/PhysRevB.1.638.

13. Li Z, Bradt RC. Thermal Exansion of the Cubic (3C) Polytype of SiC. *J Mater Sci*. 1986;21:4366-4368.

14. Xiao Z, Yang Y, Jin N, Liu S, Luo X, Huang B. Microstructure and Thermal Residual Stress Analysis of SiC Fiber through Raman Spectroscopy. *J Raman Spectrosc*. 2013. doi:10.1002/jrs.4356.

15. Olego D, Cardona M, Vogl P. Pressure Dependence of the Optical Phonons and Transverse Effective Charge in 3C-SiC. *Phys Rev B*. 1982;25:3878-3888.

16. Anastassakis E, Cantarero A, Cardona M. Piezo-Raman measurements and anharmonic parameters in silicon and diamond. *Phys Rev B*. 1990;41:7529-7535.

17. DiGregorio JF, Furtak TE. Analysis of Residual Stress in 6H-SiC Paricles within Al2O3/SiC Composites through Raman Spectroscopy. *J Am Ceram Soc*. 1992;75:1854-1857.

18. DiGregorio JF, Furtak TE, Petrovic JJ. A Technique for Measuring Residual Stress in SiC Whiskers within an Alumina Matrix through Raman Spectroscopy. *J Appl Phys*. 1992;71:3524-3531.

19. Esmonde-White FWL, Morris MD. Raman Imaging and Raman Mapping. In: *Emerging Raman Applications and Techniques in Biomedical And Pharmaceutical Fields*. Springer-Verlag; 2010:97-110.

20. Esmonde-White KA, Esmonde-White FWL, Morris MD, Roessler BJ. Fiber-optic Raman Spectroscopy of Joint Tissues. *Analyst*. 2011;136:1675-1685.

21. Dunn D. The Effect of Fiber Volume Fraction in HiPerComp SiC-SiC. 2010.

22. Hay R. personal communication. 2013.

23. Kingery WD. Note on Thermal Expansion and Microstresses in Two-Phase Compositions. *J Am Ceram Soc*. 1957;40(10):351-352.

24. Turner PS. Thermal-Expansion Stress in Reinforced Plastics. *J Am Ceram Soc*. 1946;37(4):239-250.

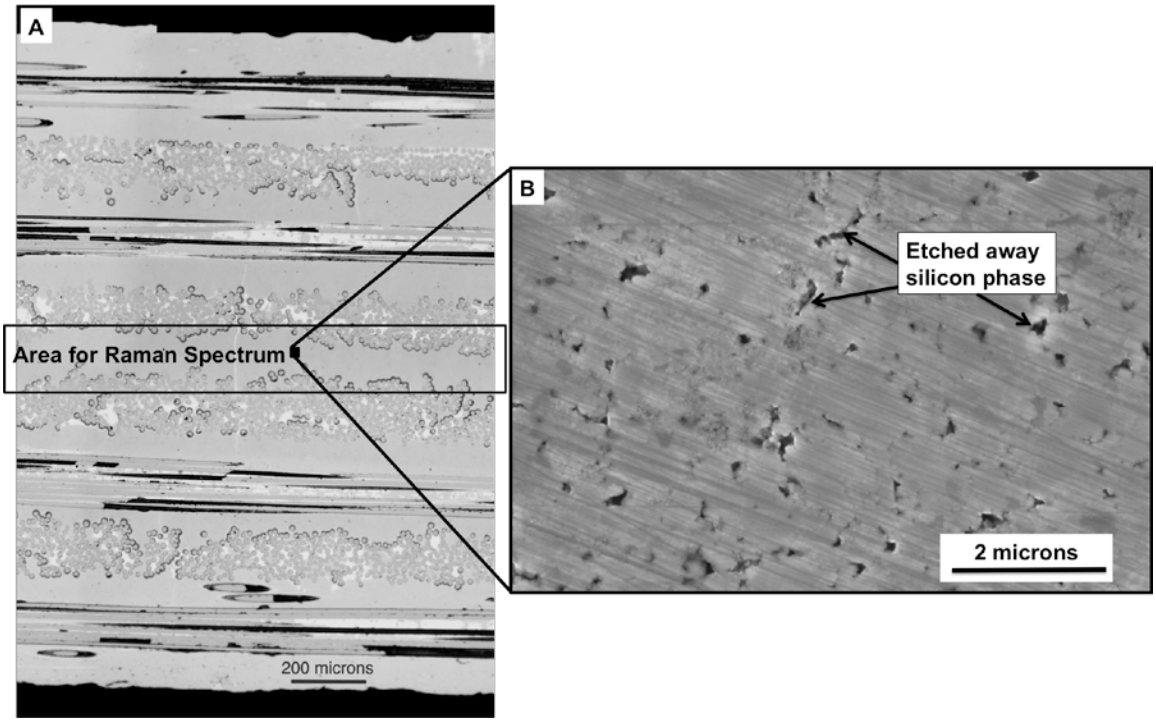

Figure 3.1. Part A shows an optical image of the 8 layer uniaxial composite. The circles are cross-sections of the 90 fiber going in and out of the page. The horizontal lines are fibers in the 0 direction, perpendicular to the 90 fibers. Part B shows secondary electron image of the RBSiC matrix after the silicon has been etched out using KOH.

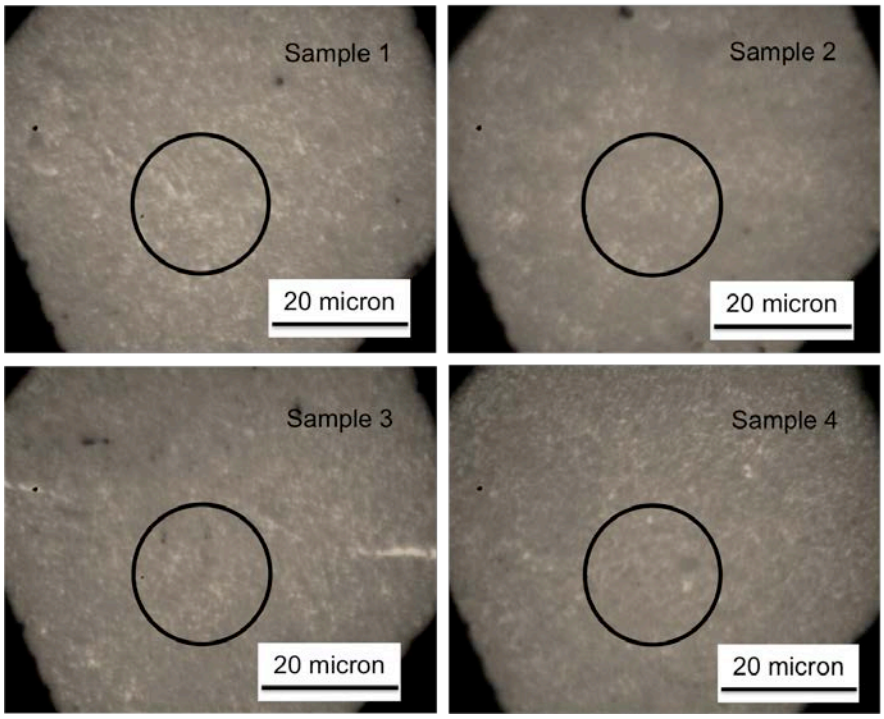

Figure 3.2. Reflected light optical images of 4 different positions in four different samples. The black circles indicate the position of the light source.

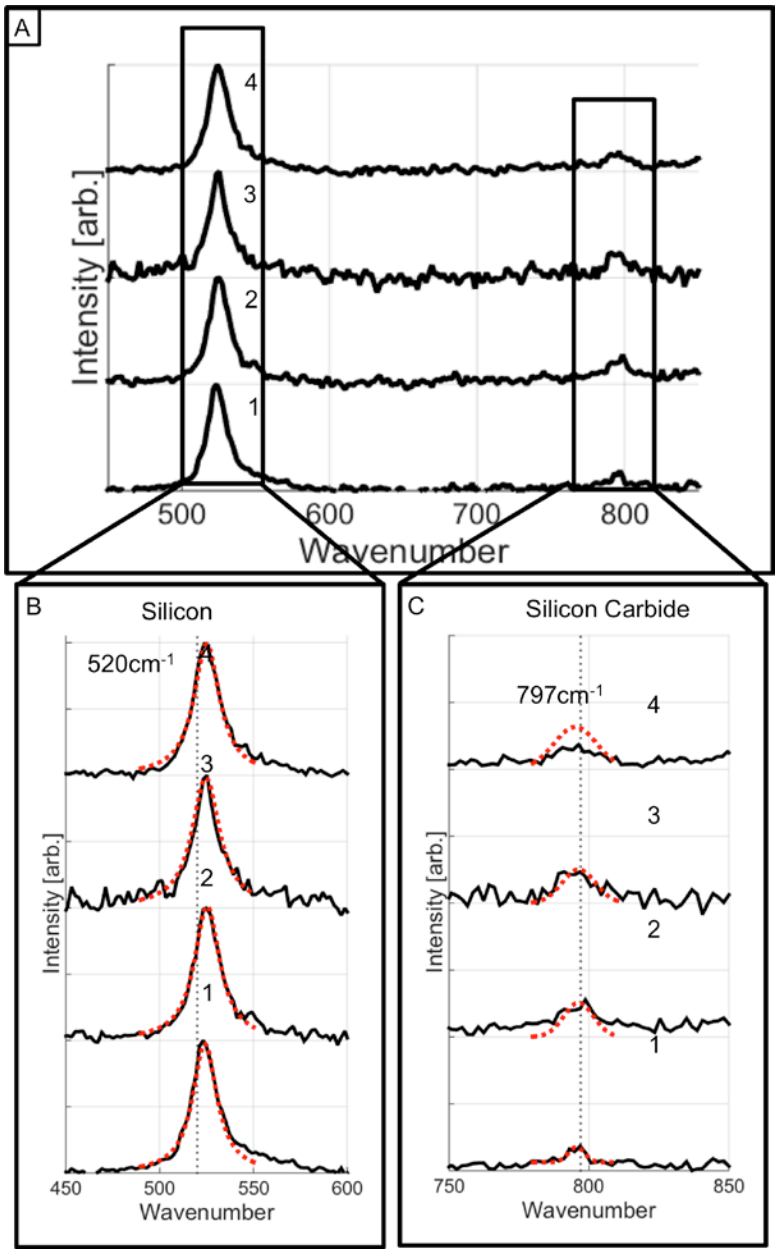

Figure 3.3. In part A, there are the four spectra from the images shown in Figure 3.1. We have shown the silicon peaks for the four images in part B. The black vertical line shows the location for the unstressed silicon at 520 cm^{-1} and the red dotted line shows the fit using the Origin software. In part C, we have the SiC peaks for the four positions. The black vertical line indicates the unstressed TO peak for SiC at 797 cm^{-1} and the red dotted lines indicate the fit using the Origin software.

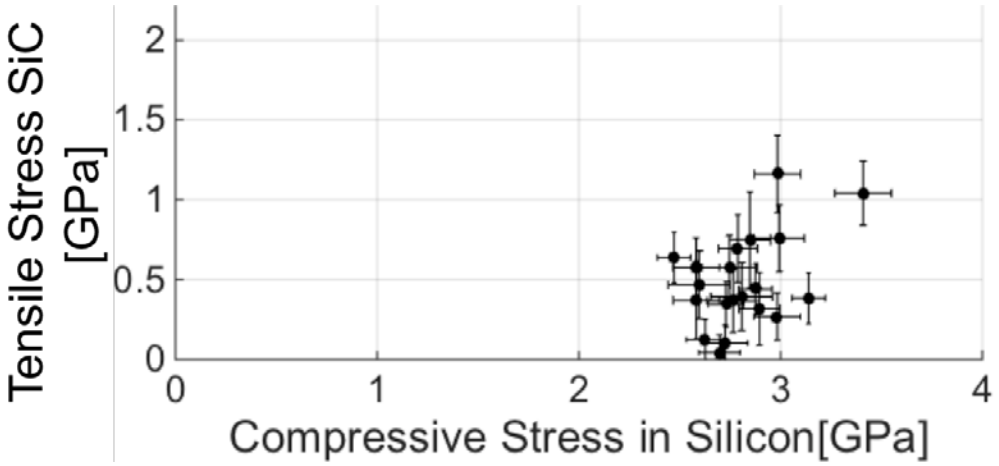

Figure 3.4. Each residual microstress measurement for a single sample with error bars for the uncertainty of each measurement. Each point represents the pair of stresses in the silicon and silicon carbide at that location

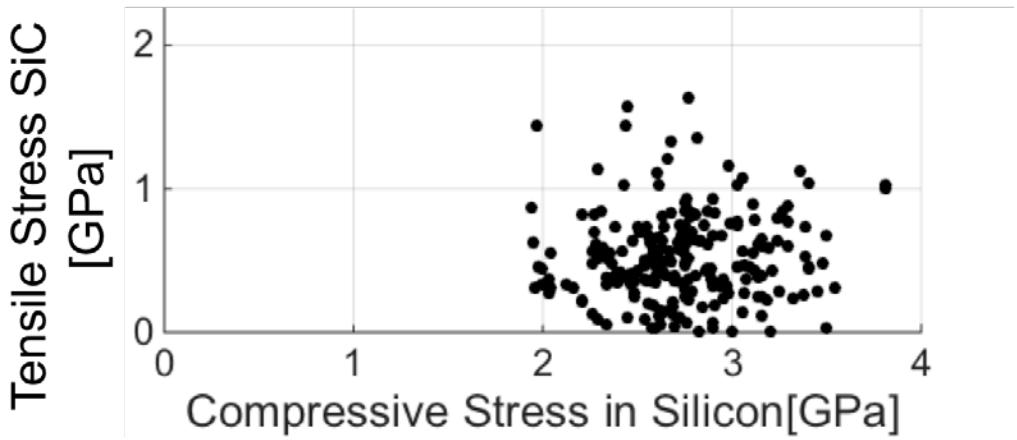

Figure 3.5. Plot of the measured compressive stress in silicon and tensile stress in SiC phases at every position for all samples. Error bars omitted for clarity.

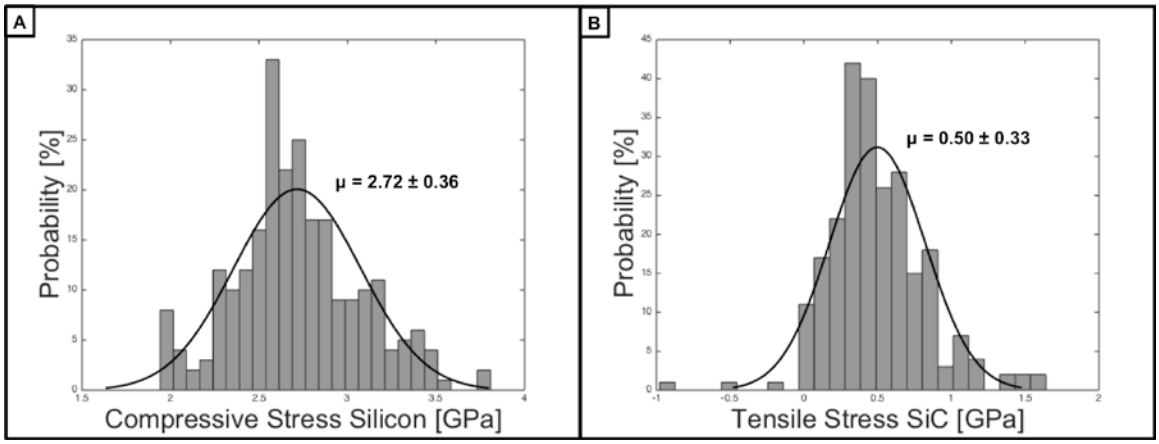

Figure 3.6. Distribution curves for the compressive stress in silicon (left) and the tensile stress in SiC (right).

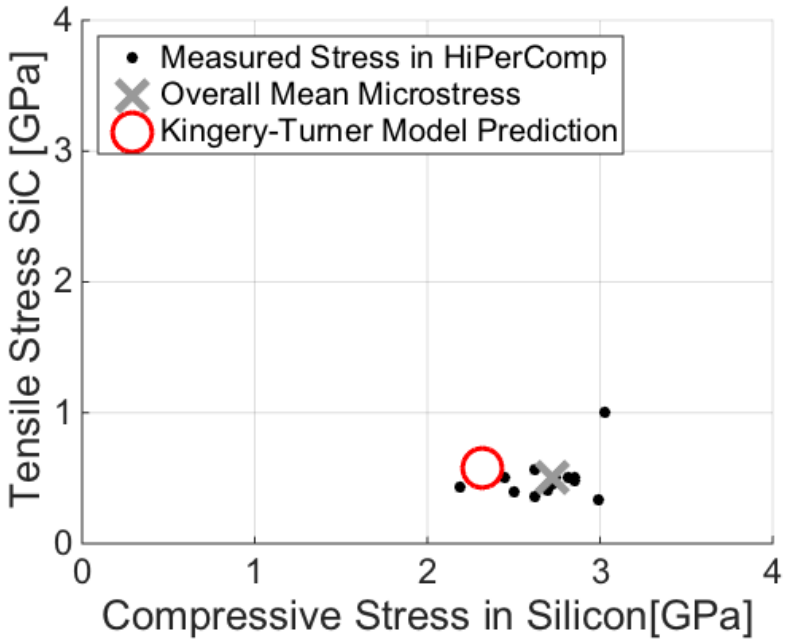

Figure 3.7. Measured microstress values from RBSiC materials using Raman spectroscopy. Black points indicate the average microstress for each sample. The gray "X" indicates the overall mean value for all of the samples. The red circle shows the Kingery-Turner model prediction.

Table 3.I. The peak positions and resulting microstress values for the locations shown in part A of Figure 3.2.

Sample	Silicon Peak Position [cm^{-1}]	SiC Peak Position [cm^{-1}]	Silicon Compressive Microstress [GPa]	SiC Tensile Microstress [GPa]
1	524.02 ± .20	795.54 ± .51	2.39 ± .12	0.41 ± .15
2	525.27 ± .26	796.12 ± .67	3.14 ± .15	0.25 ± .19
3	524.34 ± .28	796.31 ± .49	2.58 ± .17	0.19 ± .14
4	525.03 ± .21	794.32 ± .74	2.99 ± .12	0.75 ± .21

Chapter 4 Relaxation of Residual Microstress in Reaction Bonded Silicon Carbide

4.1 Introduction

Reaction bonded SiC (RBSiC) is a well-established industrial grade of SiC prized for good high temperature properties, and the ease of manufacturing net shape components[1]. RBSiC is fabricated by the reaction of a liquid silicon alloy with carbon, usually in the presence of a pre-reacted silicon carbide filler[2]. The reactive silicon is often introduced by melt infiltration (MI)[3,4]. The reaction does not go to completion[5], leaving unreacted liquid free silicon as a minority phase[6]. Reaction bonding is also used to provide the matrix in reinforced fiber composite[7,8], such as MI-SiC/SiC ceramic matrix composites (CMCs).

In Chapter 2, reported the presence of intense microstresses in monolithic RBSiC. In the silicon carbide phase of commercial grades of RBSiC, we observed tensile microstress in the range of 2-2.3 GPa. Strong compresses microstresses were detected in the free silicon phase, ranging from 1.7-2 GPa in commercial monolithic RBSiC. In Chapter 3, we measured similar stress magnitudes in an RBSiC matrix of a ceramic matrix composite (CMC). The matrix SiC phase in MI-SiC-SiC CMC showed tensile microstresses of 0.1-1.7 GPa. In the free silicon phase of the MI-SiC-SiC CMC matrix, the compressive microstresses were in the range 2-3.8 GPa.

We suggested that the freezing of the liquid free silicon during cooling caused the compressive microstresses in the silicon and tensile microstresses in the SiC. Liquid silicon, expands during crystallization. If unrelaxed, the free silicon crystallization expansion strain (CES), constrained by a rigid network of silicon carbide, causes the silicon to be in a state of

compression while the SiC is in a state of tension. As the crystallization expansion strain from silicon freezing is dilational, we believe that the microstresses can only by relaxed by dilational creep in the constraining SiC phase since the silicon is in incompressible and in compression. The solid silicon is much softer than the SiC, but conventional plasticity of the silicon phase, by dislocation motion, conserves volume and cannot relax a dilational strain.

We will therefore examine how the stress in the silicon and SiC phases relaxes in the as-manufactured RBSiC. The microstresses that we measured the in as-manufactured materials must have had some relaxation during the previous processing, but the details of the thermal history are not available to us. In this chapter, we examine how the residual stress state in the silicon and SiC phases changes during subsequent heat treatment.

4.2 Methods

4.2.1 Material

We examined two types of reaction bonded silicon carbide (RBSiC). One was a commercial monolithic RBSiC used in a much earlier creep study by Wiederhorn et al[9] and in Chapter 2. This was grade KX01, with 42 vol% free silicon and a SiC grain size ranging from 1.9-4.8 microns and the free silicon phase having a characteristic size between 0.6-4.6 microns. Details of the microstructure are in Chapter 2. Four samples of the monolithic RBSiC grade were used for this experiment.

The other RBSiC is the matrix of a commercial MI-SiC/SiC ceramic matrix composite (CMC), commonly known as HiPerComp™, manufactured by GE Aviation. The CMC is a continuous fiber reinforce composite produced by melt infiltration (MI)[10].The composite matrix consists of ~20 ± 5 vol% unreacted free silicon determined by quantitative XRD in Chapter 3. The average SiC grain size is on the order of 1 micron, and the interpenetrating silicon veins on

the order of a few hundred nm. Twenty-two samples of the composite matrix have been analyzed in this chapter.

4.2.2 Microstress Measurement

Raman spectroscopy is a known technique to measure the residual stress in the silicon[11–13] and SiC[14–16]. The Raman system being used is the same custom system used in previous studies and described in detail in Chapter 2 and Chapter 3. Briefly, we use a 532 nm green laser for excitation. The laser is focused with a 20 micron spot size on the sample with a Nikon Eclipse ME600L. The excitation spectra is separated with the HoloSpec VPT spectrograph, and converted to a computer signal through the Newton EM CCD. This system uses a two standard calibration method. First, the spectrograph is calibrated using a NIST calibrated argon light emission spectrum. The laser is then calibrated using powder acetaminophen.

For a Raman active material, there is a characteristic wavenumber associated with a room temperature, unstressed material. This characteristic wavenumber shifts linearly when a stress is applied to the material[17]. The relationship is such that

$$\Delta\omega = R\sigma \qquad [1]$$

where $\Delta\omega$ is the shift in wavenumber, σ is the applied stress, and R is the Raman coefficient determined experimentally.

We have identified a Raman peak for each of the two phases represented in RBSiC. For the silicon phase, we used the $q \approx 0$ phonon peak with a characteristic peak position at $520cm^{-1}$. The Raman coefficient for silicon was determined by Anastakakis to be $1.88 \pm 05\ cm^{-1}/GPa$[18]. For polycrystalline SiC, we chose the transverse optic phonon which has a triplet peak at $797cm^{-1}$. This peak is representative of both the α and β-SiC present in the RBSiC materials[19]. To

determine the stress in the SiC phase, we will be using 3.53 ± 0.21 cm^{-1}/GPa as determined by DiGregorio[20].

Each sample was examined as-manufactured. All samples were polished to a 1 micron finish with a non-aqueous solution. Twenty Raman microstress measurements were taken from each sample prior to annealing. After initial microstress measurements, each sample was then annealed, followed by a second round of polishing to a 1 micron finish. Finally, the relaxed residual microstress was measured using Raman spectroscopy.

4.2.3 Annealing

The as-manufactured specimens (CMC panels and RBSiC billets) had some relaxation during their manufacturing, mostly likely during the cooling stage of the manufacturing thermal cycle. We have no information about this. Therefore, we compare as-manufactured microstress states with samples that have had an additional anneal to determine how the RBSiC relaxes.

After the initial residual microstress was measured, each of the samples was annealed. All samples were annealed in lab air using a box furnace with $MoSi_2$ heating elements. For samples that were annealed for 5 hours or longer, the samples were placed in the furnace at room temperature and allowed the heat up and cool down with the furnace. For samples annealed under 5 hours, the heat up and cool down time would have affected the relaxation time. Therefore, the furnace was allowed to heat to temperature before the sample was placed into the furnace. After the specified time, the sample was removed from the hot furnace and quickly cooled to room temperature in air.

4.3 Results

4.3.1 Microstress of As-Manufactured Material

In Table 4.I we have shown the mean value and standard deviation of the microstress in the silicon phase and the SiC phase of the as-manufactured monolithic RBSiC and composite matrix. For the monolithic RBSiC, this is the result of 80 measurements across 4 different samples. The monolith ranged from 1.7 – 2.0 GPa in compression in the silicon phase and from 2.2 – 2.4 GPa tension in the SiC phase. For the composite matrix, Table 4.I shows the average of 440 measurements in 22 different samples. The CMC material showed a larger range stress measurements with the compressive stress in silicon ranging from 2 – 3.8 GPa and the tensile stress in the SiC phase of the matrix material ranging from 0.1 – 1.7 GPa. The microstress values indicated by the Raman shifts were quite variable differing from one location to another in each sample. The variation in the microstress could be fit to a normal distribution. The mean values for the monolithic RBSiC and composite matrix are given in Table 4.I with the standard deviations.

Two types of analyses were done on the annealed samples. In the first type, we examined the effect of time while maintaining a constant annealing temperature. Both the monolithic RBSiC and composite matrix were examined with the constant temperature annealing. In the second type of testing, the time was kept constant while the temperature itself was varied. Only the composite matrix was examined in the second type of experiment where temperature was the variable.

4.3.2 Relaxation of Residual Microstress as a Function of Time

An annealing temperature of 1200°C was used to determine the time dependence for relaxation of the microstress. The composite matrix was examined at nine different times: 0.5, 1,

1.5, 5, 10, 15, 20, 40, and 80 hours. For the monolithic RBSiC, three times were examined: 0.5, 1.5, 2 hours. Samples annealed for 5 hours or more were placed in a cold furnace and ramped to temperature at 10°C/min. Samples are not expected to relax under 1000°C, meaning that relaxation during heat up is less than 20 minutes. This constitutes a small portion of time compared to the annealing time. Samples annealed under 5 hours were placed into the furnace at temperature, removed after the specified time, and allowed to cool to room temperature quickly. The different cooling rates did not seem to affect the residual microstress measurements.

After being annealed at 1200°C, the samples were re-polished, and imaged using Raman spectroscopy to measure the relaxed residual microstress in the silicon and SiC phases of the monolithic RBSiC in the composite matrix. The microstess in the monolithic RBSiC after the 1200°C anneal. Figure 4.2 and Figure 4.3 show the microstess in the SiC phase after annealing.

For the monolithic material, we see a 75% reduction in the compressive stress measured in the silicon phase in the first 30 minutes at 1200°C. After the initial reduction in microstress, there does not appear to be any further reduction in the compressive microstress in the sample that was annealed 90 minutes longer.

In the tensile microstress of the SiC phase, we see an immediate relaxation in the first 30 minutes. This is similar to what we examined in the silicon phase for the monolithic material. Again, the relaxation occurs quickly (within 30 minutes) and we examine no further relaxation in the samples that have been annealed for longer periods of time.

In the composite matrix, the measured microstress the silicon phases relaxes quickly, but not as quickly as the silicon phase in the monolithic RBSiC (Figure 4.2). For convenience, we have re-plotted the first 5 hours of data in Figure 4.3. In this new plot, we see that the residual microstress relaxes by almost 50% from the mean value in just 5 hours. After the initial

relaxation in 5 hours, there is only a very slight decrease (8% from the original stress) in the next 75 hours and the stress does not relax to zero in the time frame examined. It is worth noting the relaxation examined in the first 5 hours is more than twice that of the variation shown in the as-manufactured samples.

In the SiC phase of the composite matrix, we see variation in the tensile microstress measurements of the same magnitude examine in the as-manufactured samples. It becomes difficult to assess whether the tensile microstress in the CMC has in fact relaxed, since the variation is consistent with the variation in the as-manufactured samples.

When comparing the monolithic RBSiC to the composite matrix, we notice that the stress measured in the SiC phase for the monolithic RBSiC has a higher magnitude than the magnitude of the microstress measured in the silicon phase of the monolithic RBSiC at every point. Conversely, the magnitude of the stress measured in the silicon phase of the composite matrix is higher at every point than the magnitude measured in the SiC phase.

4.3.3 Relaxation of Residual Microstress as a Function of Temperature

We examined the temperature dependence of the relaxation in the composite matrix material. Since the time dependent experiments showed such rapid relaxation, we chose 60 minutes as the constant time for the different temperature exposures. Two different samples were annealed under the same conditions at each temperature. The mean values for the silicon phase of the composite matrix are given in Table 4.II. Again, the variation in the SiC phase was similar in the as-manufactured and the post-anneal. For this reason, the SiC phase of the composite matrix was omitted.

As has been shown with the composite matrix, there was large variation in the measured microstress of the as-manufactured material. It is convenient then, to plot the data as the amount

of relaxation that occurs during annealing. We have included the calculated relaxation, that is the difference between the measured microstress as-manufactured and the measured microstress after the one-hour anneal. In Figure 4.4, we have plotted the amount of relaxation inferred at each temperature.

The amount of relaxation at each temperature in the silicon phase shows a peak in the neighborhood of 1275°C. As the temperature increases past 1275°C, there is less relaxation taking place. There is nearly no relaxation observed at 1150°C and 1350°C.

4.4 Discussion

4.4.1 As-Manufactured

The microstress measured in the composite matrix has much more variation than the monolithic material. It was suggested in a previous study that the increase in variation in the composite matrix was due to the increase in the complexity of the boundary conditions on the silicon expansion. In any case, the increased variation of the composite matrix makes determining the relaxation in the SiC phase of the CMC `impossible. Instead, we will focus on the relaxation examined in the silicon phase of both materials and the SiC phase of the monolithic material.

4.4.2 Time Dependence of Relaxation

We presume that the mechanism for relaxation of the microstresses is creep. Since silicon incompressible and in compression, the interconnected SiC phase that constrains the silicon must be expanding by dilational creep to allow for the stress to relax in both phases. The time dependence of the relaxation indicates that the relaxation rate is larger at short times (when the microstress is high), but much slower at long times (when the microstress is lower). This is not

consistent with Newtonian creep, with a stress exponent of one, since the microstress must continuously relax with an exponential decay. But fast early relaxation followed by slow later relaxation could be consistent with a non-Newtonian creep with a large stress exponent. A large stress exponent would lead to fast creep (and fast stress relaxation) in the early stage when the remaining stress is high, followed by much slower creep (and relaxation) as the remaining stress diminishes.

Wiederhorn et al. showed that tensile creep in RBSiC can be described with a creep law with a large stress exponent[9]. We will concern ourselves with the tensile creep since the SiC phase in our composite is in tension. One of the materials used Wiederhorn's study was the monolithic RBSiC we used here (kindly supplied by S. Wiederhorn) so we can directly compare our microstress relaxation behavior to tensile creep.

Wiederhorn et al. was able to determine the strain rate of two RBSiC materials with different volume fractions of unreacted free silicon at 1300°C. Typically, for power law creep, the creep rate is expressed as:

$$\dot{\varepsilon} = A\left(\frac{\sigma}{\sigma_R}\right)^n \qquad [2]$$

where $\dot{\varepsilon}$ is the strain rate, A is the kinetic constant, σ is the applied stress, σ_R is the normalizing factor, and n is the stress exponent. The Wiederhorn data for tensile creep of this grade of RBSiC could be fit to this expression with a stress exponent of 10.6. We now must convert from a creep law for strain rate vs. stress to a stress relaxation expression, in terms of stress vs. time.

In order to compare the results from the Weiderhorn experiments to that of this study, we will use the simplification that $\dot{\sigma} = E\dot{\varepsilon}$. With this, we can relate the stress relaxation measured in this experiment with the creep rates measured in the Wiederhorn experiment. Briefly:

$$\dot{\sigma_{SiC}} = \frac{\partial\sigma}{\partial t} = -E_{SiC}A\left(\frac{\sigma}{\sigma_R}\right)^n \qquad [3]$$

$$(\partial\sigma)(\sigma^{-n}) = \frac{E_{SiC}A}{\sigma_R^n}\partial t \qquad [4]$$

After integrating the partial derivatives, we define the stress as a function of time:

$$\sigma(t) = \left[\sigma_o^{1-n} - \frac{E_{SiC}A(1-n)t}{\sigma_R^n}\right]^{\frac{1}{1-n}} \qquad [5]$$

where σ_o is the initial stress exerted on the phase; in our case, this is the residual microstress measured in the as-manufactured material.

We found it useful to display the stresses in a normalized fashion for both the silicon and SiC phases. For this reason, the stresses displayed are normalized by the microstress in the sample annealed for the longest amount of time. The monolithic RBSiC is normalized by the 2 hour anneal, σ_{Si} = 0.44 GPa and σ_{SiC} = 1.63 GPa. For the CMC, the measured microstress values were normalized by the microstress measured in the 80 hour anneal, where σ_{Si} = 1.16 GPa, and σ_{SiC} = 0.49.

We are able to use the expression in Eq. [5] to fit the normalized microstress measurements associated with Figure 4.1-4.3. The n and A values determined for the monolithic RBSiC and the composite matrix can be found in Table 4.III. Note that the stress exponent, n, captures the hockey stick shape of the curve, where the kinetic constant, A, indicates the microstress of the plateau. Since the microstresses shown in Figure 4.5 and Figure 4.6 are normalized, the A values is simply a fitting parameter. We have also plotted the relaxed microstress measurements with the fits found using Eq. [5] in Figure 4.5 and Figure 4.6.

Since the monolithic RBSiC used in this study was the same material used in Wiederhorn's creep study, we kept the stress exponent the same, and used the kinetic constant as a fitting parameter. As can be seen in Figure 4.5, keeping the same stress exponent captures the fast relaxation examined in the monolithic RBSiC.

In the composite matrix, we were able to fit the data to Eq. [5] with a stress exponent of 10.4. This is similar to the stress exponent found in the monolithic RBSiC, implying a similar mechanism for creep. The kinetic constant found for the composite matrix is slightly lower than the kinetic constant for the monolithic RBSiC. The temperature for relaxation of the monolithic RBSiC was performed at the same temperature as the composite matrix in this study allowing comparison even with the normailization. We see that at the same temperature, the monolithic RBSiC has a slightly faster kinetic constant than the composite matrix, suggesting a faster creep rate in the monolith.

The monolithic RBSiC material has a much larger grain size, suggesting that the monolith would resist creep better than the smaller grain size CMC. We examine that the stress in the monolithic RBSiC relaxes out much faster than the stress in the CMC. Therefore we know that grain size alone is not the determining factor for stress relaxation in RBSiC.

What is more likely the determining factor for the relaxation rate is the silicon content. In both the monolithic RBSiC and composite matrix, the silicon phase is surrounding the SiC grains. Silicon has a much lower melting temperature (1410°C) than SiC (2700-3000°C). In the monolithic RBSiC, the silicon content is twice that of the CMC material. Having an excess of the silicon phase, which is nearer to its melting temperature, during the anneals, will have a strong affect on the relaxation rates of the material. It is reasonable then that the amount of free silicon phase in the RBSiC material is the rate controlling mechanism for this system.

4.4.3 Temperature Dependence of Relaxation

We see that the reduction in residual stress increases up to 1275°C where there is a peak. Increasing the temperature beyond 1275°C provides less reduction in the microstress, and nearly

no change at 1350°C. This is somewhat troubling since all mechanisms for relaxation would suggest that an increase in temperature would cause an increase in relaxation.

We used Differential Scanning Calorimetry to identify a thermal event in composite matrix. The test was done on a 30.7 mg sample of the composite matrix. The sample was then taken to 1450°C at 20°C/min with the energy reported every 5 degrees.

The DSC scan does not show an energetic occurrence at 1275°C as we would have expected. The onset of melting occurs at 1381°C and is complete by 1400°C. The onset of solidification occurs at 1373°C and is complete at 1350C. There is no thermal event in the 1275-1350°C temperature range that could be associated with decrease in relaxation.

4.5 Conclusion

We have examined the relaxation of the compressive microstresses in silicon phase and tensile microstresses in the SiC phase of reaction bonded SiC in a monolithic RBSiC material and in a composite matrix for a CMC. The compressive stress in the silicon phase for the monolithic RBSiC decreases from 1.8 GPa to 0.4 GPa in 30 minutes at 1200°C, and tensile stress in the SiC phase of the monolithic RBSiC decreases from 2.3 GPa to 1.5 GPa in 30 minutes at 1200°C. There was very little subsequent reduction in the measured microstress. In the composite matrix, the compressive stress in the silicon phase decreases from 2.7GPa to 1.4 GPa in 5 hours at 1200°C, and with only a small decrease in residual microstress for anneals longer than 5 hours.

Both the monolithic RBSiC and the composite matrix show fast relaxation at short times, followed by much slower relaxation at long times. This behavior is consistent with stress relaxation by power law creep with a large stress exponent. Using the creep exponent reported by Weiderhorn for tensile creep of monolithic RBSiC, we could approximately describe the

behavior. It was found that the stress exponent exhibited by the monolithic RBSiC was in agreement with the previous creep experiment performed on the same material. The stress exponent for the composite matrix was very similar to that of the monolithic RBSiC. We found that the composite matrix had a lower kinetic constant than the monolithic RBSiC annealed at the same temperature. This shows us that silicon content influences the relaxation rate much more than grain size.

We also found that there was a maximum amount of relaxation that occurred at 1275°C. It is surprising that increasing the annealing temperature past 1275°C exhibits a reduction in the amount of relaxation in the composite. This does not correspond to a thermal event as indicated by DSC.

Acknowledgements

The authors would like to thank Alan Olvera for his assistance in the DSC measurement.

References

1. Sawyer GR, Page TF. Microstructural Characterization of “REFEL” (Reaction-Bonded) Silicon Carbides. *J Mater Sci*. 1978;13:885-904.

2. Martinez Fernandez J, Munoz A, de Arellano Lopez AR, Valera Feria FM, Dominguez-Rodriguez A, Singh M. Microstructure-Mechanical Properties Correlation in Siliconized Silicon Carbide Ceramics. *Acta Mater*. 2003;51:3259-3275.

3. Margiotta JC. Study of Silicon Carbode Formation by Liquid Silicon Infitration of Porous Carbon Structures. 2009.

4. Luthra K, Singh R, Brun MK. Toughened Silcomp Composites - Process and Preliminary Properties. *Am Ceram Soc Bull*. 1993;72:79.

5. Singh M, Behrendt DR. Studies on the Reactive Melt Infilitration of Silicon and Silicon-

Molybdenum Alloys in Porous Carbon. *Annu Meet Am Ceram Soc*. 1992;(94).

6. Hillig WB. Melt Infiltration Process for Making Ceramic Matrix Composites. In: Mazdiyasni KS, ed. *Fiber Reinforced Ceramic Composites*. Park Ridge, NJ: Noyes Publications; 1990:261-277.

7. Bhatt RT, Gyekenyesi JZ, Hurst JB. *Silicon Effects on Properties of Melt Infiltrated SiC/SiC Composites*. NASA Glenn; 2000.

8. Nimmer R, Corman G, Gilmore R. *Laminate Orientation and Bias Effects on Prepreg HiPerComp CMC Mechanical Properties*. GE Global Research; 2009.

9. Wiederhorn SM, Hockey BJ, French JD. Mechanisms of Deformation of Silicon Nitride and Silicon Carbide at High Temperatures. *J Eur Ceram Soc*. 1999;19:2273-2284. http://www.ewp.rpi.edu/hartford/users/papers/engr/ernesto/barthc2/EP/Other/References/[23].pdf . Accessed 1999.

10. Corman GS, Luthra KL. Silicon Melt Infiltrated Ceramic Composites (HiPerComp). In: *Handbook of Ceramic Composties*. New York: Springer; 2005.

11. Hart TR, Aggarwal RL, Lax B. Temperature dependence of Raman scattering in silicon. *Phys Rev B*. 1970;1(2):638-642. doi:10.1103/PhysRevB.1.638.

12. Cerdeia F, Cardona M. Effect of Carrier Concentration of Raman Frequencies of Si and Ge. *Phys Rev B*. 1972;5:1440-1454.

13. Huang X, Wu K, Chen M, et al. Temperature Dependence of Raman Scattering in Si Crystalls with Heavy B and/or Ge Doping. *Mater Sci Semicond Process*. 2006;9:257-260.

14. Li Z, Bradt RC. Micromechanical Stresses in SiC-Reinforced Al2O3 Composites. *J Am Ceram Soc*. 1989;72:70-77.

15. Xiao Z, Yang Y, Jin N, Liu S, Luo X, Huang B. Microstructure and Thermal Residual

Stress Analysis of SiC Fiber through Raman Spectroscopy. *J Raman Spectrosc*. 2013. doi:10.1002/jrs.4356.

16. Olego D, Cardona M, Vogl P. Pressure Dependence of the Optical Phonons and Transverse Effective Charge in 3C-SiC. *Phys Rev B.* 1982;25:3878-3888.

17. Anastassakis E, Pinczuk A, Burstein E. Effect of Static Uniaxial Stress on the Raman Spectrum of Silicon. *Solid State Commun*. 1970;8:133-138.

18. Anastassakis E, Cantarero A, Cardona M. Piezo-Raman measurements and anharmonic parameters in silicon and diamond. *Phys Rev B.* 1990;41:7529-7535.

19. DiGregorio JF, Furtak TE. Analysis of Residual Stress in 6H-SiC Paricles within Al2O3/SiC Composites through Raman Spectroscopy. *J Am Ceram Soc*. 1992;75:1854-1857.

20. DiGregorio JF, Furtak TE, Petrovic JJ. A Technique for Measuring Residual Stress in SiC Whiskers within an Alumina Matrix through Raman Spectroscopy. *J Appl Phys*. 1992;71:3524-3531.

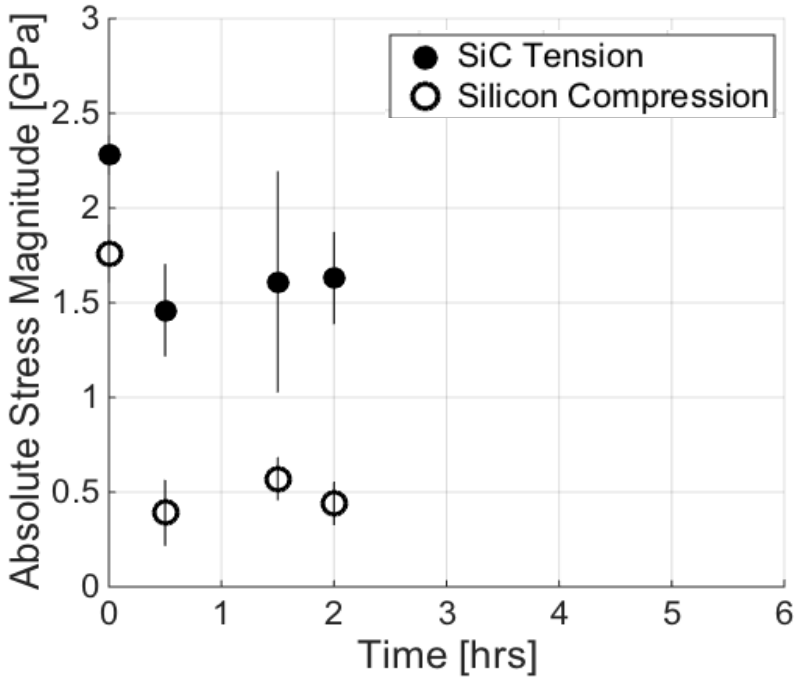

Figure 4.1. The stresses displayed in this graph have been normalized by the stress measured after 2 hours of annealing in the monolithic RBSiC after being annealed at 1200°C. Compressive microstresses in the silicon phase are displayed with open circles, and tensile microstress in the SiC phase are displayed with filled dots.

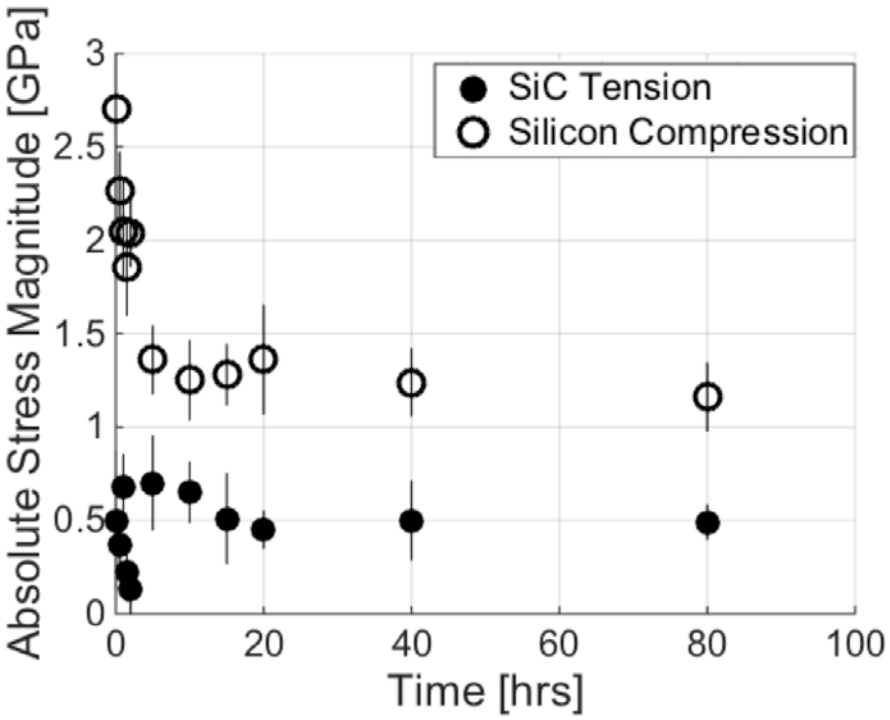

Figure 4.2. Measured compressive microstresses in the silicon phase (open circles) and tensile microstress in the SiC phase (filled dots) of the composite matrix after being annealed at 1200°C for the specified amount of time.

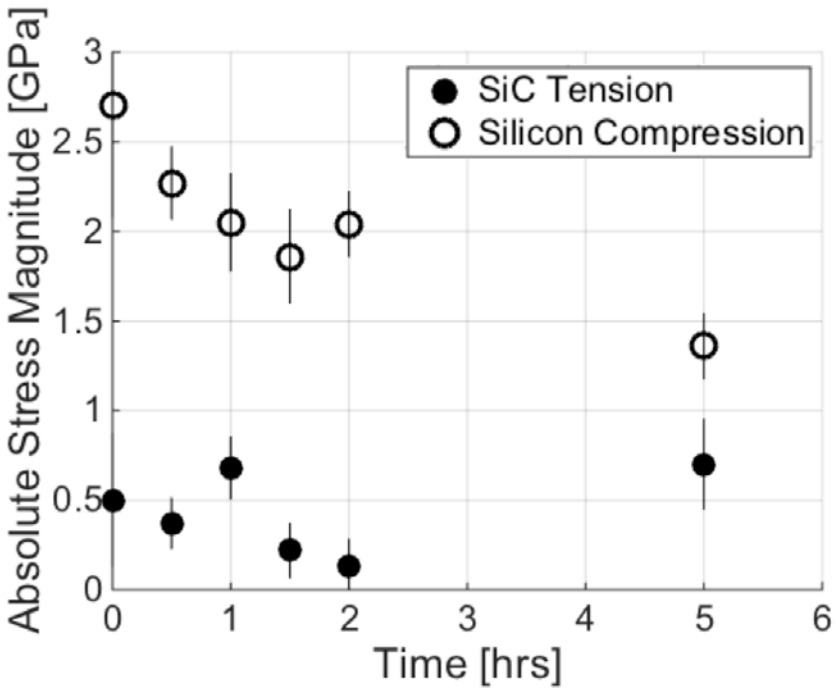

Figure 4.3. Zoomed in portion of Figure 4.2. This plot shows the measured stress in the composite material after just the first 5 hours of annealing.

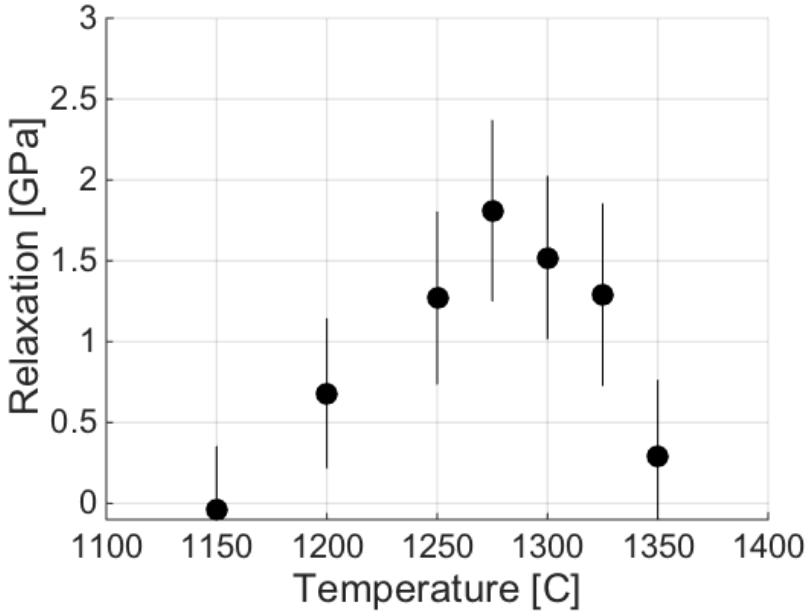

Figure 4.4. Plotted is the amount of relaxation in the silicon phase of the CMC examined at each temperature in a 60 minute anneal.

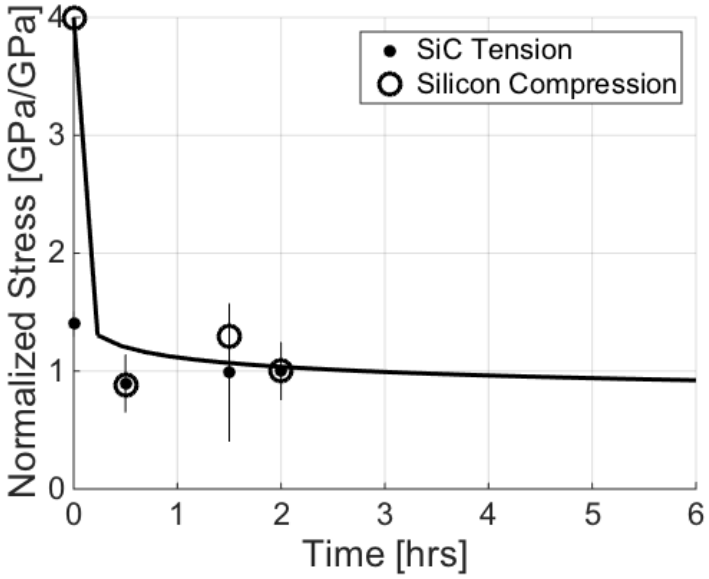

Figure 4.5. Fitting a creep curve to the normalized microstress measurements in silicon and SIC phases of the monolithic RBSiC during the constant temperature experiment. The line is Eq [5] fit to the data set with n = 10.6 and A = 1.0E-18.

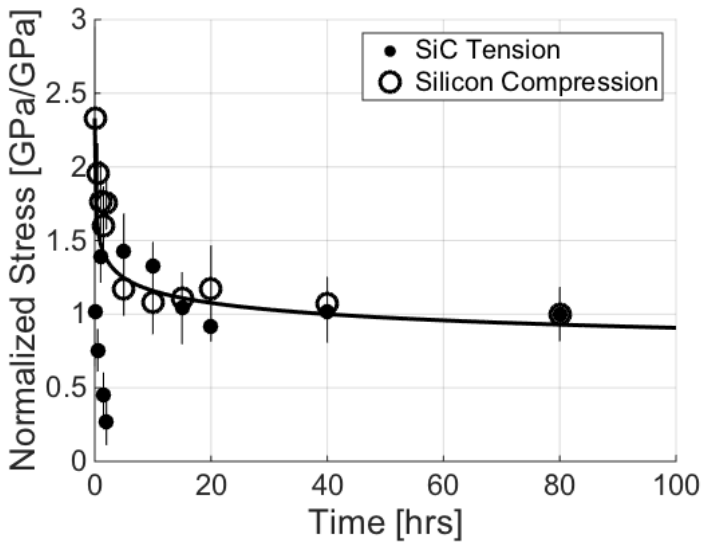

Figure 4.6. Fitting a creep curve to the normalized microstress measurements in silicon and SIC phases of the composite matrix during the constant temperature experiment. The line is Eq [5] fit to the data set with n = 10.4 and A = 7.0E-20.

Table 4.I. Mean as-manufacture values for the monolithic RBSiC and the composite matrix

Material	Compressive stress in Silicon Phase [GPa]	Tensile stress in SiC Phase [GPa]
Monolithic RBSiC	1.76 ± 0.15	2.28 ± 0.10
Composite Matrix	2.70 ± 0.36	0.50 ± 0.33

Table 4.II. Results of the measured microstress in the composite matrix as a function of temperature

Temperature [°C]	Mean Compressive Stress As-Manufactured [GPa]	Mean Compressive Stress after 1 hour Anneal [GPa]	Relation [GPa]
1150	2.25 ± 0.21	2.29 ± 0.18	-0.04 ± 0.39
1200	2.15 ± 0.37	1.47 ± 0.23	0.68 ± 0.46
1250	2.86 ± 0.30	1.59 ± 0.23	1.27 ± 0.53
1275	2.74 ± 0.24	0.93 ± 0.28	1.81 ± 0.56
1300	2.45 ± 0.26	0.93 ± 0.23	1.52 ± 0.50
1325	2.59 ± 0.27	1.30 ± 0.28	1.29 ± 0.56
1350	2.66 ± 0.26	2.37 ± 0.22	0.29 ± 0.47

Table 4.III. Values for n and A determined from Wiederhorn et al[9].

Material	Temperature [C]	n	A
KX01 (Wiederhorn paper)	1300	10.6	2.2E-8
KX01 (monolith in this chapter)	1200	10.6	1.0E-18
HiPerComp™ (composite matrix in this chapter)	1200	10.4	7.0E-20

Chapter 5 Ply-Level Residual Stress in Mel-Infiltrated SiC/SiC Ceramic Matrix Composites from Crystallization Expansion Strain

5.1 Introduction

It is recognized that SiC/SiC ceramic matrix composites contain residual stresses[1], which influence the mechanical properties of the composite[2]. Dunn witnessed this affect while loading the composite in 4-point bending [3]. In his experiment, he noticed that many cracks were visible in the composite while under load. When the load was removed, the cracks in the matrix closed up. This is indicative of a compressive residual stress in the matrix of the composite. Similarly, Morscher et al. inferred the role of residual stress of the composite using hysteresis loops[4]. He found that upon unloading, some of the overall strain was recovered, indicating that there was strain reduction caused by a residual compressive stress in the composite material.

Although this phenomenon has been shown in other studies, the magnitude and source of the residual stress have yet to be characterized directly. We have used indentation cracks to measure the ply-level residual stress in a [0/90]2s MI-SiC/SiC CMC in the matrix-rich regions between the fiber containing laminae. In the next sections, we will discuss the source of the residual stress and provide a model for predicting the order of magnitude expected from the ply-level of analysis.

5.2 Indentation Cracks in the Presence of Stress

Indentation testing is a powerful technique to explore a wide range of mechanical phenomena in brittle materials[5]. In the absence of far-field stress, a Vickers indent results in a

diamond indentation with medial/radial cracks forming at the corners of the diamond shape. In a material that experiences far-field stresses, the length of the cracks will be altered based on the direction and magnitude of the far field stress.

The residual stress in the matrix only layers of the laminate composite will be measured using an indentation method developed by Zeng and Rowcliffe[6]. In a stressed material the length of the cracks, which form at the corners of the Vickers diamond, will be altered based on the direction and magnitude of the far field stress. The method developed by Zeng and Rowcliffe uses the length of the stressed crack and the length of an unstressed condition to determine the magnitude of the residual stress state[7].

The Zeng and Rowcliffe model follows the form:

$$\sigma_{comp} = K_c \frac{1-\left({}^{c_o}/_{c_2}\right)^{3/2}}{\sqrt{\pi c_2}} \qquad [1]$$

where σ_{comp} is the residual compressive stress, K_c is the fracture toughness, c_o is the length of an unstressed crack, and c_2 is the length of the stressed crack. A schematic of this can be seen in Figure 5.1.

The relative magnitude of the crack lengths c_o and c_2 can be treated as an asymmetry parameter, AP = (c_2/c_o). We consider laminates with a residual stress field due to fabrication. In our case, we do not have an unstressed material. Instead of using the crack length found in an unstressed material, we use the crack length that propagates in the y-plane. The composite is a laminate that experiences no delamination. Therefore, it is safe to assume that the stress in the z-plain acting on the crack growing in the y-direction is negligible. Thus, each indent has an unstressed crack (c_o) propagating in the y-direction and a stressed crack (c_2) propagating in the z-direction.

In the schematic, we show all three cases possible. At the top, we show an unstressed case in which the lengths of the horizontal and vertical cracks are the same length (AP = 1). This indicates no residual stress state at the point of the indent. In the second case, we show a compressive force in the horizontal direction, which causes the vertical cracks to be shortened compared to the unstressed, horizontal cracks (AP < 1). In the final case, there is a tensile stress in the horizontal direction, which causes the vertical crack to increase in length compared to the unstressed condition (AP > 1). Again, since there is no delamination, we assume that the stress in the vertical direction is negligible and that the crack growing in the horizontal direction is in an unstressed state.

5.3 Methods and Materials

5.3.1 Materials

The material being examined is a 8-ply [0/90]2s continuous fiber ceramic matrix composite (CMC) designed by GE Aviation, commonly known as HiPerComp™. The composite consists of SiC fibers with a boron nitride coating within a melt-infiltrated (MI) reaction bonded silicon carbide (RBSiC) matrix described by Corman and Luthra[8]. The composite consists of 20 vol% unreacted free silicon determined through quantitative XRD[9]. An image of the 8-ply layup for the CMC can be seen in Figure 5.2. This composite shows two 0° fiber directions layers and two 90° fiber directions layers. Between each of the fiber containing layers is a matrix only layer. It was important that the fibers of the fiber containing layers did not impinge on the crack propagation from the Vickers indent. Therefore, indents were done in the matrix only layer at the center of the composite, which was the thickest for all samples. Indents were kept more than 100 microns from the nearest fiber. This would ensure that the cracks from the indent could propagate without being disturbed by the fibers.

In Figure 5.3, we have magnified a region within a 90° fiber layer. In part A, we see the fibers as grey circles, and the BN coating in black surrounding the fibers. In part B, we have magnified the matrix region even further. Here we have etched out the fine grain silicon of the siliconized-SiC matrix. The voided areas in the image represent where the silicon was prior to etching. The etching was done for imaging purposes only, and none of the tests were done on etched samples.

Based on manufacturer specifications, we know that the fiber volume for the composite is on the order of 33 vol%. For the fiber containing layers, we determined that the volume fraction of fibers was 45 vol% and 55 vol% through using ASTM E562-11. This was not taking into account the boron nitride coating. These are relatively thin and are assumed to not play a role in the stress state of the composite.

Fourteen samples of the composite were polished to a 1 micron finish. As was stated, the fiber layers have fibers running perpendicular to one another. At the center of the composite, where the composite is symmetric in layup, there is a thick layer of matrix that proved thick enough to indent without interference from the fibers. Since this layer is the point of symmetry for the fiber layup, both layers above and below will have the same fiber direction. It was unknown if the fiber direction in the fiber layer immediately adjacent to the matrix layer will have an influence on the stress state in the composite. For this reason, eight samples were prepared such that the fibers layers surrounding the center matrix layer were in the 90° direction, and six samples were prepared such that the surrounding fiber layers were in the 0° direction. Since it is assumed that the fibers are constraining the expansion of the matrix, we assume that there will be a measureable stress in both of these cases, i.e. that the stress is biaxial. For each

sample, 20 indents were taken across the length of each sample. The length of the indents and cracks were measured *in situ* and recorded.

5.3.2 Methods

We used a Clark Microhardness Indenter CM-400AT. This machine allows us to control the force of the indent, the duration of the indent, and perform measurements *in situ*. A 500 gram load was used for all indents, which produced an indentation impression of ~20 microns with well-developed radial/medial cracks.

For all indents, the duration of the indent was held constant at 15 seconds. The width of the indent and cracks were measured *in situ*. To ensure that the non-symmetric crack lengths were not a byproduct of a damaged indentation tip, the indenter was rotated 90° and the resulting indents maintained the same asymmetric form. During the course of the experiments, the indenter was calibrated, and no change was seen as a result of the calibration.

5.4 Results

5.4.1 Asymmetry of Indentation Cracks

All of the indents show shortened crack propagation in the z-direction, which is normal to the plane of the laminate. Figure 5.4 is a typical example of an indent in the center matrix layer of the composite. The indent length in the z-direction, c_2, is 62 microns. The indent length in the y-direction, which we take as c_o, is 109 microns. So for this case, the AP is 0.57. With the assumption that there is no stress in the z-direction, we infer that there is a compressive stress in the y-direction. The compression causes the crack to arrest early compared to the non-stressed crack propagating in the y-direction.

Using Eq. [1], we are able to estimate the magnitude of the compressive stress in the matrix only layer of the composite. The fracture toughness value for RBSiC was taken from the literature to 3 MPa$\sqrt{m}$ [10]. For this particular indent, we infer a compressive stress of 215 MPa normal to the y-direction.

5.4.2 Distribution of Asymmetry Parameter

Not all the indents were the same. There was significant variation in the asymmetry parameter of the indents from one indent to another in a single sample. The AP for individual indents appeared to vary randomly, with no noticeable effect of location within a sample. We determined that the variation of the AP follows Weibull statistics. In the top of Figure 5.5, we show a Weibull plot of the AP values obtained for the 120 taken on samples oriented so that the central matrix region was between 0° fibers and the bottom of Figure 5.5 shows the distribution in AP for the 160 data indents between 90° fibers.

For the indents in the matrix between 0° fibers, the mean AP was about 0.73, with the 90^{th} percentile about 0.86 and the 10^{th} percentile around 0.58. For the indents in the matrix between 90° fibers, the mean AP was about 0.86, with the 90^{th} percentile about 0.98 and the 10^{th} percentile around 0.70. The AP for individual indents appeared to vary randomly, with no noticeable effect of location within a sample.

Values of AP equal to 1 indicate when the crack lengths of c_0 and c_2 are equivalent, meaning no stress. Values greater than 1 are when c_0 are less than c_2, which would indicate a tensile stress in the matrix. Nearly all of the AP values are less than 1, indicating that nearly all of the indents show an apparent compressive stress in the matrix region of the composite.

5.4.3 Statistical Distribution of Ply-Level Residual Stress

Using Eq [1], we can use the measured crack lengths to determine the apparent compressive stress in the matrix region, shown in Figure 5.6. As was the case with the AP, the apparent stress calculated from the cracks lengths follows a Weibull distribution. For the indents in the matrix between 0° fibers, the mean apparent stress was about 103 MPa, with the 90^{th} percentile about 155 MPa and the 10^{th} percentile around 40 MPa. For the indents in the matrix between 90° fibers, the mean apparent stress was about 63, with the 90^{th} percentile about 120 MPa and the 10^{th} percentile around 20 MPa. It is interesting that the mean value of the apparent stress is differs depending on the direction of the fibers layers immediately surrounding the matrix rich region that was analyzed. This gives evidence that the stress measured is affected by the immediate landscape.

5.5 Discussion

We have measured the compressive residual stress that exists in the matrix only layer of a laminate CMC. However, what has not been addressed is the cause of the residual stress. The matrix of the CMC consists of melt-infiltrated (MI) reaction bonded silicon carbide (RBSiC). In the MI process, liquid silicon is infiltrated into a carbon rich environment to form SiC, but with some residual silicon remaining. During crystallization, silicon has an 11% volume expansion. This causes the two-phase siliconized-SiC matrix to expand.

As was mentioned before, the composite being examined in this study is a laminate composite with fiber containing layers and matrix only layers. The matrix only layers will want to expansion the full amount of the two-phase siliconized-SiC. However, on either side of the matrix only layers is a layer containing fibers. In the case where the fibers are oriented in the 0° direction, the fibers are stiff, and will act as a constraint on the surrounding matrix. In the case

where the fibers are oriented in the 90° direction, the fibers are not stiff, and instead act as holes to dilute the expansion of the surrounding matrix. In both cases, we expect a compressive stress to form in the matrix only layer, and a tensile stress in the fiber containing layer. Since the fiber is strong when oriented in the 0°direction, we expect to measure a higher stress in the matrix only layers surrounded by 0° fibers than 90° fibers.

5.5.1 Expansion of Siliconized-SiC Matrix

The expansion of the silicon phase during crystallization causes the two phase, siliconized-SiC to expand. In order to determine how much expansion we used the modified thermo-elastic model developed by Kingery and Turner from Chapter 2 and Chapter 3.

Briefly, the original model was developed to determine the stress developed from a coefficient of thermal expansion mismatch. The model follows the form:

$$\sigma_i = (\alpha_r - \alpha_i)\Delta T K_i = \Delta\alpha \Delta T K_i \quad [2]$$

In this equation, σ is the stress, K is the bulk modulus for that phase, α is the coefficient of thermal expansion, and ΔT is the difference between the initial and final temperature. The subscript *i* indicates the phase for which the stress is being calculated, and the subscript *r* describes the coefficient of thermal expansion of the two phase mixture and can be written as:

$$\alpha_r = \frac{\alpha_1 K_1 V_1 + \alpha_2 K_2 V_2}{K_1 V_1 + K_2 V_2} \quad [3]$$

where V is the volume fraction, and the subscripts 1 and 2 represent the two phases being examined.

We know that α_r gives the coefficient of thermal expansion for the two-phase mixture. We also know that αΔT represents a strain value. Therefore, we can represent the strain in the two-phase siliconized-SiC as:

$$\varepsilon_{Si-SiC} = \alpha_r \Delta T = \frac{\alpha_{Si} K_{Si} V_{Si} + \alpha_{SiC} K_{SiC} V_{SiC}}{K_{Si} V_{Si} + K_{SiC} V_{SiC}} \Delta T \quad [4]$$

In the case of crystallization expansion of silicon, the strain from the silicon phase is equivalent to the linear expansion of the silicon phase, i.e., $\alpha_{Si}\Delta T = \varepsilon_{CES}$. The SiC phase is not expanding, meaning that $\alpha_{SiC}\Delta T = \varepsilon_{SiC} = 0$. Therefore, we can rewrite the expansion of the two phase siliconized-SiC as:

$$\varepsilon_{Si-SiC} = \frac{\varepsilon_{CES} K_{Si} V_{Si}}{K_{Si} V_{Si} + K_{SiC} V_{SiC}} \quad [5]$$

The expression defined in Eq. [5], provides a simple expression to define the expansion of the two-phase siliconized-SiC, which in the case of the composite, is the matrix component.

5.5.2 Ply-Level Stress

The stresses estimated from the indentations describe the residual stress has to due with the ply-to-ply interactions of the laminate. As was noted earlier, between each of the fiber containing layers is a matrix only layer. The matrix only layer will have an expansion equal to that determined by Eq. [5]. To determine the expected stress in the fiber containing layers, we will use a thermo-elastic model for laminated composites.

The model being used is from Barnes and Byerly[11]. Similar to the Kingery-Turner model, the Barnes-Byerly model was adopted to determine the thermoelastic stresses that develop in a cross-ply laminate. The model follows the form:

$$\sigma_{22} = \frac{(E_{11} \times E_{22})}{(E_{11} + E_{22})} \times (\alpha_{22} - \alpha_{11}) \Delta T \quad [6]$$

where σ is the stress, E is Young's modulus, and α is the coefficient of thermal expansion. In the case of the original thermo-elastic model, "11" and "22" indicate the direction of the fibers in the laminate.

In the case of the Barnes-Byerly model, the concern is with a cross-ply laminate. In the case of HiPerComp™, we have a third component of the matrix only layers. For this reason, we will break up the analysis into two separate parts, one where the matrix only layer is attached to a fiber layer with 0° fibers and the other where the matrix only layer is attached to a fiber layer with 90° fibers. A schematic of the two analyses can be seen in Figure 5.7.

We will now substitute "11" for the fiber component, and "22" for the matrix component. With this, we can re-write Eq. [6] as:

$$\sigma_m = \frac{(E_{SiC-f} \times E_m)}{(E_{SiC-f} + E_m)} \times \alpha_m \Delta T - \alpha_f \Delta T \qquad [7]$$

Since $\alpha\Delta T$ represents a strain component, we will substitute the thermo-elastic strain from the coefficient of thermal expansion mismatch with the strain developed in the crystallization expansion of silicon:

$$\sigma_m = \frac{(E_{SiC-f} \times E_m)}{(E_{SiC-f} + E_m)} \times \varepsilon_m - \varepsilon_f \qquad [8]$$

The matrix is made up of the siliconized-SiC, and therefore has a strain equal to that determined in the previous section ($\varepsilon_m = \varepsilon_{Si\text{-}SiC}$). The fiber layers are made up of 45 vol% matrix, and 55 vol% fiber. Therefore, the only strain in the fiber layers is that from the 45 vol% which makes up the matrix ($\varepsilon_f = 0.45\varepsilon_{Si\text{-}SiC}$). We can then write the final expression for the ply-level stress in the matrix as:

$$\sigma_m = \frac{(E_{SiC-f} \times E_m)}{(E_{SiC-f} + E_m)} \times 0.55\varepsilon_{Si-SiC} \qquad [9]$$

In order to solve for the stress in Eq. [9], we must first define the modulus values for the matrix layer and fiber layers. For the matrix layer, we will use the rule of mixtures and define $E_m = E_{Si}*f_{Si} + E_{SiC\text{-}m}*f_{SiC}$. In the case of the fiber containing layers, we will define two separate

modulus, one for the 0° fibers, and one for the 90° fibers. This will be done using Voigt and Reuss bounds[12] where:

$$E_f^0 = V_f E_{SiC-f} + V_m E_m \quad [10]$$

and

$$E_f^{90} = \left[\frac{V_{SiC-f}}{E_f} + \frac{V_m}{E_m}\right]^{-1} \quad [11]$$

where E_f^0 is the modulus in the 0° fiber layer, and E_f^{90} is the modulus in the 90° fiber layer. Modulus and volume fraction values can be found in Table 5.I. It is worth noting that upper and lower bounds of the fiber layer modulus determined from Eq. [10] and Eq. [11], are very similar.

Now that all of the variables are set up, we can mathematically solve Eq. [8] for the expected stress in the matrix layer surrounded by 0° fibers and 90° fibers. For the composite examined in this study, the volume fraction of free silicon is 20 ± 5 vol%. The results of the model prediction as well as the mean measured stress can be seen in Table 5.II.

The magnitude of the model prediction is slightly higher than the apparent stress measured from the indentation experiment. The model does not account for any type of relaxation during processing. Since these composites are manufactured at high temperatures, it is reasonable to assume that some type of relaxation has occurred. Therefore, the model presented here is representative of the upper bound of the residual stress state in the ply-level.

The model prediction for the two different fiber orientations is nearly the same. The model does not capture the stress difference measured in the experiment. The Voigt and Reuss limits for the modulus of the fiber layer suggest that there is very little difference between the modulus of a 0° fiber layer and the modulus of a 90° fiber layer.

The Reuss limit for modulus assumes that the fibers in the 90° direction carry some load. In the thesis of Dan Dunn, the modulus of a unidirectional 0° composite and a unidirectional 90°

composite similar to the composite studied here was examined[3]. In Dunn's research, he found that the flexural modulus for a 0° unidirectional composite was around 275 GPa, and the flexural modulus of a 90°was around 105 GPa. Thus, Dunn showed that the modulus of 90° fibers is much less than the modulus in the 0° direction, and that using the Reuss method of determining the modulus of the fiber layer perpendicular to the loading direction is not suitable for this composite.

Since Dunn found that the modulus of the 90° direction fiber layer was so much lower than the 0° fiber layer, we examined the modulus assuming the fibers in the 90° fiber layer acted as holes. Therefore we use Eq. [10] assuming $V_f = 0$. This modification caused the modulus to drop from 377 GPa to 151 GPa, and the subsequent stress in the matrix surrounded by 90° fibers to drop from 249 MPa to 146 MPa.

The newly calculated stress shows that the predicted stress in the matrix surrounded by 90° fibers (σ^{90}) is much less than the expected stress in a matrix layer surrounded by 0° fibers (σ^{0}). We can examine the stress ratio (σ^{90}/σ^{0}) for the calculated stress and the measured stress. We find that the stress ratio for the calculated stress assuming the fibers in the 90° direction act as holes is 0.58, and the measured stress ratio is 0.61. Assuming the fibers in the 90° direction act as holes provides a stress ratio very similar to the measured stress ratio.

5.6 Conclusion

For the first time in the literature, the ply-level residual stress within a CMC has been measured using cracks propagating from Vickers indents. This level of stress has been identified in the past, but has yet to be characterized. The stress measured at the ply-level follows a Weibull distribution. We also found that the stress in the matrix only regions is contingent upon the fiber direction in the surrounding fiber containing layers.

We have identified the cause of the residual stress at the ply-level to be a result of the crystallization expansion of free silicon within the matrix regions of the composite. We modified a thermo-elastic laminate model, used in determining residual stress, to a model that uses the crystallization expansion of the two-phase, siliconized-SiC matrix to determine the ply-level residual stress. We found that the measured residual stress values were somewhat lower than the predicted values using the model. We also found that using the traditional Voigt and Reuss bounds for determining the modulus of the fiber layers did not accurately describe the behavior of this composite. Instead, describing the fibers in the 90° direction as holes provided a stress ratio consistent with the measured stress ratio.

References

1. Steen M. Tensile mastercurve of ceramic matrix composites: significance and implications for modelling. *Mater Sci Eng*. 1998;250(2):241-248.

2. Mei H. Measurement and calculation of thermal residual stress in fiber reinforced ceramic matrix composites. doi:10.1016/j.compscitech.2008.08.015.

3. Dunn D. The Effect of Fiber Volume Fraction in HiPerComp SiC-SiC. 2010.

4. Morscher GN, Ojard G, Miller R, et al. Tensile creep and fatigue of Sylramic-iBN melt-infiltrated SiC matrix composites: Retained properties, damage development, and failure mechanisms. *Compos Sci Technol*. 2008;68(15-16):3305-3313. doi:10.1016/j.compscitech.2008.08.028.

5. Marshall D, Cook R, Padture N, et al. The Compelling Case for INdentation as a Functional Exploratory and Characterization Tool. *J Am Ceram Soc*. 2015;98(9):2671-2780.

6. ZENG K, ROWCLIFFE D. EXPERIMENTAL-MEASUREMENT OF RESIDUAL-STRESS FIELD AROUND A SHARP INDENTATION IN CLASS. doi:10.1111/j.1151-

2916.1994.tb07025.x.

7. Zeng K, Rowcliffe DJ. Vicerks Indentations in Glass -I. Residual Stress Fields and Iso-Stress Contour Maps. *Acta Metall et Mater*. 1995;43:1935-1943.

8. Corman GS, Luthra KL. Silicon Melt Infiltrated Ceramic Composites (HiPerComp). In: *Handbook of Ceramic Composties*. New York: Springer; 2005.

9. Wing B, Halloran J. Microstresses in the Matrix of a Melt-Infiltrated Reaction Bonded Silicon Carbide Ceramic Matrix Composite. 2015.

10. ROUTBORT J, MATZKE H. ON THE CORRELATION BETWEEN SOLID PARTICLE EROSION AND FRACTURE PARAMETERS IN SIC. doi:10.1007/BF01111969.

11. Barnes JA, Byerly GE. The formation of residual stresses in laminated thermoplastic composites. *Compos Sci Technol*. 1994;51(4):479-494.

12. Karch C. Micromechanical Analysis of Thermal Expansion Coefficients. *Model Numer Simulations Mater Sci*. 2015:104-118.

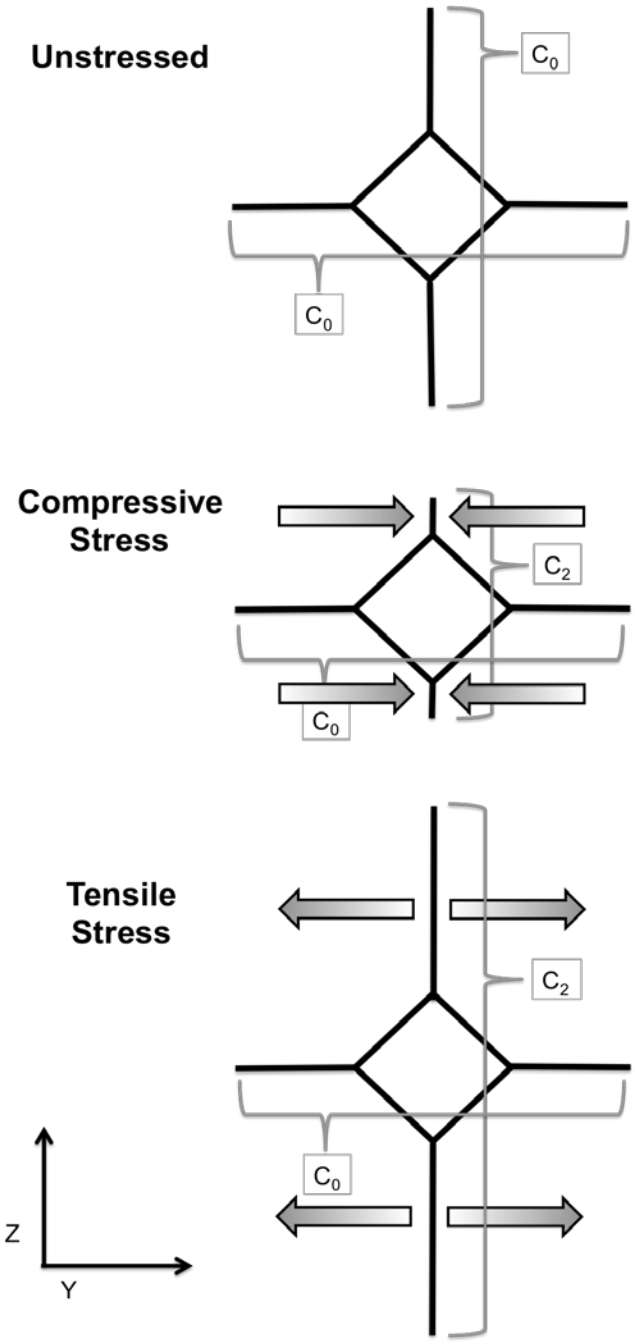

Figure 5.1. Schematic of a Vickers indent in the matrix only layers of a laminate composite.

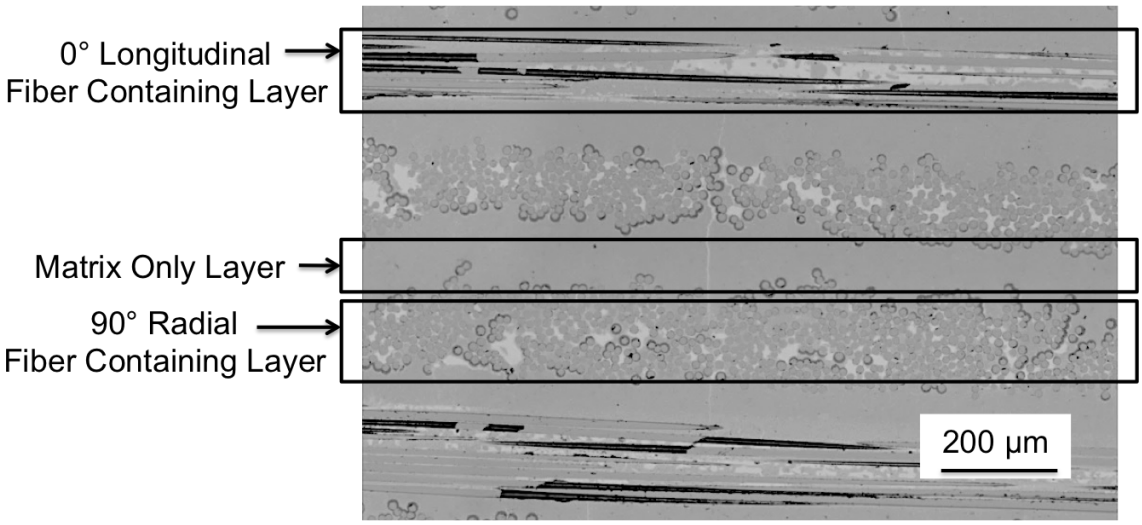

Figure 5.2. Here we show the inner four layers of the 8 layer composite. At the center, we see a thick matrix only region defining the line of symmetry for the composite. On either side of the center matrix region, we see that the fiber layer is oriented in the same direction. For the composite shown, the fiber layers on either side of the center matrix region are oriented in the 90° direction. The next fiber layer shows fibers in the longitudinal direction. These are fibers oriented in the 0° direction.

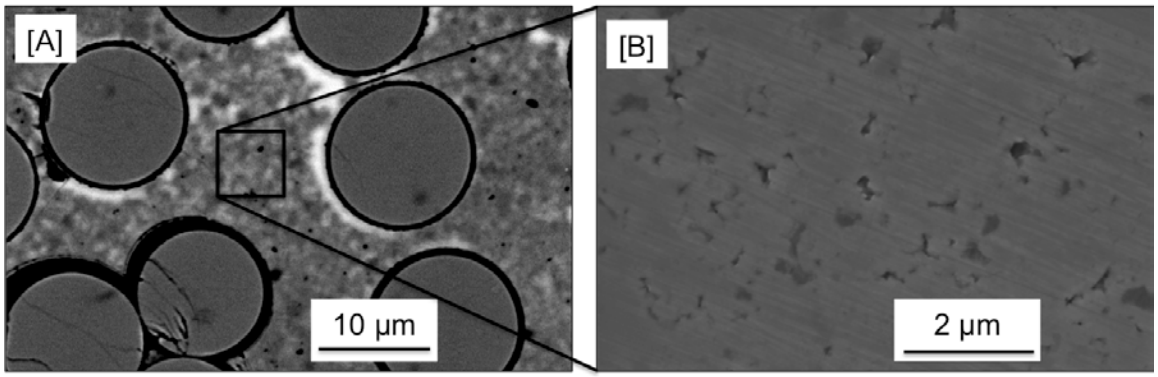

Figure 5.3. [A] is a magnified image of the 90° fibers containing region in Figure 5.2. [B] shows the siliconized-SiC matrix which runs between the fibers and makes up the entirety of the matrix only layers. Note that the silicon in image [B] has been etched out to allow for a better image.

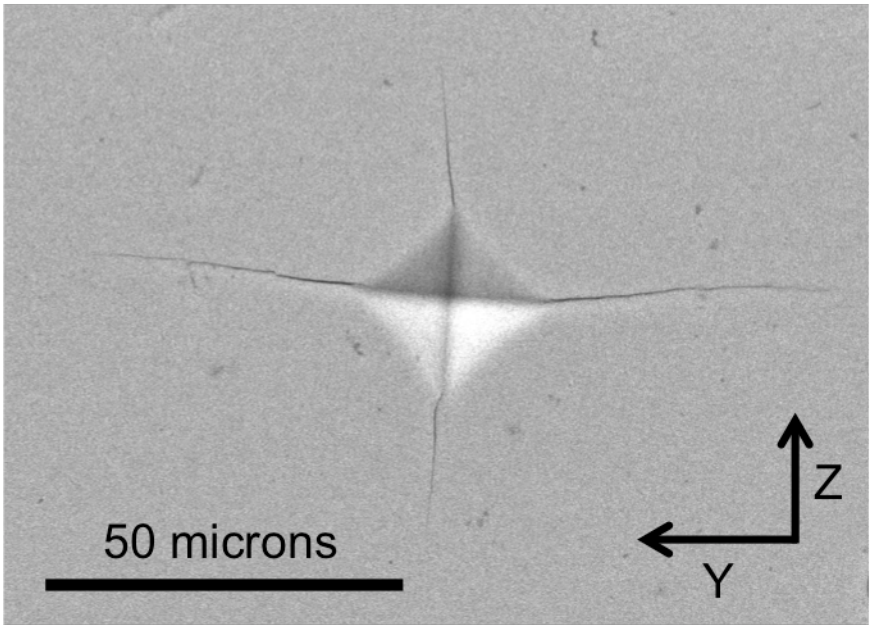

Figure 5.4. Representative indent taken from the matrix only layer of the composite.

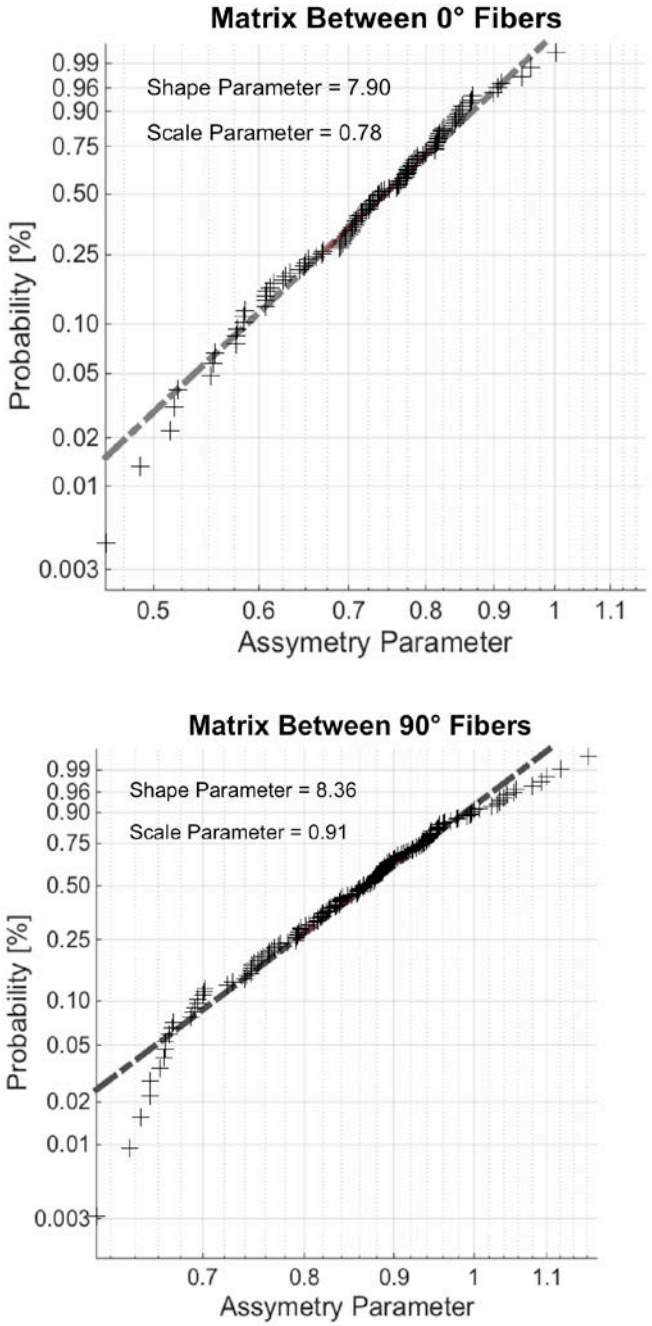

Figure 5.5. Weibull plot of the Asymmetric Parameter (AP) for the 120 indents (6 sample) on the matrix region between two 0° fiber layers is at the top, and below that is the Weibull plot for the 160 indents (8 samples) on the matrix between two 90° layers.

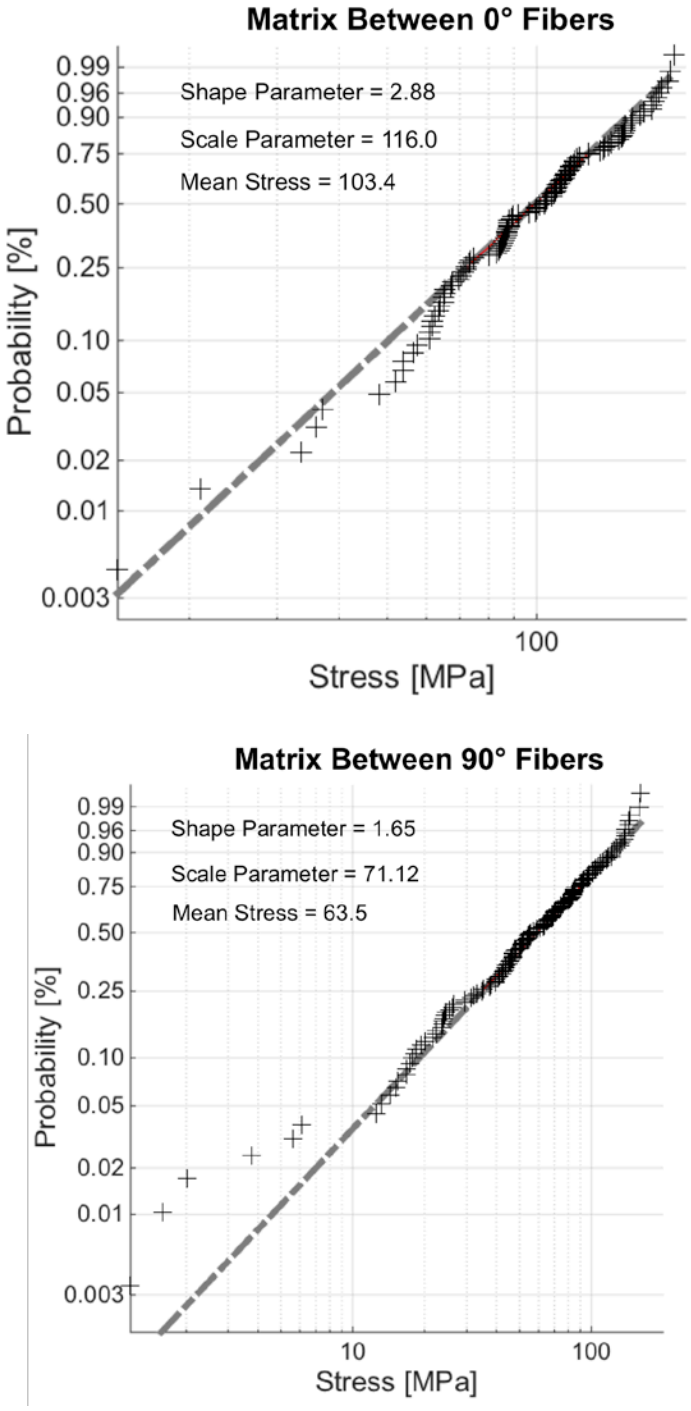

Figure 5.6. Weibull distribution for the probability of the compressive stress measured in the matrix only regions of the composite with a Weibull modulus of 1.17 and a mean value of 76.4 MPa.

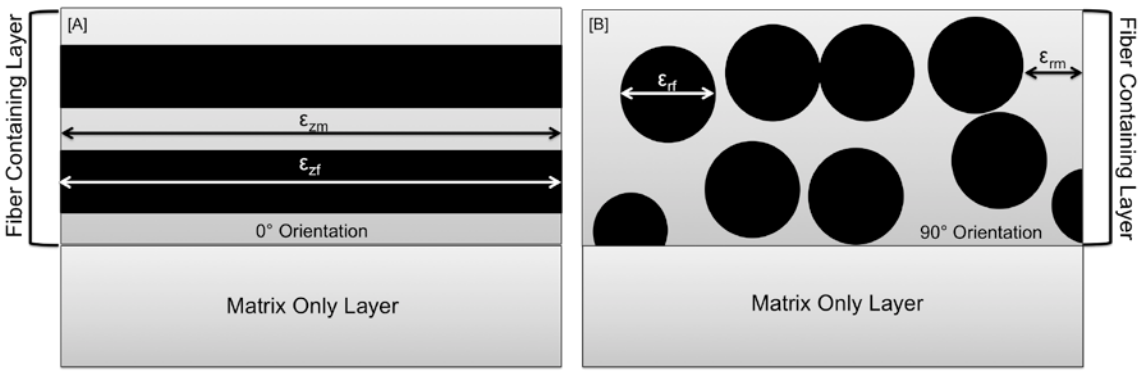

Figure 5.7. Schematic of laminate layups to determine the magnitude of stress at the ply-level as a result of the crystallization expansion of silicon.

Table 5.I. Values for equations in Chapter 5.

Symbol	Meaning	Value
K_{Si}	Bulk Modulus for Silicon	69 GPa
K_{SiC}	Bulk Modulus for SiC	227 GPa
E_{Si}	Young's Modulus for Silicon	156 GPa
$E_{SiC\text{-}m}$	Young's Modulus for SiC in the matrix	380 GPa
$E_{SiC\text{-}f}$	Young's Modulus for SiC in the fiber	420 GPa
E_f^0	Young's Modulus for 0° fiber layer	382 GPa
E_f^{90}	Young's Modulus for 90° fiber layer (Reuss)	377 GPa
E_f^{90}	Young's Modulus for 90° fiber layer (Fibers as holes)	151 GPa
E_m	Young's Modulus for the matrix	335 GPa
V_{Si}	Volume fraction of free silicon in the composite	20 ± 5 vol%
V_m	Volume fraction of matrix in the fiber layer	45 vol%
V_f	Volume fraction of fiber in the fiber layer	55 vol%

Table 5.II. Comparison of model results and experimental measurements of the residual stress at the ply-level

Fiber Orientation	Model [MPa]	Experimental [MPa]
0°	250	103.4
90° (Reuss)	249	63.5
90° (Fiber as holes)	146	

Chapter 6 Subsurface Oxidation of Boron Nitride Coatings on Silicon Carbide Fibers in Melt-Infiltrated SiC/SiC Ceramic Matrix Composites

6.1 Introduction

Fiber interface coatings in ceramic matrix composites (CMCs) provide a vital role in toughening the CMC[1]. The coatings act as a debond layer when a crack approaches[2]. This allows the fiber to remain intact, securing the structural integrity of the composite. Boron Nitride (BN) and carbon coatings on ceramic fibers are typically used as de-bonding interfaces in fiber reinforced ceramic matrix composites (CMCs) [3,4]. Carbon interfaces oxidize more readily[2], while BN coatings oxidize more slowly and at higher temperatures, they are more durable in large temperature range than carbon coatings[5]. Morscher and Cawley have examined the effects of BN oxidizing to B_2O_3 at intermediate temperatures (600-1000°C)[6]. They have found that the glassy boria bonds the matrix to the fiber. With the matrix and fiber bonded, cracks are able to pass from the matrix to the fiber, lowering the toughness of the composite.

Most oxidation studies of CMCs with BN coatings consider the case of a composite under stress and the matrix is microcracked[7,8]. The oxygen penetrates through the microcracks in the matrix[1,6,9] to react with the BN interface. However, oxidation of the BN coating can occur at location where BN-coated fibers intersect the external surface. Luthra refers to this phenomenon as “ends-on-oxidation” and analyzed its role for penetration of oxygen into the composite[1]. Here we examine ends-on-oxidation for a CMC consisting of a melt-infiltrated, reaction bonded SiC matrix and SiC fiber with a BN coating. The goal is to examine how readily oxygen penetrates

BN coatings in a moderate water vapor environment, without an externally applied load. We will see how the coating thickness and temperature affects the oxygen penetration beneath the surface of the composite.

6.2 Methods

6.2.1 Sample Preparations

The material system being examined is HiPerComp™, supplied by GE Aviation, a SiC-SiC CMC with a BN coating on the fibers (Figure 6.1). The silicon carbide fibers had a proprietary boron nitride-based coating, as reported by Luthra and Corman[10]. Specimens were machined from plates with a [0/90]2s architecture with ~33vol% SiC fiber loading. The matrix was reaction bonded SiC containing ~20vol% unreacted free silicon, produced by melt infiltration. This particular CMC has no environmental barrier coating (EBC) to protect it from oxidation. The BN coating on the fibers is applied while the fibers are in bundles known as tows. Note, not all fibers are coated uniformly. The variation can be seen in Figure 6.1, where a polished section where the BN-rich coating between the SiC fiber and SiC:Si matrix appears as a dark ring. It is worth noting that thicker coatings typically appear on the outside of the tow.

Six samples were made from the material described above. Samples machined by diamond sawing were polished to a 1 micron diamond finish in DP-708, a non-aqueous lapping oil from Mager Scientific. Samples were annealed in an MHI box furnace with Zicar molybdenum disilicide elements. The oxidation atmosphere was ambient laboratory air, which had an absolute humidity in the range of 10±2 g/m^3, based on the laboratory temperature and relative humidity at the time of the experiments. This corresponds to a water vapor pressure around 15 hPa, for a partial pressure of H_2O in the oxidation furnace around 0.015. Two different

temperatures were examined, 1200°C and 1285°C. At both temperatures, a sample was annealed at 20, 40, and 80 hours.

The extent of oxidation along the surface was determined using microstructure analysis. The external oxide scale on the SiC matrix was examined in cross-section, but was too small to measure reliably from micrographs. Instead the thickness was characterized using nuclear reaction analysis (NRA). The sample was placed in a Deuterium ion beam with an accelerating voltage of 877 keV. The detection angle is set to 150°.

Oxygen penetration along fiber tows normal to the oxidation surface was characterized by examining the end-on tows (90° fiber tows in the 0/90 laminate). After annealing the samples, each one was mounted in epoxy at an angle using a glass slide to prop up one side (Figure 6.2).

During the cure process of the epoxy, the samples were prone to shifting. In order to determine the exact depth being examined, the samples were removed from the epoxy after polishing. The heights of each side (m and h in Figure 6.2) were measured. The angle of polish was determined by:

$$\theta = \tan^{-1}\frac{h-m}{y} \qquad [1]$$

where theta is the angle of interest, h and m are the height of the two legs, and y is the total length of the sample. All of the specifications can be seen in Figure 6.2.

This angle polish allows examination of many oxidation depths in a single sample. Any lateral position in the plane of polish (y in Figure 6.2) can be related to the depth removed by polishing from the surface (z in Figure 6.2) by $z = y\tan\theta$. By examining the microstructure at various locations y, we observe BN coatings at a depth z beneath the exposed surface. At each lateral location, we observed the appearance of the BN layers normal to the oxidation, at depths ranging from 0 microns to 1000 microns below the oxidation surface.

To traverse a single sample it takes approximately 80 fields of view along a single fiber layer. For each sample, two fiber layers were analyzed completely. This results in approximately 7000 fiber coatings analyzed for each sample.

6.2.2 Identifying Oxidized BN Coatings

In order to measure the thickness of the coatings, secondary electron images using the Philips XL30 SEM (SEMTech Solutions, North Billerca, MA) were used to provide the most precise measurement. Energy dispersive spectrometry (EDS) maps were used to indicate the presence of oxygen in the annulus between the fiber and the matrix. Since oxidation of BN coatings causes the release of N_2 gas and forms B_2O_3 glass, for a coating to be categorized as oxidized it had to meet two criteria: 1) oxygen was present in the EDS map, and 2) nitrogen signal in that coating was greatly diminished. These two criteria were determined using the EDS images. If significant oxygen is detected, we presumed that sufficient oxygen had penetrated so the BN coating was oxidized. EDS maps were collected with the Philips XL30 using an accelerating voltage of 10keV and a map resolution of 128x100 pixels. Each map was the result of 128 frames averaged together. Each map scan took approximately 10 minutes to complete.

To establish the reliability of the EDS, selected sampler were also analyzed by wavelength dispersive spectroscopy (WDS) using a Cameca SX-100 Electron Microprobe Analyzer (Gennevillers, France). WDS analysis was done using an accelerating voltage of 15 keV and a dwell time of 0.03 sec, a step size of 0.2 pixels, and a resolution of 256x192. The crystals selected were PC2 for nitrogen, LPCO for oxygen, and LTAP for silicon. Each scan took approximately 80 minutes to complete.

6.3 Results

6.3.1 External Oxide Scale on SiC:Si Matrix

With these oxidation conditions, silica-rich external oxide was difficult to observe by in the polished cross section. Instead, the matrix oxide thickness on the on the external surface was characterized by nuclear reaction analysis (NRA). NRA reactions are characteristic of the atoms of which the beam is in contact. As the majority of the signal from the oxide formed on the RBSiC matrix, we can presume this represents the extent of the external oxide scale thickness. Therefore, we used the existence of the oxygen reaction to determine the depth of the oxide layer. The oxide scale after 20 hours at 1200°C was about 0.75 ± 0.10 microns. After 80 hours at 1285°C the average scale was about 3 ± 0.10 microns.

6.3.2 Oxygen in BN Coatings

The end-on 90^{o} tows were exhaustively examined for two tows per sample. Secondary electron images and corresponding EDS oxygen maps were obtained for hundreds of fields of view, each about 300 microns wide. The images were taken starting from the shallow side of each specimen, which was about 40 microns below the external surface, to the deep side of the specimen, which was about 900 microns below the external surface. Images from about 80 fields of view were required to cross from one side of the sample to the other, for each tow examined. The depth varied about 15 microns from the right side to the left side for each field of view. The coatings on more than 40,000 individual fibers were characterized to determine if they had been oxidized, and to determine the coating thickness.

Examples of SE, nitrogen EDS, and oxygen EDS images are shown in Figure 6.3. These images are taken from an area approximately 100 microns deep from the exposed surface of a

sample that has been annealed at 1200°C for 40 hours. The field of view is from a single tow and contains ~150 fibers.

In part [A] of Figure 6.3, we see bright areas along some of the coatings. This is indicative of charging on a non-conductive surface. In part [B], we show the nitrogen EDS map for the same region imaged in part [A]. The EDS map has been inverted, meaning that the dark areas indicate nitrogen signal and the light areas lack nitrogen. This was done to show the contrast more clearly. In part [B] of Figure 6.3, we see that the same BN coatings that were bright in part a have very little nitrogen signal, indicated by the circles in part [B]. In part [C] of Figure 6.3, we show the oxygen EDS map for the same region. Again, we have inverted the map, meaning the dark areas indicate high oxygen and light areas are low oxygen. We see that the bright, charging coatings in part a show high oxygen signal.

Certain coatings appear to have been oxidized 100 microns below the surface, but not many coatings are oxidized. About 25% of the fibers in this field of view have coatings with a strong oxygen signal. Many of the apparently oxidized coatings are on fibers on the outside of the tow. It is also worth noting that some individual fibers are not uniformly oxidized.

To be certain that the oxygen signal was not an artifact, we used wavelength dispersive spectroscopy (WDS) on as-received samples and on the annealed samples for verification. WDS was not used for full analysis since an elemental map by WDS required ~80 minutes, while it was possible to capture an element map with EDS in ~10 minutes. In Figure 6.4 we can see that the as-received sample has nearly no oxygen when compared to the annealed sample. This shows us that the oxygen indicated in the EDS maps was in fact from the heat-treatments, and not present prior to annealing.

6.3.3 Depth Characterization of BN Coatings

High-resolution images were stitched together to provide the composite image in Figure 18. The bottom of Figure 18 shows the SE image, and above that is the corresponding oxygen EDS image of that area. Below the images is a scale that provides the depth below the oxidation surface that corresponds to the lateral location pictured. This shows eight of the eighty fields of view that span the specimen, comparing four shallow fields in the 50-80 micron depth (right side of Figure 6.5) with deep fields of view (left side of Figure 6.5) in the depth range of 600-640 microns beneath the external surface. The fields of view in dashed boxes appear in detail in Figure 19A and Figure 19B.

In part B of Figure 6.6, we have shown the SE and oxygen EDS for a fiber tow bundle that was near the oxidation surface. The near surface fiber coatings show oxidation which is 20x deeper than the surface layer of oxide as determined by NRA. In part A of Figure 6.6, we have shown the SE and oxygen EDS images for a region that was much deeper from the oxidation surface. Even at 600 μm deep from the oxidation surface, we see that there is still significant oxidation of the BN fiber coatings. This is more than 200x deeper than the native oxide layer. From these images it is apparent that the oxygen tends towards the thicker coatings, which appear more frequently on the outside of the fiber tow bundles.

6.3.4 Statistics on the BN Coatings

The microstructure displayed in the various figures shown indicates how complex the organization of the fiber bundles can be. The BN formed from the CVD process does not uniformly coat the fibers in the tow bundle. As a result, the coatings on the ouside of the fiber tows are typically thicker than the coatings on the interior.

Using the secondary electron (SE) images, all of the BN coatings for each sample were measured. Due to the variation of the coating sizes, we divided the coatings into several thickness ranges for simplification purposes. The ranges are such that every coating less than one micron is grouped as “submicron.” Coatings greater than one micron and less than two microns are grouped as “1 micron.” Coatings that are greater than two microns and less than three microns are grouped as “2 micron,” and coatings greater than three microns are all grouped together as “>3 micron.”

Each sample had approximately 7000 fiber coatings counted. The number of coatings of each size for each sample is listed in Table 6.I. About 63% of the coatings are less than 1 micron thick (submicron range), 16% are in the 1 micron thickness range, 16% are in the 2 micron thickness range, and 5% fall in the three micron thick or thicker range. These thicker coatings were located mostly on the outer part of the fiber tows. Although the submicron thickness range is the largest category of fiber coatings, we see that coatings of this size do not indicate oxygen based on the EDS maps.

For the 1 micron and 2 micron groups, we see similar amounts of each coatings thickness. However, we notice that the 2 micron group shows a much higher percentage of oxidized fiber coatings in each sample. Coating sizes greater than 3 micron make up only a small portion of the total number of coatings. For these large coating sizes, we see that nearly all of them are oxidized. The overall trend given by the table is that increasing the thickness of the coating increases the likelihood that the coating will be oxidized.

6.3.5 Dependence of Oxidation of BN Coatings as a Function of Coating Thickness

With the angle polish that was shown in Figure 15, we were able to quantify the depth of oxygen penetration for each of the coatings. In Figure 6.7, we examine the percentage of

oxidized fibers over the range of depths for a sample annealed at 1285°C for 40 hours. The graph shown in Figure 20 is characteristic of all times and temperatures of oxidation. Only one graph is shown to limit redundancy.

In this figure, we see that increasing the thickness of the coating increases the likelihood of that coating being oxidized at any given depth. As the depth into the sample increases, the percentage of oxidized coating decreases for all coating sizes. It is also worth noting that for all times and temperatures, the submicron coatings do not appear to oxidize.

Because these graphs tend to get cluttered, we have chosen to simplify the data by showing the depth at which each coating thickness range has 20, 50, and 80% of the fiber coatings oxidized (Figure 6.8). For the depth analyzed, the “>3 micron” range never achieved less than 20% oxidized fiber coatings. Therefore, this point was left off of the graph in Figure 6.8.

This graph shows very clearly that as the coating thickness increases, the likelihood of the coating being oxidized increases. We also see that oxygen has penetrated more than 800 microns deep into the composite without matrix cracking.

6.3.6 Dependence of Oxidation Depth as a Function of Annealing Temperature

In Figure 6.9a, we show the percentage of coatings grouped as 2 micron that are oxidized at each depth. In the graph, the filled in points indicate samples that have been heat treated at 1285°C, and the open points are indicative of samples heat treated at 1200°C. Figure 22b shows the same information, but only indicates the depths at which 20, 50, and 80% of the 2 micron fiber coatings are oxidized.

We see that the high temperature anneal provides for deeper oxygen penetration into the composite. We also see that at the higher temperature, the amount of time of the oxidation has a significant affect on the likelihood a coating will be oxidized deeper.

6.4 Discussion

The data provided gives information on a number of variables as they pertain to the penetration depth of oxygen within the fully dense composite material. Strong oxygen signals were detected nearly 1000 microns deep into the composite, which we claim is only a result of oxygen ingress along the end-on fiber coatings. It is worth noting again that these samples are not exposed to stress and were examined as-received, with no imposed microcrack damage.

The depth of oxygen penetration is dependent on the time and temperature of the annealing. This is shown very well in part b of Figure 6.9. The filled in markers show the higher temperature annealing, which all indicate a deeper oxygen penetration on the fiber coatings than the lower temperature annealing counterparts. And although more obvious in the 1285°C annealing, we see that there is an increase in the oxygen penetration as a function of time at temperature during the anneal.

We examined planes-of-polish at a constant distance from the oxidation surface. This is convenient as all fibers are approximately round, coating thickness can be easily discerned, and it becomes easy to see which have been oxidized. We cannot discern from a single plane-of-polish if fibers were exactly straight, or it they moved enough to intersect another fiber coating above it. We did examine the statistics of fibers which were far enough to be considered isolated, and compared that with fibers which seemed to be touching. For each thickness interval, we observed no difference in fraction oxidized between isolated fibers and touching fibers.

6.4.1 Deep Penetration of Oxygen Without an Applied Load

In 80 hours at 1285°C, we see oxygen signal coming from 900 microns deep within the composite. It is also shown in the EDS mappings that the coating annulus is filled with oxidized material. This implies that the BN oxidizes to liquid boria for some amount of time, and that water vapor is low enough that the oxide does not immediately evaporate as seen by Jacobson[11] and modeled by Xu[7] and Parthasarathy[8].

The rate of oxidation of silicon carbide is dramatically enhanced by contact with boria to form a borosilicate, due to the much larger diffusivities of oxygen and water in the borosilicate[12,13]. This allows for deep oxygen penetration into the fully dense composite in a relatively short amount of time.

Oxidation of the BN coatings results in a liquid boria phase in the annulus surrounding the fiber. Klaus Nickel notes that, in presence of reactive borosilicate, the diffusion constants must change with time and temperature, making conventional oxidation models less useful[14]. The liquid boria is constantly reacting with the surrounding SiC[15], forming a more silicious borosilicate. As the boria becomes more diluted with silicate glass, the diffusion constant is constantly changing, making diffusion kinetics difficult to determine.

6.4.2 Thickness Effect

We observe that thicker BN coatings are more likely to oxidize deep into the composite than thin coatings. However, we also see that the oxidation penetration is not uniform in coatings of the same thickness. We presume that all coatings are deposited equivalently. We observe that at any given depth, some of the coatings of a certain thickness are oxidized, and some of them are not. For instance, if we look at Figure 6.8, we can see that in 40 hours at 1285°C, 50% of the

2 micron thick coatings are oxidized 550 microns deep. This also means that 50% of the 2 micron coatings at 550 microns deep are not oxidized.

In a study by Morscher et al., they witness the deep oxygen penetration in BN coatings at much lower temperatures (700 and 800C)[16]. Morscher determined that processing of the BN coatings, specifically temperature and using silicon as a dopant had a large effect on the penetration depth of oxidation. He showed that higher deposition temperatures of the BN coating and higher silicon contents in the BN coatings greatly reduced the depth at which oxygen was able to penetrate the mini-composite. He also found that thicker coatings allow for deeper penetration of oxygen under the same conditions.

In our experiment, the entire sample is exposed to the environment equally. Therefore, the water content is constant for all of the BN coatings, and it is not a water vapor concentration difference causing the different penetration depths in coatings of the same thickness.

We have binned the coatings into similar thicknesses, providing some variation within each bin. We later examined coatings with the exact same thickness. We found that even coatings of the same thickness showed variation in the likelihood of being oxidized at the depths examined. Thus, the variation in depth is not a result of binning the data sets.

For the BN coatings in this experiment, it is unknown what temperature the coatings were deposited onto the fibers. It is also unknown at this time if any silicon dopant was used, and if it was, how much. We do, however, know that all of the coatings were manufactured in the same way. We examine different oxidation rates on coatings of the same thickness exposed to the same environment. Based on the Moscher study, this would suggest that under the same processing conditions, the coatings are not chemically equivalent and oxidize at different rates.

6.5 Conclusion

We have discovered very deep oxygen in a fully dense ceramic matrix composite that has no external load applied to it. The boron nitride coatings act as oxygen channels into the composite. Oxygen was measured using energy dispersive spectroscopy more than 300x deeper into the composite than the native oxide layer formed on the surface of the composite. This is consistent with boria formation increasing the diffusion rate of oxygen.

It was determined that isolated fiber coatings were just as likely to oxidize as fiber coatings, which were close enough to touch. We find that thicker coatings allow oxygen to ingress deeper than thin coatings. BN oxidized to liquid boria to form a borosilicate glass in the annulus surrounding the fiber. The borosilicate continues to degrade the surrounding SiC, increasing the silicate concentration, and greatly increasing the complexity of determining the diffusion rate of water into the fiber coating.

We found that at any given depth, some of the fiber coatings of a specific thickness showed an oxygen signal from the EDS, but others in the same exact thickness indicated no oxygen signal. This experiment exposed all fiber coatings to the environment equally. We suggest that coatings deposited under the same conditions are not chemically equivalent.

Acknowledgements

The authors would like to thank Fabian Naab at the University of Michigan's Molecular Ion Beam Lab (MIBL) for his assistance with Nuclear Reaction Analysis. We thank Dr. Katherine Sevener for valuable comments. This research was funded by GE Aviation under a University Strategic Alliance grant.

References

1. Luthra KL. Oxidation-Resistant Fiber COatings for Non-Oxide Ceramic Composites. *J Am Ceram Soc*. 1997;80:3253-3257.

2. Sheldon BW, Sun EY, Nutt SR, Brennan JJ. Oxidation of BN-Coated SiC Fibers in Ceramic Matrix Composites. *J Am Ceram Soc*. 1996;79:539-543.

3. Cranmer DC. Fiber Coating and Characterization. *Am Ceram Soc Bull*. 1989;(68):415-419.

4. Baskaran S, Halloran JW. Fibrous Monolithic Ceramics: III, Mechanical Properties and Oxidation Behavior of the Silicon Carbide/Boron Nitride System. *J Am Ceram Soc*. 1994;5(77):1249-1255.

5. Jacobson NS, Fox DS, Opila EJ. High Temperature Oxidation of Ceramic Matrix Composites. *Pure Appl Chem*. 1998;70:493-500.

6. Morscher GN, Cawley JD. Intermediate Temperature Strength Degradation in SiC/SiC Composites. *J Eur Ceram Soc*. 2002;22:2777-2787.

7. Xu W, Zok F, McMeeking R. Model of Oxidation-Induced Fiber Fracure in SiC/SiC Composites. *J Am Ceram Soc*. 2014;11(97):3676-3683.

8. Parthasarathy TA, Przybyla CP, Hal RS, Cinibulk MK. Modeling Environmental Degradation of SiC-Fiber Reinforced CMCs. 2015.

9. Heredia FE, McNulty JC, Zok FW, Evans AG. Oxidation Embrittlement Probe for Ceramic-Matix Composites. *J Am Ceram Soc*. 1995;6(78):2097-2100.

10. Corman GS, Luthra KL. Silicon Melt Infiltrated Ceramic Composites (HiPerComp). In: *Handbook of Ceramic Composties*. New York: Springer; 2005.

11. Jacobson NS, Morscher GN, Bryant DR, Tressler RE. High-temperature oxidation of boron nitride: II, boron nitride layers in composites. http://apps.webofknowledge.com.proxy.lib.umich.edu/full_record.do?product=UA&search_mode=GeneralSearch&qid=7&SID=2DK2HEXGrTQVSdt3ojS&page=1&doc=2.

12. Quemard L, Rebillat F, Guette A, Tawil H, Louchet-Pouillerie C. Degradation mechanisms of a SiC fiber reinforced self-sealing matrix composite in simulated combustor environments. doi:10.1016/j.jeurceramsoc.2006.02.042.

13. Reillat F, Garitte E, Guette A. Quantification of Higher SiC Fiber Oxidation Rates in the Presence of B2O3 Under Air. *Am Ceram Soc Proc*. 2010:135-149.

14. Nickel KG. Ceramic matrix composite corrosion models. doi:10.1016/j.jeurceramsoc.2004.12.010.

15. Ogbuji LUJT. Pest-resistance in SiC/BN/SiC composites. doi:10.1016/S0955-2219(02)00268-6.

16. Morscher GN, Bryant DR, Tressler RE. Environmental Durability of BN-Based Interphases (For SiC/SiC Composites) in H2O Containing Atmospheres at Intermediate Temperatures. *Ceram Eng Sci Proc*. 1997;18.

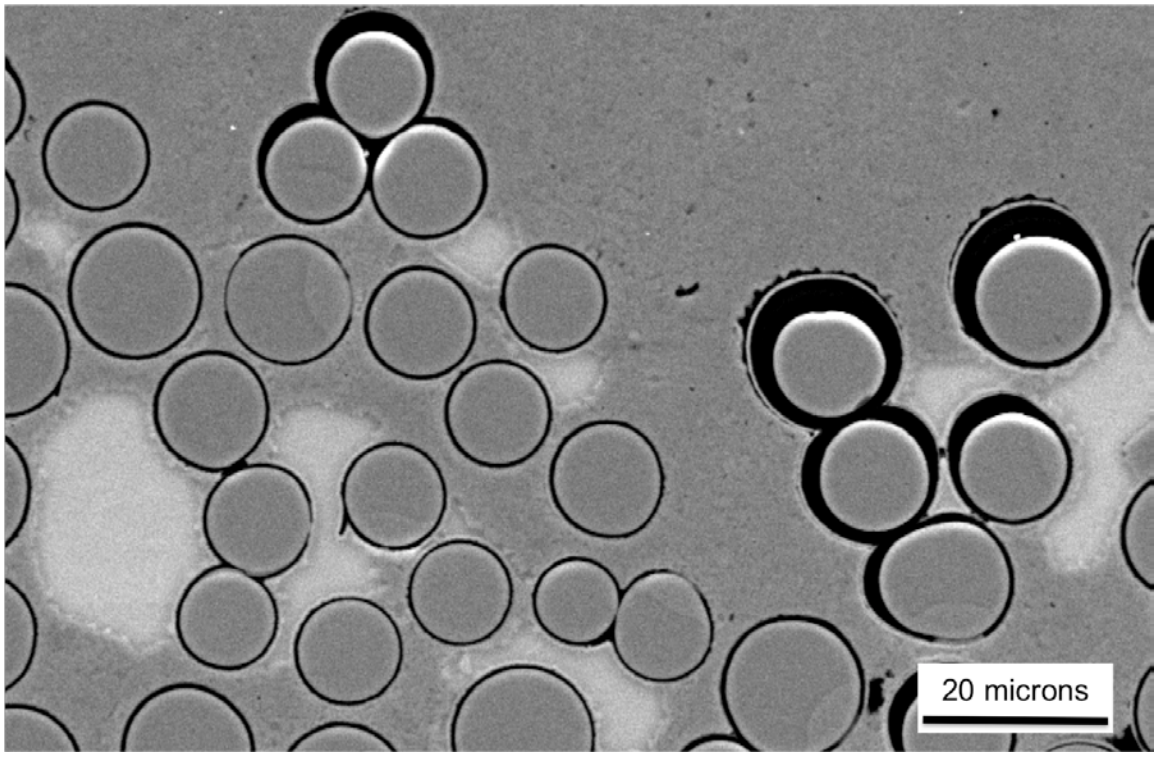

Figure 6.1. Image from a fiber tow bundle in HiPerComp™. The black circles surrounding the SiC fibers are the BN coatings. Notice the large variation in thickness among the coatings. The light grey is unreacted free silicon due to processing.

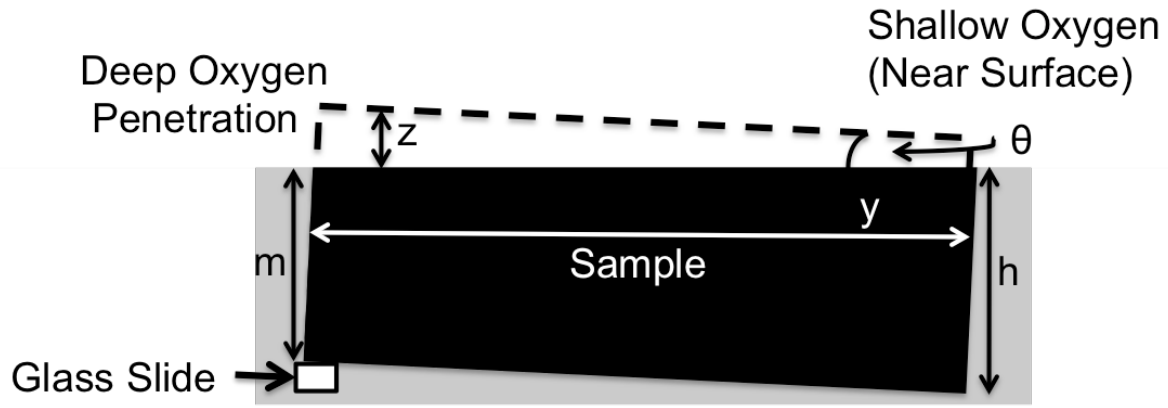

Figure 6.2. Samples are mounted on an angle with the assistance of a glass slide. The samples are then ground to reveal coatings near the surface (right) and coatings deep compared to the oxidized surface (left).

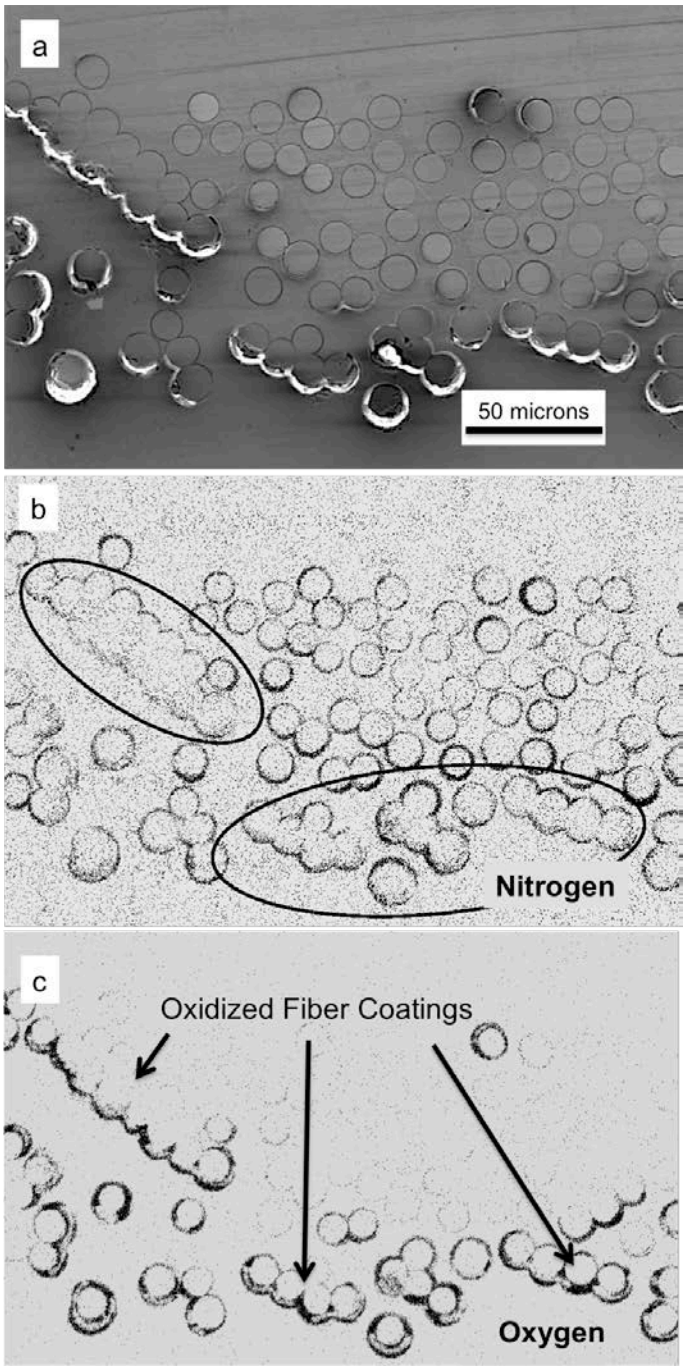

Figure 6.3. All images are of the same fiber tow bundle that has been heat treated at 1200 °C for 40 hours in ambient air. [A] shows the SE image of the tow bundle, [B] is the nitrogen EDS map of the bundle, and [C] is the oxygen EDS map of the same area. Oxidized coatings are indicated in b by ellipsis, and in [C] with arrows.

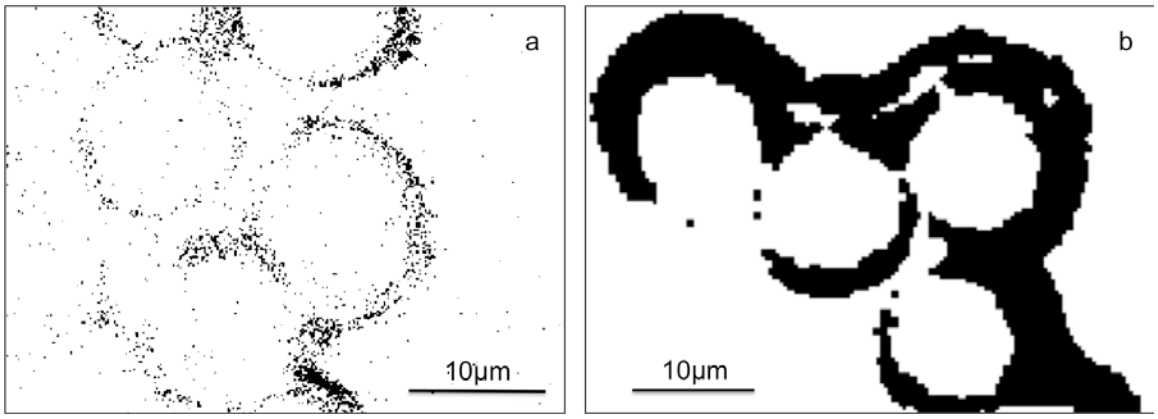

Figure 6.4. WDS results from an as-received sample [A], and a sample that has been annealed at 1200°C for 40 hours [B].

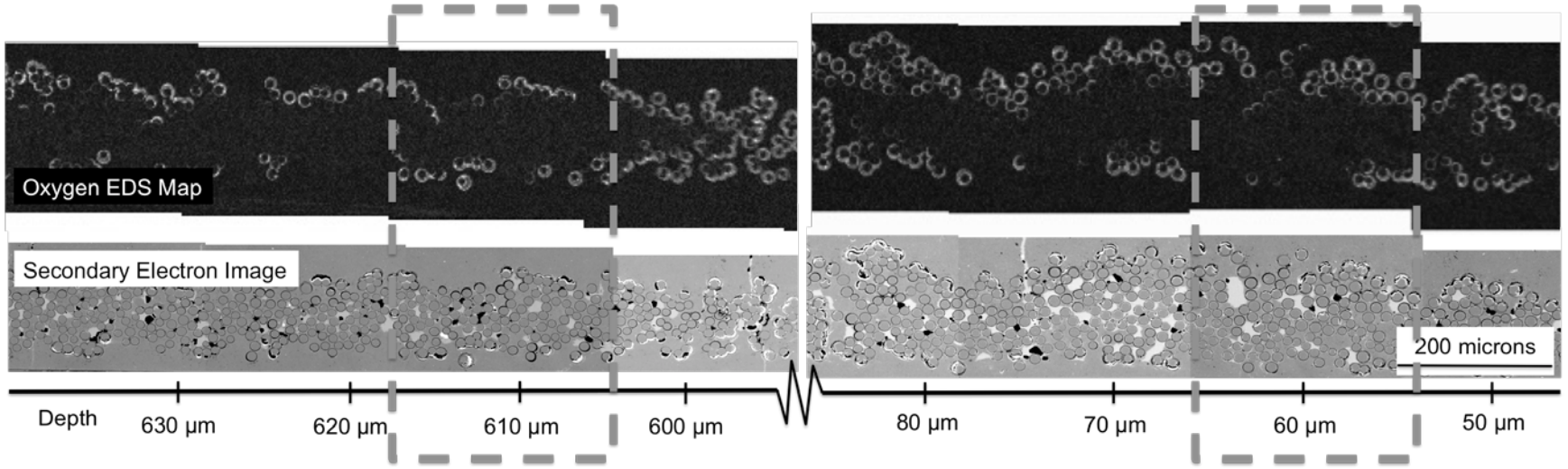

Figure 6.5. Image of a tow in HiPerComp™ after being annealed. The image shows the oxygen EDS images stitched together. Below the images, we have provided the depth below the oxidation surface. This depth is corresponds to the z depth indicated in Figure 15.

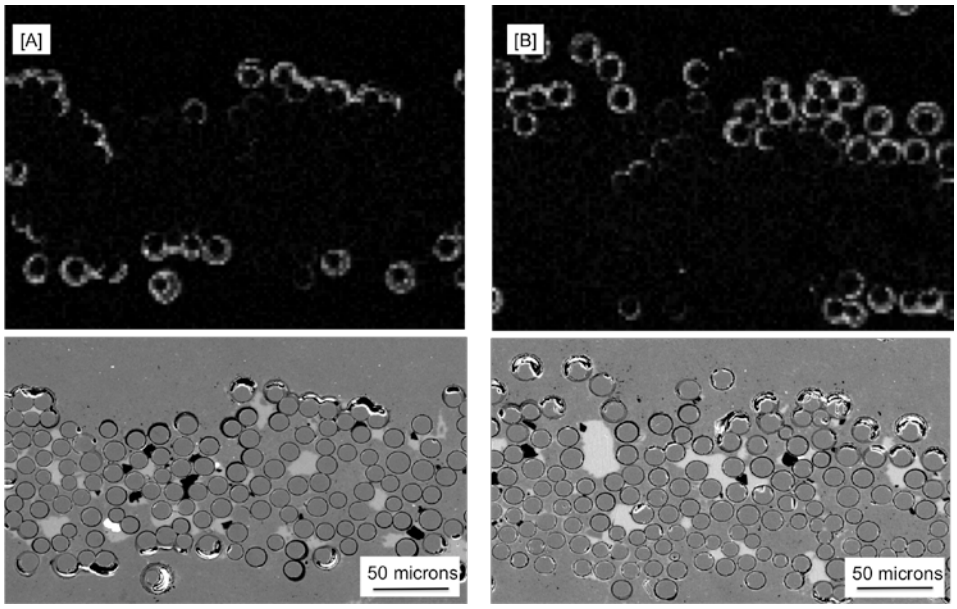

Figure 6.6. SE and oxygen EDS images at two different depths away from the external surface. [A] is taken approximately 600 microns deep from the exposed surface, and [B] is approximately 60 microns deep.

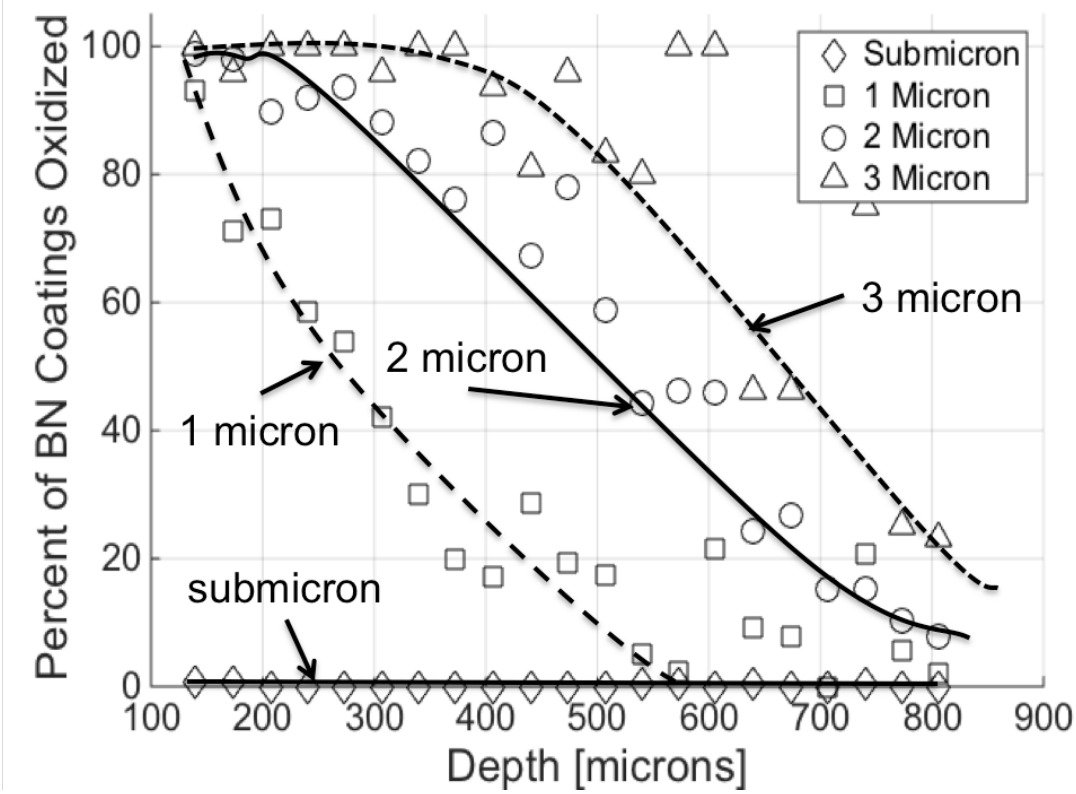

Figure 6.7. Shows the percent of oxidized coatings in each thickness range for the sample oxidized at 1285 °C for 40 hours. Both graphs show that thicker BN coatings are more likely to be oxidized at any given depth (lines drawn to guide the eye).

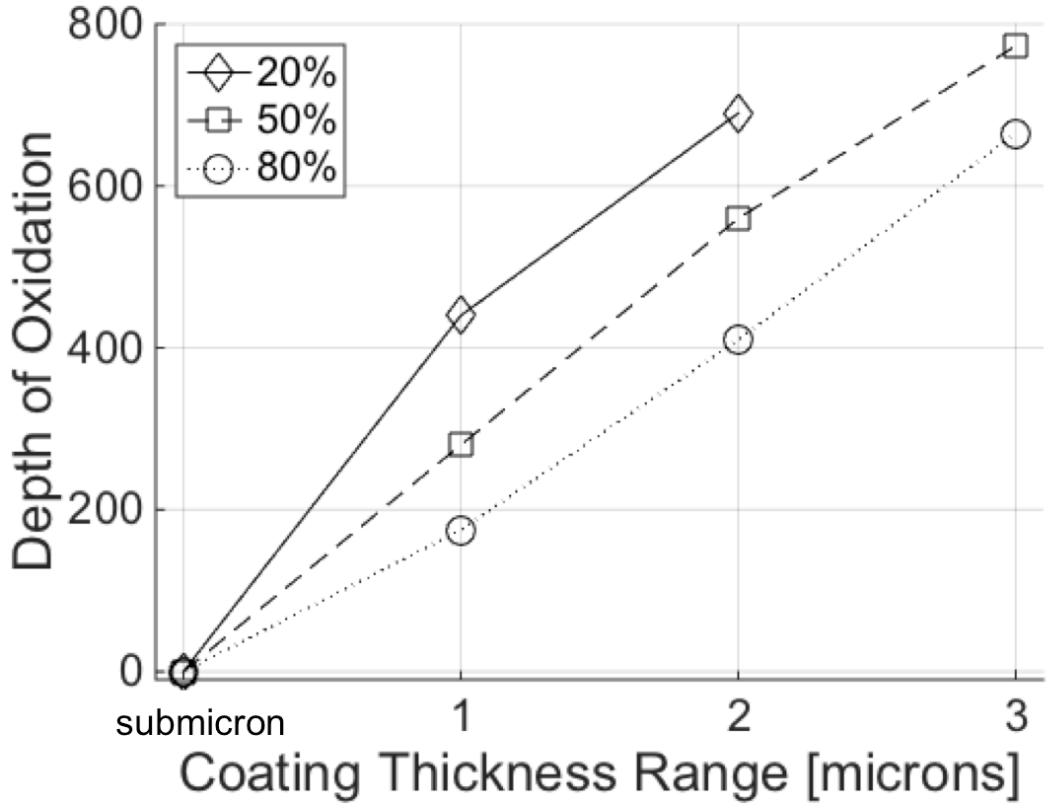

Figure 6.8. Graph indicating the depth at which each coating thickness range shows 20, 50, and 80% of the coatings as oxidized after a 40 hour anneal at 1285°C.

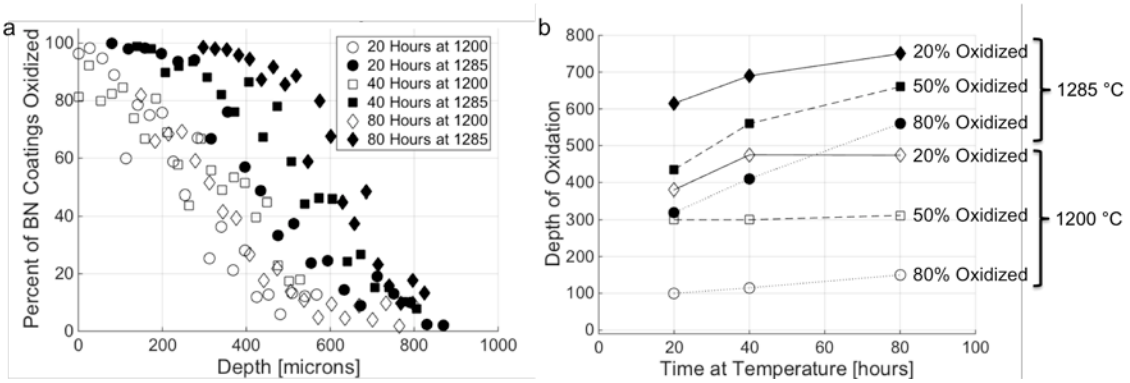

Figure 6.9. Graphed at the percent of oxidized coatings vs. depth for each time period and temperature for all 2 micron range coatings. In [A], the open points indicate samples heat treated at 1200°C and the closed points are samples heat treated at 1285°C. [B] shows the same information simplified to the depths where 20, 50, and 80% of the 2 micron coatings are oxidized.

Table 6.I. Results from oxidized BN coatings

Annealing Conditions		Submicron			1 micron			2 micron			>3 Micron		
Anneal Temp	Anneal Time	Total Number	Percentage of Total	Percent Oxidized	Total Number	Percentage of Total	Percent Oxidized	Total Number	Percentage of Total	Percent Oxidized	Total Number	Percentage of Total	Percent Oxidized
1200	20	5021	64.1%	0.2%	1491	19.0%	17.0%	1140	14.6%	47.7%	169	2.2%	71.0%
	40	4860	63.2%	0.1%	1642	21.4%	18.0%	1019	13.3%	58.3%	175	2.3%	74.3%
	80	4690	59.7%	0.0%	1452	18.5%	6.0%	1501	19.1%	30.0%	211	2.7%	67.8%
1285	20	4797	62.2%	1.0%	1036	13.4%	29.3%	1323	17.2%	49.5%	558	7.2%	77.4%
	40	4820	63.0%	0.1%	846	11.1%	28.0%	1345	17.6%	62.0%	645	8.4%	91.8%
	80	4804	65.5%	0.2%	923	12.6%	23.6%	1267	17.3%	67.1%	340	4.6%	92.6%

Chapter 7 Conclusion

This study has identified a previously unknown source of high magnitudes residual microstress in reaction bonded silicon carbide (RBSiC). We determined that the crystallization expansion of the silicon phase of RBSiC results in large residual microstresses in the silicon and SiC phases of RBSiC. The microstress developed from thermoelstic mismatch of the two phases was shown to be negligible compared to the high microstress values from the crystallization expansion of the silicon phase.

The microstresses were measured using Raman spectroscopy in three different RBSiC materials. Two of the materials were monolithic RBSiC, and the third was a ceramic matrix composite matrix. All three materials measured residual microstresses in the GPa range for the silicon and SiC phases. The two different monolithic RBSiC materials showed very little variation position to position and sample to sample. The composite matrix showed much larger variation, but proved to follow a normal distribution.

In order predict the residual microstress of a RBSiC material, we adapted a thermoelastic model. The modification took the strain developed from a thermal expansion mismatch and replaced it with the strain caused by the crystallization expansion of the silicon phase. This model was shown to be in good agreement with the measured values of the microstress in RBSiC. This model could also be used to determine the overall strain (i.e. displacement) of the two-phase RBSiC, or siliconized-SiC.

Since the two-phase RBSiC is only one component of the composite, we sought to determine how the expansion of that two-phase siliconized-SiC would influence the rest of the

composite. We examined how a layer of matrix only material would expand differently than a layer in the composite consisting of matrix and fibers. We found that stress predicted in the matrix only layer was dependent on the orientation of the surrounding fiber layers. We also found that the stress magnitude and stress ratio were closely related to the measured ply-level stress values when the fibers in the 90° direction were modeled as holes, and did not participate as a structural component of the analysis.

The ply-level stress was measured using the indentation method of Zeng and Rowcliffe. In nearly every indentation of the matrix only layer, there was anisotropy of the crack lengths of the Vickers indent, consistent with a compressive stress in the matrix only layers. The asymmetric parameter (AP), which we identified as the ratio of vertical crack length to horizontal crack length, was found to follow a Weibull distribution. Using the indentation method defined by Zeng and Rowcliffe, we were able to determine the apparent stress of the matrix only layer of the composite. The measured apparent stress was slightly lower than what the adopted model predicted. This is most likely due relaxation that occurred during processing of the composite.

We then examined the relaxation of the residual microstress of the silicon and SiC phases of the siliconized-SiC. It was found that relaxation of the residual microstress follows power law creep. The stress exponent measured for the composite matrix was 10.4. This is in very good agreement with the stress exponent measured in monolithic RBSiC in a previous study by Weiderhorn et al., which was verified in this study.

The oxidation of the boron nitride (BN) coatings has been examined. It was found that oxygen penetrated more than 900 microns deep into the fully dense composite within 80 hours at 1285°C, without any type of mechanical load applied. We determined that the oxygen penetrates

through ends-on oxidation of the BN coatings. This is a new mechanism for oxygen penetration since most of the current research focuses on oxygen ingress through cracks in the matrix. Deep oxygen penetration is consistent with liquid boria providing enhanced oxidation rates SiC

The thickness of the BN coatings was found to greatly influence the depth of oxygen penetration into the fully dense composite. We determined that the depth to which oxygen was allowed to penetrate the composite was related to the thickness of the BN coating. BN coatings that were less than 1 micron thick showed no oxygen ingress at all temperatures and times examined. However, the thicker coatings acted as tunnels, allowing oxygen to penetrate deep into the composite. We examined that not all BN coatings oxidize at the same rate. Since the environment to which all of the coatings were exposed was equivalent, we concluded that the BN coating have some chemical difference despite being deposited under the same conditions.